Molecular simulation studies of adsorption and diffusion : phenomena of gases in porous materials

Liu, B.

Publication date
2008

Document Version
Final published version

Molecular simulation Studies of Adsorption and Diffusion Phenomena of Gases in Porous Materials

Bei Liu

Molecular simulation Studies of Adsorption and Diffusion Phenomena of Gases in Porous Materials

ACADEMISCH PROEFSCHRIFT

ter verkrijging van de graad van doctor
aan de Universiteit van Amsterdam,
op gezag van de Rector Magnificus
prof. dr. D.C. van den Boom
ten overstaan van een door het college voor promoties ingestelde
commissie, in het openbaar te verdedigen in de Agnietenkapel

op dinsdag 4 november 2008, te 14.00 uur

door

Bei Liu
geboren te Lanzhou, China

Promotiecommissie

Promotor:

- prof. dr. ir. B. Smit

Overige leden:

- prof. dr. P. G. Bolhuis
- prof. dr. A. Fasolino
- prof. dr. F. Kapteijn
- dr. E. J. Meijer
- prof. W. Wang

Faculteit der Natuurwetenschappen, Wiskunde en Informatica

The research reported in his thesis was carried out at the Van't Hoff Institute for Molecular Science, Faculty of Science, University of Amsterdam (Nieuwe Achtergracht 166, 1018 WV, Amsterdam, The Netherlands), and at the Centre Européen de Calcul Atomique et Moléculaire (CECAM; Ecole Normale Supérieure, 46 Allée d' Italie, 69007 Lyon, France), with financial support from the Dutch STW/CW Separation Technology program (700.56.655-DPC.6243).

Contents

Contents

1

Introduction

1.1 Zeolites and metal-organic frameworks

1.1.1 Zeolites

Inorganic microporous materials, typically known as zeolites, are an important class of materials, which are crystalline silicates or aluminosilicates with 3D microporous framework structures. The first zeolite was discovered by a Swedish mineralogist named Axel Fredrik Cronstedt in the 18th century who found that the stones rapidly lose water and seemed to boil upon heating them. Using the Greek words which mean "stone (*lithos*) that boils (*zein*)," he called this material zeolite [1].

In their common form, zeolites are based on TO_4 tetrahedra, where T is an aluminum or silicon atom. The Primary Buiding Units (PBU's) are the TO_4 tetrahedra, and they form Secondary Building Units (SBU's), like four rings (4R), five rings (5R), six rings (6R), eight rings (8R), double four rings (D4R), double six rings (D6R), double eight rings (D8R), etc., that contain up to 16 T atoms. These SBUs assembled together give rise to a large variety of different zeolites. Currently, more than 150 zeolite types have been synthesized and 48 naturally occurring zeolites are known [2].

In the zeolite frameworks, silicon and aluminum are bound to each other through shared O-atoms. The SiO_4 units (Si_4^+/O_4^-) are neutral but the AlO_4 units (Al_3^+/O_4^-) result in a net negative charge. The anionic character of the lattice caused by the presence of aluminum is compensated by protons and cations, such as Na^+, K^+, Ca^{2+}, Mg^{2+}, and others. These positive ions are rather loosely held and can readily be exchanged for other cations, leading to zeolites

exhibiting different adsorption, diffusion, and separation properties [3].

Owing to their structural and compositional features, zeolites can be used for a variety tasks.

a. Highly selective adsorbents

Zeolites have the potential of providing precise and specific separation of gases, including: (1) separation of gas mixtures according to the size and shape of the adsorbates. In this way, they adsorb only those molecules that their diameters are less than the pore apertures (using molecular sieving principle) or adsorb some adsorbates preferentially according to length, size, and configurational entropy [4]. Examples include separation of propane/propene by pure-silica small pore 8R zeolites [5-11], and separation of alkanes by MFI [4, 12, 13]; (2) selective adsorption of the polar or unsaturated molecules. A practical example is the separation of N_2 and O_2 in the air on zeolite A, by exploiting different polarities of the two molecules [14], and the removal of CO_2 and SO_2 from low-grade natural gas streams [15, 16].

b. Water purification and softening

Zeolites are widely used as ion-exchange beds in domestic and commercial water purification and softening. In these applications the mechanism is ion exchange to adsorb the calcium and magnesium found in tap water.

c. Heating and refrigeration

Zeolites can be used as solar thermal collectors and for adsorption refrigeration. In these applications, their high heat of adsorption and ability to hydrate and dehydrate while maintaining structural stability is exploited. This hygroscopic property coupled with an inherent exothermic reaction when transitioning from a dehydrated to a hydrated form (heat adsorption), making natural zeolites effective in the storage of solar and waste heat energy.

d. Petrochemical industry

The large internal surface, the thermal stability, and the presence of acid sites make zeolites an important class of catalytic materials for petrochemical applications, for instance, in fluid catalytic cracking and hydro-cracking. Zeolites confine molecules in small spaces, which causes changes in their structure and reactivity. The proton form of zeolites (prepared by ion-exchange) is powerful solid acids, and can facilitate a host of acid-catalyzed reactions, such as isomerisation, alkylation, and cracking.

From the above discussion, we can see that the widespread use of zeolites is mainly based on adsorption, diffusion, and catalysis. Although much experimental and theoretical research has been performed on investigating these properties, there are still many questions

left. For example, most of zeolite applications rely on the fact that the zeolite pores have dimensions that are comparable with the size of the molecules that can adsorb. To qualitatively and quantitatively explain why certain zeolites specifically adsorb one type of molecules and why certain ones are for a given application at the molecular level, reliable molecular models (force fields) are required. Many united-atom (UA) force fields [17-22] have been proposed for describing the adsorption and diffusion properties of alkanes in nanoporous framework structures. However, there are only two UA force fields dealing with the adsorption of alkenes in zeolites [23, 24]. In these two force fields tail corrections were used, which make them less practical to use in inhomogeneous systems [25, 26]. Most of the accurate alkane models do not use these tail corrections for adsorption and diffusion calculations in these types of systems. In this work we develop a similar type of force field for alkenes. In addition, it is well known that the presence of framework Al (non-framework cations/protons) influences the adsorption and the catalytic properties of the zeolites; however, the positions of the Al atoms and associated cations/protons distributions in many zeolites are still not clear and in this work we address the effects of non-framework ions on the adsorption properties at the molecular level.

1.1.2 Metal-organic frameworks

Metal-organic frameworks (MOFs) are a new family of hybrid porous materials that are formed by the coordination of metal ions with organic linkers. The first MOFs, reported by Robson and others in the early 1990s, typically consisted of single metal ions connected by simple tetrahedral or rod-shaped ligands, such as tetracyanophenylmethane or 4, 4-bipyridine [27-31], and had little or no practical applicability. The use of more varied organic linkers and the replacement of single metal ions with metal clusters have led to the synthesis of increasingly complex frameworks with a variety of applications [32-36].

Similar to zeolite structures, MOFs can be built up from either tetrahedral or octahedral building blocks and have 3D microporous channels and ultra-high specific surface areas. By a rational combination of different metal ions with different organic linkers, these materials feature opportunities for a large range of differences in functionality and structure. To date a large number of different MOFs have been synthesized which have shown various promising applications in, for example, gas storage, separation, or catalysis, etc. [37-39]

Among the various MOFs synthesized, a family with interpenetrated frameworks [40, 41] has shown potential applications for gas storage and separation. In this type of materials, additional small pores and adsorption sites are formed by the interpenetration of frameworks (the structure of IRMOF-9 [34] is shown in Figure 1.1 as an example), leading to MOFs with multi-pores of different sizes that exhibit different gases/gas mixtures adsorption, diffusion, and separation properties [41-47] compared with their non-interpenetrated counterparts [48,

49].

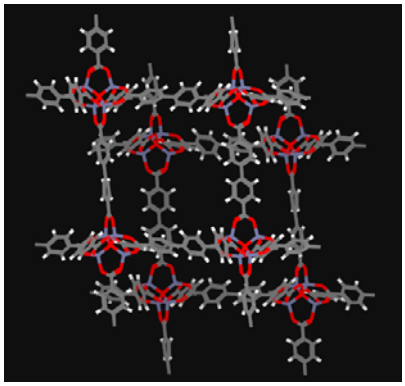

Figure 1.1: An example of MOFs (IRMOF-9)[34] with interpenetrated framework.

Currently, most theoretical [50-59] and experimental [60-62] investigations focus on non-interpenetrated MOFs and far less attention has been paid on the interpenetrated structures. To the best of our knowledge, neither experimental nor theoretical investigations have been performed on gas diffusion characteristics in such MOFs and the studies on the separation of gas mixtures in these MOFs are also very limited. In this work we address the question how the interpenetration influences the adsorption and diffusion properties of these materials.

Considering the importance of zeolites and MOFs in chemistry, physics, and materials science, it would be important to obtain a better understand of these materials at the molecular level using molecular simulations. This is the motivation for the works in this thesis. We set out to clarify these problems with a combination of different simulation techniques.

1.2 Simulation techniques

Owing to the rapid improvement in computer hardware over the last few years and the invention of sophisticated simulation techniques, molecular simulation is playing an increasingly important role in studying the properties of materials and the adsorption and diffusion behaviors of fluids confined in these materials [63]. It not only provides a cost-effective way of determining adsorption isotherms, diffusion coefficients, etc., especially under conditions not readily amenable to experiments (for example, at extreme temperatures or pressures), but also gives molecular-level details of the microstructure of the confined fluids, such as the molecular conformation, adsorption location, and diffusion trajectory enabling us to examine the underlying mechanisms that may be inaccessible by experiments.

In this section we briefly introduce several popular simulation techniques like Monte Carlo (MC) and Molecular Dynamics (MD) simulations in various ensembles (canonical, grand-canonical, and the Gibbs ensemble) and their applications. In addition, Dynamically Corrected Transition-State Theory is presented as well.

1.2.1 Monte Carlo simulations

The Metropolis algorithm

The Markov Chain Monte Carlo method is an important tool to generate a set of configurations that has a well defined distribution. In a Monte Carlo simulation, a Markov chain consists of a sequence of configurations and in practice, such a chain is generated by performing attempts to generate a new configuration, for example, by displacing a randomly selected particle and accepting or rejecting this move according the an appropriate acceptance rule. This acceptance rule can be derived from the condition of detailed balance [64]. If $P_B(o)$ and $P_B(n)$ denote the probability of finding the system in state (o) and (n), respectively, and $\alpha(o \to n)$ and $\alpha(n \to o)$ denote the conditional probability to perform a trial move from $o \to n$ and $n \to o$, respectively, then the probability $P_{acc}(o \to n)$ to accept the trial move from $o \to n$ is related to $P_{acc}(n \to o)$ by the condition of detailed balance:

$$P_B(o)\alpha(o \to n)P_{acc}(o \to n) = P_B(n)\alpha(n \to o)P_{acc}(n \to o) \tag{1.1}$$

In case the priori probability to generate a particular Monte Carlo move does not depend on the actual configuration, we have:

$$\alpha(o \to n) = \alpha(n \to o) \tag{1.2}$$

so the acceptance probability is

$$P_{acc}(o \to n) = \min\left(1, \frac{P_B(n)}{P_B(o)}\right) \tag{1.3}$$

If we are simulating the NVT ensemble the probability distribution is given by the Boltzmann distribution:

$$P_{NVT}(\Gamma^N) \propto \exp\left[-\beta U\left(\Gamma^N\right)\right] \tag{1.4}$$

where $\beta = \frac{1}{k_B T}$, Γ is the coordinate in phase space, and $U\left(\Gamma^N\right)$ is the potential energy of configuration Γ^N. If we substitute this expression in equation (1.3), we see that the

acceptance rule depends on the difference of the energy between the new and the old configuration. There are many acceptance rules that obey this condition. The choice of Metropolis *et al.* is:

$$acc(o \longrightarrow n) = \min\left(1, \exp\left\{-\beta\left[U(n) - U(o)\right]\right\}\right) \tag{1.5}$$

In conventional NVT Monte Carlo simulations the number of particles is constant. To compute an adsorption isotherm, which gives us the number of molecules inside the porous materials as a function of the pressure of the gas or liquid that is in contact with the porous materials, it is convenient to use the grand-canonical ensemble. In the grand-canonical ensemble the probability of find a particular configuration is:

$$P_{\mu VT}(\mathbf{s}^N; N) \propto \frac{\exp(\beta\mu N)V^N}{\Lambda^{3N} N!} \exp\left[-\beta U\left(\mathbf{s}^N\right)\right] \tag{1.6}$$

where Λ is the thermal de Broglie wavelength, μ is the chemical potential, and $\mathbf{s}^N$ are the reduced coordinates, i.e., $\mathbf{s} = \mathbf{r}/L$, where $\mathbf{r}$ is the coordinate and L is the length of the box. The characteristic of a grand-canonical Monte Carlo simulation is that one has to add or remove particles from the system. For example, by substituting equation (1.6) in equation (1.3), we see that the acceptance rule for the addition of a particle is:

$$acc(N \longrightarrow N+1) = \min\left(1, \frac{V}{\Lambda^3 (N+1)} \exp\left\{\beta\left[\mu - U(N+1) + U(N)\right]\right\}\right) \tag{1.7}$$

where $U(N+1) - U(N)$ is the energy of the additional particle that is added at a random position in the porous materials.

In a Monte Carlo simulation it is important that a sufficiently large number of moves are accepted. In the case of grand-canonical simulation, the insertion of a particle at a random position will be rejected if this particle is added on top of one of the atoms of the porous material or other adsorbed molecules. For small molecules like methane one can carry out a sufficiently large number of random insertions to find the "holes" in the porous material. However, for the long chain molecules random insertion becomes very inefficient as the probability that one of the atoms in the chains overlaps with the porous materials atoms increases enormously with chain length. Special techniques are therefore required to deal with these long chain molecules.

Configurational-bias Monte Carlo (CBMC)

As the fraction of successful insertions into the porous materials is very low for long-chain molecules, conventional Monte Carlo simulations become very time-consuming for these types of molecules. To increase the number of successfully inserted molecules we apply the

CBMC technique. In the CBMC scheme molecules are not inserted at random but grown atom by atom. This growing process introduces a bias which can be removed exactly by adjusting the acceptance rule [64].

To generate a new configuration of a molecule, we use the following steps based on the method developed by Rosenbluth and Rosenbluth [65]:

1. For the first atom, a random position in the porous materials is generated, and the energy of an atom at this position is calculated. This energy is denoted by U_1.

2. For the following atoms, say atom i, a set of k trial positions is generated. We denote these positions by $\mathbf{b} = (\mathbf{b}_1, \mathbf{b}_2, ..., \mathbf{b}_k)$. For each of these trial positions the energy is calculated with the atoms of the other molecules and with those atoms of the molecule that are already grown. This energy is denoted by $U_{\mathrm{i}}(\mathbf{b}_j)$.

3. Out of these k trial positions one is selected, say j, with a probability

$$P_i(\mathbf{b}_j)d\mathbf{b}_j = \frac{\exp[-\beta U_i(\mathbf{b}_j)]d\mathbf{b}_j}{w(i)} \tag{1.8}$$

in which

$$w(i) = \frac{1}{k}\sum_{j=1}^{k}\exp[-\beta U_i(\mathbf{b}_j)] \tag{1.9}$$

Eq. 1.8 ensures that those conformations with the lowest energy have the highest probability of being selected.

4. After repeating step 2 until the entire chain molecule of length M has been grown, we compute the Rosenbluth factor of the new configuration

$$W(n) = \exp(-\beta U_1)\prod_{i=2}^{M} w(i) \tag{1.10}$$

We use a similar algorithm to compute the Rosenbluth factor of the old conformation:

1. A molecule is selected at random and the energy of the first atom is calculated and is denoted by U_1.

2. For the following atoms, the external energy U_{i} is calculated and a set of k - 1 trial orientations is generated. Using this set of orientations and the actual position of atom $l, \mathbf{b}_1$,

we calculate

$$w(l) = \frac{1}{k}\left\{\exp\left[-\beta U_i(\mathbf{b}_1)\right] + \sum_{j=2}^{k}\exp\left[-\beta U_i(\mathbf{b}_j)\right]\right\} \tag{1.11}$$

3. After repeating step 2 until all M atoms of the chain molecule have been considered, we calculate for the entire molecule the Rosenbluth factor of the old conformation

$$W(o) = \exp(-\beta U_1)\prod_{i=2}^{M} w^{ext}(i) \tag{1.12}$$

We can use these algorithms to generate a new conformation and compute the Rosenbluth factors of the old and new configurations to perform canonical (NVT), grand-canonical (μVT), and Gibbs ensemble simulations. It is important that the bias, which is introduced by the selection of the most favorable conformation, is removed by appropriate acceptance rules. For example, for an NVT simulation one can use the CBMC scheme to remove a randomly selected molecule and regrow it at a random position in the porous materials; this move is not accepted or rejected on the basis of the energy difference (compare to equation (1.5)), but on the basis of the ratio of the Rosenbuth weights [64]:

$$acc(o \longrightarrow n) = \min\left(1, \frac{W(n)}{W(o)}\right) \tag{1.13}$$

The complete proof that this acceptance rule removes the bias exactly can be found in the literature [64]. Similar acceptance rules can be derived for the grand-canonical and Gibbs ensembles [64].

Computation of Henry coefficient and isosteric heat of adsorption

To study the adsorption in a given system, the initial task is always the determination of the Henry coefficient and the isosteric heat at zero loading as these variables give us an idea of the strength of the affinity between the adsorbate and the adsorbent. They tell us how much the adsorbate can adsorb under dilute conditions and how adsorption varies with temperature. Experimentally these variables are extracted from the measured adsorption isotherms at various temperatures. For calculating the Henry coefficient and the isosteric heat of adsorption at infinite dilution Q_{st}^0 of chain molecules in porous materials, simulations in the limit of zero loading are necessary. Regarding the simulations, zero loading means simulations with only one molecule present. The Henry coefficient can be calculated from [19]

$$K_H = \frac{1}{RT\rho_f}\frac{< W >}{< W^{IG} >} \tag{1.14}$$

and the isosteric heat of adsorption at infinite dilution Q_{st}^0 can be calculated from [19]

$$Q_{st}{}^0 = RT - \Delta U = RT - (< U_{hg} > - < U_h > - < U_g >) \tag{1.15}$$

where T is the temperature, R = 8.31451 J/(mol K) is the gas constant, and ρ_f in kg/m^3 is the density of the framework. The Rosenbluth factor of the single chain molecule in porous materials $< W >$, the Rosenbluth factor of the molecule in the ideal gas $< W^{IG} >$, the ensemble average of the potential energy of the host-guest system $< U_{hg} >$, the energy of the isolated chain molecule in the ideal gas $< U_g >$, and the average host energy $< U_h >$ (zero for a rigid framework) are computed from two independent simulations of a single chain: a NVT-simulation of a chain molecule adsorbed in the framework and a NVT simulation of an isolated chain in the ideal gas phase.

In the NVT ensemble, several Monte Carlo moves can be employed during a simulation [64, 66]:

1. Displacement move

A chain is selected at random and given a random displacement. The maximum displacement is taken such that 50% of the moves are accepted. The acceptance rule is

$$acc(o \longrightarrow n) = \min\left(1, \exp\left\{-\beta\left[U(n) - U(o)\right]\right\}\right) \tag{1.16}$$

2. Rotation move

A chain is selected at random and given a random rotation. The center of the rotation is the center of mass. The maximum rotation angle is chosen such that 50% of the moves are accepted. The acceptance rule is given by Eq. 1.16.

3. Full regrow move

A chain is selected at random and is completely regrown at a random position. This move is essential for NVT MC simulation as it changes the internal configuration of a molecule, and during this move the average Rosenbluth weight can be collected. The acceptance rule for full regrow is

$$acc(o \longrightarrow n) = \min\left(1, \frac{W(n)}{W(o)}\right) \tag{1.17}$$

4. Partial regrow move

A chain is selected at random and part of the molecule is regrown. It should be pointed out that

which part of the chain is regrown and with which segment the regrown is started are decided randomly. The acceptance rule for this move is given by Eq. 1.17.

The relative probabilities for attempting these moves are 10% displacements, 10% rotations, 10% partial regrowths, and 70% regrowths of the entire molecule.

Computation of adsorption isotherm by MC in μVT ensemble

In adsorption studies, one also likes to know at a given temperature the amount adsorbed as a function of the pressure. For calculating the adsorption isotherms of chain molecule, it is convenient to carry out simulations in the grand-canonical ensemble. In the grand-canonical ensemble the number of particles N can fluctuate, whereas the chemical potential μ (can be converted to pressure P), the temperature T, and the volume V are constant. Because these parameters are also constant in the experimental studies, the results obtained from simulations can be compared with experimental data directly. In addition to Monte Carlo moves mentioned in the above section, there are other moves that are employed during a simulation in this ensemble [64, 66]:

1. Insertion move

A chain is grown at a random position. The acceptance rule for insertion of the particle is

$$acc(N \longrightarrow N+1) = \min\left(1, \frac{\exp(\beta\mu^B)V}{\Lambda^3(N+1)} W(n)\right) \tag{1.18}$$

where μ^B is the chemical potential of a reservoir consisting of ideal chain (a chain that has only bonded interactions) molecules. .

2. Deletion move

A chain is chosen at random and the Rosenbluth factor of the old conformation $W(o)$ is computed. The acceptance rule for deletion of the particle is

$$acc(N \longrightarrow N-1) = \min\left(1, \frac{\Lambda^3 N}{V\exp(\beta\mu^B)} \frac{1}{W(o)}\right) \tag{1.19}$$

The relative probabilities for attempting these moves are 15% displacements, 15% rotations, 15% partial regrowths, and 55% exchanges with the reservoir.

Computation of vapor-liquid coexistence curve (VLCC) by MC in Gibbs ensemble

To test the accuracy of the interaction potentials, a good way is to check the VLCCs, as they are very sensitive to the choice of interaction potentials. Historically, the prediction of both vapor-liquid and liquid-liquid equilibria has relied almost exclusively on approximate theoretical models or on empirical equations of state rather than on rigorous models for intermolecular interaction at high fluid densities. The advent of the Gibbs-ensemble Monte Carlo method proposed by Panagiotopoulos [67, 68] provides us an opportunity to directly simulate the vapor-liquid coexistence curve.

In Panagiotopoulos's method, the two coexisting phases are simulated simultaneously in two separate boxes and hence, it avoids the interface between the two phases. The thermodynamic conditions for phase equilibria are equal chemical potential (μ), equal pressure (P), and equal temperature (T), i.e. chemical, mechanical, and thermal equilibrium. In the simulation we fix the difference in chemical potentials between the two coexisting phases, i.e., $\Delta\mu = \mu_{\mathrm{I}} - \mu_{\mathrm{II}} = 0$, and the difference in pressure $\Delta P = P_{\mathrm{I}} - P_{\mathrm{II}} = 0$, while the absolute values (P_{I}, P_{II}, μ_{I}, μ_{II}) are still undetermined. More precisely, the temperature, the total number of particles in the two boxes, and the total volume of the two boxes are kept fixed. In addition, the two systems can exchange particles and volume to ensure equal chemical potential and pressure between the two phases. A Gibbs-ensemble Monte Carlo simulation consists of three different trial moves [64]:

1. Particle displacement

One of the particles in box i = 1, 2 is selected at random and given a random displacement. The acceptance rule for this move is identical to the one used in a conventional NVT ensemble simulations (Eq. 1.16).

2. Volume exchange

In addition, we perform trial moves that consist of an attempted change of the old volume V_1(o) of box 1 to a new volume V_1(n) = V_1(o) + ΔV, while the volume of box 2 changes from V_2(o) to

V_2(n)= V_2(o) − ΔV. ΔV is a random number uniformly distributed over the interval [−$\Delta V_{\max}$, $\Delta V_{\max}$]. The acceptance rule for volume exchange is

$$acc(o \longrightarrow n) = \min\left(1, \left(\frac{V_1(n)}{V_1(o)}\right)^{N_1} \left(\frac{V_2(n)}{V_2(o)}\right)^{N_2} \exp(-\beta\Delta U_1)\exp(-\beta\Delta U_2)\right) \qquad (1.20)$$

where N_1 and N_2 are the number of particles in box 1 and box 2 and $\Delta U_i = U_i(n) - U_i(o)$ (i =1, 2) is defined as the energy difference in box i between state n and state o.

3. Particle exchange

The third trial move that is used in a Gibbs ensemble MC simulation is the exchange of particles. A new configuration is generated from the old configuration by removing a particle from box 1 and inserting this particle in box 2 (50% of the trials) or by removing a particle from box 2 and inserting this particle in box 1 (50%). The acceptance rule for the transfer of a particle from box 1 to box 2 is

$$acc(o \longrightarrow n) = \min\left(1, \frac{N_1 V_2}{(N_2+1)V_1} \exp(-\beta\Delta U_1) \exp(-\beta\Delta U_2)\right) \tag{1.21}$$

In a similar way, it can be derived that the acceptance rule for the transfer of a particle from box 2 to box 1 is

$$acc(o \longrightarrow n) = \min\left(1, \frac{N_2 V_1}{(N_1+1)V_2} \exp(-\beta\Delta U_1) \exp(-\beta\Delta U_2)\right) \tag{1.22}$$

Similar to the grand-canonical ensemble, for chain molecules this step has a prohibitively low acceptance, since a random insertion of a chain molecule in a box will almost always result in an overlap with one of the other chains. To make the exchange of chain molecules between the two boxes possible, we use the CBMC technique. Let us assume the system to be in state *o* with N_1 particles in box 1 with volume V_1 and we try to generate state *n* by moving a particle from box 2 into box 1. We use the algorithms of the CBMC section to grow a chain in box 1 and to calculate the Rosenbluth factor of the chain $W_1(n)$; at the same time we calculate the corresponding Rosenbluth factor for the chain that we chose to remove from box 2 $W_2(o)$. We then accept this move with probability [69, 70]

$$acc(o \longrightarrow n) = \min\left(1, \frac{N_2 V_1}{(N_1+1)V_2} \frac{W_1(n)}{W_2(o)}\right) \tag{1.23}$$

1.2.2 Molecular Dynamics simulations

The molecular dynamics technique is a scheme for studying the time evolution of a classical system of *N* particles in a volume *V*, following paths determined by Newton's laws. In contrast to MC simulations, which only yield thermodynamic ensemble averages, MD simulations can also provide transport properties of the system. An MD simulation is performed as follows:

1. Start with a configuration, i.e., select initial positions and velocities for all particles.
2. Calculate the forces on all particles.
3. Integrate Newton's equations of motion to obtain the new positions and velocities:

$$\mathbf{F}_i = m_i \times \frac{d\mathbf{v}_i}{dt} \tag{1.24}$$

$$\mathbf{v}_i = \frac{d\mathbf{r}_i}{dt} \tag{1.25}$$

in which $\mathbf{F}_i$, m_i, $\mathbf{v}_i$, and $\mathbf{r}_i$ are the total force, mass, velocity, and position of particle i, respectively.

For integrating the equation of motion in a MD simulation the velocity Verlet algorithm is probably the most widely used method:

$$\mathbf{r}(t+\Delta t) = \mathbf{r}(t) + \mathbf{v}(t)\Delta t + \frac{\mathbf{f}(t)}{2m}\Delta^2 t + \delta(\Delta^3 t) \tag{1.26}$$

$$\mathbf{v}(t+\Delta t) = \mathbf{v}(t) + \frac{\mathbf{f}(t) + \mathbf{f}(t+\Delta t)}{2m}\Delta t + \delta(\Delta^2 t) \tag{1.27}$$

where $\mathbf{r}(t)$, $\mathbf{v}(t)$, and $\mathbf{f}(t)$ are the position, velocity, and force at time t, respectively, Δt is the time step used, and m is the mass of the particle.

4. Repeat steps 2 and 3 until we have simulated the system sufficiently long such that thermodynamic and transport properties of the system can be computed.

When using simulations to calculate diffusivities, it is possible to compute two different types of diffusion coefficients: the self-diffusion coefficient D_S and the collective coefficient D_C.

Self-diffusion coefficient

The self-diffusion coefficient is a single particle property, which follows from the motion of a single tagged particle. In a simulation of a system of *N* particles, one can label each particle and hence obtains *N* data points for the self-diffusion coefficient. The self-diffusion coefficient can be expressed in terms of the autocorrelation function of the velocities of the particles:

$$D_s = \frac{1}{3N}\sum_{i=1}^{N}\int_0^\infty < v_i(t')v_i(0) > dt' \tag{1.28}$$

For a three-dimensional system, we can determine the self-diffusion coefficient for each dimension separately. For the *x*-direction, equation (1.28) becomes

$$D_s^x = \int_0^\infty < v_x(t) v_x(0) > dt \tag{1.29}$$

where $v_x(t)$ is the x coordinate of the velocity of a tagged molecule at time t. Since the tagged particle could be any particle in the system, we can average over all particles in our system to increase the accuracy of our calculation. Or alternatively, we can use the mean square displacement of a labeled particle. By taking the slope of the mean square displacement (msd) at long times, the self-diffusion coefficient can be computed as:

$$D_S^x = \frac{1}{2} \lim_{t \to \infty} \frac{d}{dt} \left\langle [x(t) - x(0)]^2 \right\rangle \tag{1.30}$$

where $x(t)$ is the x coordinate of the tagged molecule at time t. In a similar way we can compute the diffusion coefficients in the y and z directions, from which we can compute the overall diffusion coefficient D

$$D = \frac{D_x + D_y + D_z}{3} \tag{1.31}$$

This diffusion coefficient is measured in NMR experiments.

Collective diffusion coefficient

The collective diffusivity is the collective diffusion behavior of all adsorbate particles, including interparticle correlations. This implies that in a simulation of a system of N particles one obtains only a single data point for the collective diffusion coefficient, which makes the collective diffusion coefficient more difficult to compute compared to the self-diffusion coefficient calculations. An accurate calculation of this diffusion coefficient requires much longer simulations.

In the x direction, it can be computed in terms of the autocorrelation function of the velocities of the particles:

$$D_c^x = \frac{1}{N} \int_0^\infty \sum_{i=1}^N \sum_{j=1}^N < v_{xi}(t') v_{xj}(0) > dt' \tag{1.32}$$

or from the mean square displacement:

$$D_c^x = \frac{1}{2N} \lim_{t \to \infty} \frac{d}{dt} \left\langle \left(\sum_{i=1}^N [x(t) - x(0)] \right)^2 \right\rangle \tag{1.33}$$

Similar expressions can be written for the *y* and *z* direction and the overall collective diffusion coefficient is given by:

$$D_c = \frac{D_c^x + D_c^y + D_c^z}{3} \tag{1.34}$$

From a computational point of view there is no differences between using the mean square displacement or the velocity autocorrelation function; they give identical results.

In the limit of zero loading, adsorbate-adsorbate interactions becomes negligible and velocity correlations between different particles in equation (1.32) have little influence on the diffusion coefficient. We can rewrite equation (1.32) as the sum of velocity correlations between the same particle and between two different particles:

$$D_c^x = \frac{1}{N}\int_0^\infty \sum_{i=1}^N < v_{xi}(t')v_{xi}(0) > dt' + \frac{1}{N}\int_0^\infty \sum_{i=1}^N \sum_{j\neq i}^N < v_{xi}(t')v_{xj}(0) > dt' = D_s^x + \frac{1}{N}\int_0^\infty \sum_{i=1}^N \sum_{j\neq i}^N < v_{xi}(t')v_{xj}(0) > dt' \tag{1.35}$$

Therefore, in the limit of very low loading the collective diffusion coefficient and self-diffusion coefficient are equal.

1.2.3 Dynamically corrected Transition State Theory

In addition to MD, Transition State Theory (TST) has been used to study diffusion [71]. If we assumed that diffusion processes in confinement can be described as hopping events on a lattice, where the hopping from state A to another state B is limited by a free energy barrier between the two states; suppose that A and B are separated by a lattice distance λ; and if every particle crossing the barrier coming from A will equilibrate at B then we can assume that transition state theory holds and we can compute the hopping rate directly from the free energy barrier. However, if some of the particles cross the barrier in the direction to B, but fail to equilibrate in B - instead turning around and going back to A – a correction factor κ is needed to account for these recrossings. This is the so-called dynamical correction. The transmission rate $k_{A\to B}$ from state A to B is then given by [71]

$$k_{A\to B} = \kappa \times \sqrt{\frac{k_B T}{2\pi m}} \times \frac{\exp[-\beta F(q^*)]}{\int_{pore} \exp[-\beta F(q)]dq} \tag{1.36}$$

where k_B is Boltzmann's constant, *T* is the temperature of the system, *m* is the mass of the

hopping particle, $F(q)$ is the free energy as a function of q, and q^* denotes the (assumed) location of the barrier. When the particles perform a random walk on a lattice spanned by the porous material pore centers, this transmission rate $k_{A\to B}$ in turn can be converted to a self-diffusion coefficient D_s via:

$$D_s = k_{A\to B} \times \lambda^2 = \kappa \times \sqrt{\frac{k_B T}{2\pi m}} \times \frac{\exp[-\beta F(q^*)]}{\int_{pore} \exp[-\beta F(q)] dq} \times \lambda^2 = \kappa \times D_s^{TST} \tag{1.37}$$

In the above equation, D_s^{TST} is the free energy contribution to the self-diffusion coefficient, the part of the diffusion that is governed by free energy barriers: influences of the confinement topology on the diffusion of the gas molecules. κ is the transmission coefficient that be used for correcting for recrossing events, i.e. it corrects for trajectories which start from state A but fail to end up in state B [72].

By using Transition State Theory for calculating diffusion we need to compute free energy profiles, which can be obtained by performing NVT ensemble MC simulations using the histogram sampling (HS) method [71]. In the HS method, a histogram is made of the particle positions, mapped on the reaction coordinate q. This histogram can be converted into a relative free energy profile by using $\beta F(q) = -\ln < P(q) >$, where $P(q)$ denotes the probability to find a molecule at a given position q according to the histogram.

1.3 Force fields: Inter- and intramolecular potentials

It is commonly recognized that reliable force fields for the interatomic potentials play a key role in molecular simulations [4]. The force field is a set of functions that describe the interactions between the atoms in a molecular system. Most commonly used force field consists at least of bonded and non-bonded terms:

$$U^{\text{total}} = U^{\text{bonded}} + U^{\text{non-bonded}} \tag{1.38}$$

with

$$U^{\text{bonded}} = U^{\text{bond}} + U^{\text{bend}} + U^{\text{torsion}} + U^{\text{intra VDW}} \tag{1.39}$$

$$U^{\text{non-bonded}} = U^{\text{VDW}} + U^{\text{Coulomb}} \tag{1.40}$$

Many different force fields exist, such as the universal Force Field (UFF) [73], Dreiding and Dreiding II [74], Discover (CVFF) [75], Burchart [76], BKS [76], AMBER [77–81], CHARMM [82–86], or OPLS/Amber [87–90] etc.

These general force fields are not sufficiently accurate to quantitatively predict the

adsorption and diffusion in nanoporous systems. To provide an accurate representation of the interactions in these porous materials, many specific force fields [17-24, 57, 58, 91-94] have been proposed. For example, Vlugt et al. [17] proposed a united-atom force field for adsorption and diffusion of alkanes in zeolites; Dubbeldam *et al.* [18, 19] refined this force field further, able to faithfully reproduce the experimentally determined isotherms of alkanes in pure silica MFI-type zeolites and has extended it to pure silica TON-, AFI-, DDR-, and MWW-type zeolites successfully; Calero *et al.* [20-22] extended the force field of Dubbeldam *et al.* to take into account the effects of cations and protons, for alkanes in aluminosilicates. In addition to alkane-zeolite systems, several force fields for describing the adsorption and diffusion phenomena of alkenes [23, 24], CO_2 [91], and N_2 [91] in zeolites were proposed as well. The force fields describing the interactions of light gases (H_2, N_2, O_2, CO, CO_2, CH_4, C_2H_4, C_2H_6) with the atoms in MOFs have been proposed by Zhong and co-workers [57, 58, 92-94]. It should be pointed out that most of the above force fields are material-dependent.

1.4 Scope of this thesis

This thesis consists of two parts. The first part includes the studies of adsorption behavior of alkanes and alkenes in various zeolites and the second part is about the investigations of adsorption and diffusion behavior of light gases/gas mixtures in interpenetrated MOFs by using the simulation techniques described in the previous sections.

The first part of this thesis, chapters 2-5, describes the adsorption behavior of alkanes and alkenes in various pure silica zeolites and aluminosilicates. In chapter 2, we focused on investigating the adsorption behavior of alkanes in pure silica zeolites. A prerequisite for doing proper simulations is a high quality force field. Because most force fields are zeolite-dependent, it is of great usefulness if we can find a general force field applicable to most zeolites. In this chapter we tested the applicability of a united-atom force field for alkanes to various pure silica zeolites.

As most of the accurate alkane models do not use the tail corrections for doing proper adsorption and diffusion simulation in this type of systems, it is important to have a similar type of model for both alkanes and alkenes. In chapter 3, we developed a new united atom force field which accurately describes the adsorption properties of linear alkenes in zeolites. The force field developed for alkenes was specifically designed for use in the inhomogeneous system and therefore a truncated and shifted potential was used. With the determined force field, we performed a comparative study on the adsorption behaviors of alkenes in various pure silica zeolites.

Besides the researches carried out in the pure silica zeolites, we also investigated the

effect of the presence of cations/protons on the adsorption behaviors of hydrocarbons in aluminosilicates. It is well known that the presence of cations influences the adsorption and the catalytic properties of this type of zeolites. The type, density, and location of non-framework cations can be tailored by adjusting the Si/Al ratio and synthesis approaches, leading to tailored adsorption and catalytic properties. In chapter 4, the adsorption behaviors of linear alkanes in Na-MOR zeolites were studied in detail. The reason for selecting this system is that Mordenite (MOR), among the various zeolites, is a particularly useful zeolite for several catalytic applications, such as dewaxing of heavy petroleum fractions and cracking or isomerization of hydrocarbons [95]. In this chapter we validated a suitable force field for Na-MOR zeolites and we studied the relationship between sodium cations and the adsorption behavior of C_4-C_7 in this type of zeolites. In chapter 5, the most likely positions of aluminium in several zeolites were identified and we studied their different adsorption behaviors in detail. The structure of zeolites is composed of silicon and aluminium oxide tetrahedra and charge-balancing ions. As the presence of ions influences the adsorption properties of the zeolites and the positions and stability of ions in the zeolites are strongly related to their Al distributions, it is therefore important to identify the aluminium site locations.

The second part of this thesis, chapters 6 and 7, describes the adsorption and diffusion behavior of light gases/gas mixtures in MOFs. In chapter 6, we performed a combined molecular dynamics simulation and dynamically corrected transition state theory (dcTST) study to investigate the effect of interpenetration (catenation) on hydrogen diffusion in interpenetrated MOFs as well as their relationships. The reason why hydrogen was selected as the probe molecule in this work is that MOFs are a family of promising materials for hydrogen storage. In chapter 7, we investigated the effect of interpenetration on gas mixture (CH_4/H_2) separation in interpenetrated MOFs. We selected CH_4/H_2 system as the model mixture to separate since this is an important practical system that is involved in the process of purification of synthetic gas obtained from steam re-forming of natural gas. Currently, 95% of hydrogen used in fuel cells is produced by this method, and components such as methane must be removed from the synthetic gas before hydrogen can be used effectively [96].

Bibliography

[1] Oxford English Dictionary, 2nd ed., Simpson, J. and Weiner, E. (Ed.), Clarendon Press, Oxford, **1989**.

[2] International Zeolite Association, Structure Commission, http://www.iza-structure.org.

[3] Beerdsen, E.; Dubbeldam, D.; Smit, B.; Vlugt, T. J. H.; Calero, S. *J. Phys. Chem. B* **2003**, *107*, 12088.

[4] Krishna, R.; Smit, B.; Calero, S. *Chem. Soc. Rev.* **2002**, *31*, 185.

[5] Zhu, W.; Kapteijn, F.; Moulijn, J. A. *Chem. Commun.* **1999**, 2453.

[6] Zhu, W.; Kapteijn, F.; Moulijn, J. A.; den Exter, M. C.; Jansen, J. C. *Langmuir* **2000**, *16*, 3322.

[7] Olson, D. H.; Camblor, M. A.; Villaescusa, L. A.; Kuehl, G. H. *Micropor. Mesopor. Mater.* **2004**, *67*, 27.

[8] Olson, D. H. U. S. Patent No. 6, 488, 741, 2002.

[9] Olson, D. H.; Yang, X.; Camblor, M. A. *J. Phys. Chem. B* **2004**, *108*, 11044.

[10] Yang, X.; Toby, B. H.; Camblor, M. A.; Lee, Y.; Olson, D. H. *J. Phys. Chem. B* **2005**, *109*, 7894.

[11] Cantín, A.; Corma, A.; Leiva, S.; Rey, F.; Rius, J.; Valencia, S. *J. Am. Chem. Soc.* **2005**, *127*, 11560.

[12] Calero, S.; Smit, B.; Krishna, R. *J. Catal*. **2001**, *202*, 395.

[13] Calero, S.; Smit, B.; Krishna, R. *Phys. Chem. Chem. Phys.* **2001**, *3*, 4390.

[14] Nandi, S. P.; Walker, P. L. *Sep. Sci.* **1976**, *11*, 441.

[15] Delgado, J. A.; Uguina, M. A.; Gomez, J. M. *Sep. Pur. Tech.* **2006**, *48*, 223.

[16] Krishna, R.; van Baten, J. M. *Chem. Eng. J.* **2007**, *133*, 121.

[17] Vlugt, T.; Krishna, R.; Smit, B. *J. Phys. Chem. B* **1999**, *103*, 1102.

[18] Dubbeldam, D.; Calero, S.; Vlugt, T. J. H.; Krishna, R.; Maesen, T. L. M.; Beerdsen, E.; Smit, B. *Phys. Rev. Lett.* **2004**, *93*, 088302.

[19] Dubbeldam, D.; Calero, S.; Vlugt, T. J. H.; Krishna, R.; Maesen, T. L. M.; Smit, B. *J. Phys. Chem. B* **2004**, *108*, 12301.

[20] Calero, S.; Dubbeldam, D.; Krishna, R.; Smit, B.; Vlugt, T. J. H.; Denayer, J. F. M.; Martens, J.A.; Maesen, T. L. M. *J. Am. Chem. Soc.* **2004**, *126*, 11377.

[21] Calero, S.; Lobato, M. D.; García-Pérez, E.; Mejías, J. A.; Lago, S.; Vlugt, T. J. H.; Maesen, T. L. M.; Smit, B.; Dubbeldam, D. *J. Phys. Chem. B* **2006**, *110*, 5838.

[22] García-Pérez, E.; Dubbeldam, D.; Maesen, T. L. M.; Calero, S. *J. Phys. Chem. B*, **2006**, *110*, 23968.

[23] Granato, M. A.; Vlugt, T. J. H.; Rodrigues, A. E. *Ind. Eng. Chem. Res.* **2007**, *46*, 321.

[24] Jakobtorweihen, S.; Hansen, N.; Keil, F. J. *Mol. Phys.* **2005**, *103*, 471.

[25] Martin, M. G.; Thompson, A. P.; Nenoff, T. M. *J. Chem. Phys.* **2001**, *114*, 7174.

[26] Wilding, N. B.; Schoen, M. *Phys. Rev. E* **1999**, *60*, 1081.

[27] Hoskins, B. F.; Robson, R. *J. Am. Chem. Soc.* **1989**, *111*, 5962.

[28] Hoskins, B. F.; Robson, R. *J. Am. Chem. Soc.* **1990**, *112*, 1546.

[29] Abrahams, B. F.; Hoskins, B. F.; Liu, J. L.; Robson, R. *J. Am. Chem. Soc.* **1991**, *113*, 3045.

[30] Abrahams, B. F.; Hoskins, B. F.; Robson, R. *J. Am. Chem. Soc.* **1991**, *113*, 3606.

[31] Fujita, M.; Kwon, Y. J.; Washizu, S.; Ogura, K. *J. Am. Chem. Soc.* **1994**, *116*, 1151.

[32] Moulton, B.; Zaworotko, M. J. *Chem. Rev.* **2001**, *101*, 1629.

[33] Eddaoudi, M.; Moler, D. B.; Li, H.; Chen, B.; Reineke, T. M.; O'Keeffe, M.; Yaghi, O. M. *Acc. Chem. Res.* **2001**, *34*, 319.

[34] Eddaoudi, M.; Kim, J.; Rosi, N.; Vodak, D.; Wachter, J.; O'Keeffe, M.; Yaghi, O. M. *Science* **2002***, 295*, 469.

[35] Kitagawa, S.; Kitaura, R.; Noro, S.-I. *Angew. Chem., Int. Ed.* **2004**, *43*, 2334.

[36] Ockwig, N. W.; Delgado-Friedrichs, O.; O'Keeffe, M.; Yaghi, O. M. *Acc. Chem. Res.* **2005**, *38*, 176.

[37] Rowsell, J. L. C.; Yaghi, O. M. *Angew. Chem. Int. Ed*. **2005**, *44*, 4670.

[38] Férey, G. *Chem. Soc. Rev.* **2008**, *37*, 191.

[39] Mueller, U.; Schubert, M.; Teich, F.; Puetter, H.; Schierle-Arndt, K.; Pastré, J. *J. Mater. Chem.* **2006**, *16*, 626.

[40] Kesanli, B.; Cui, Y.; Smith, M. R.; Bittner, E. W.; Bockrath, B. C.; Lin, W. *Angew. Chem. Int. Ed.* **2005**, *44*, 72.

[41] Chen, B.; Ma, S.; Hurtado, E. J.; Lobkovsky, E. B.; Zhou, H. C. *Inorg. Chem.* **2007**, *46*, 8490.

[42] Ma, S.; Sun, D.; Ambrogio, M.; Fillinger, J. A.; Parkin, S.; Zhou, H. C. *J. Am. Chem. Soc.* **2007**, *129*, 1858.

[43] Rowsell, J. L. C.; Yaghi, O. M. *J. Am. Chem. Soc.* **2006**, *128,* 1304.

[44] Chen, B.; Ma, S.; Zapata, F.; Lobkovsky, E. B.; Yang, J. *Inorg. Chem.* **2006**, *45*, 5718.

[45] Chen, B.; Liang, C.; Yang, J.; Contreras, D. S.; Clancy, Y. L.; Lobkovsky, E. B.; Yaghi, O. M.; Dai, S. *Angew. Chem. Int. Ed.* **2006**, *45*, 1390.

[46] Bastin, L.; Bárcia, P. S.; Hurtado, E. J.; Silva, J. A. C.; Rodrigues, A. E.; Chen, B. *J. Phys. Chem. C* **2008,** *112,* 1575.

[47] Bárcia, P. S.; Zapata, F.; Silva, J. A. C.; Rodrigues, A. E.; Chen, B. *J. Phys. Chem. B* **2007**, *111*, 6101.

[48] Kubota, Y.; Takata, M.; Matsuda, R.; Kitaura, R.; Kitagawa, S.; Kato, K.; Sakata, M.; Kobayashi, T. C. *Angew. Chem. Int. Ed.* **2005**, *44*, 920.

[49] Kayes, S. S.; Long, J. R. *J. Am. Chem. Soc.* **2008**, *130*, 806.

[50] Fost, H.; Düren, T.; Snurr, R. Q. *J. Phys. Chem. B* 2006, *110*, 9565.

[51] Walton, K. S.; Millward, A. R.; Dubbeldam, D.; Frost, H.; Low, J. J.; Yaghi, O. M.; Snurr, R. Q. *J. Am. Chem. Soc.* **2008**, *130*, 406.

[52] Ramsahye, N. A.; Maurin, G.; Bourrelly, S.; Llewellyn, P. L.; Serre, C.; Loiseau, T.; Devic, T.; Ferey, G. *J. Phys. Chem. C* **2008**, *112*, 514.

[53] Düren, T.; Sarkisov, L.; Yaghi, O. M.; Snurr, R. Q. *Langmuir* **2004,** *20,* 2683.

[54] Liu, J.; Culp, J. T.; Natesakhawat, S.; Bockrath, B. C.; Zande, B.; Sankar, S. G.; Garberoglio, G.; Johnson, J. K. *J. Phys. Chem. C* **2007,** *111,* 9305.

[55] Yang, Q.; Xue, C.; Zhong ,C.; Chen, J. *AIChE J.* **2007**, *53*, 2832.

[56] Keskin, S.; Sholl, D. S. *J. Phys. Chem. C* **2007**, *111*, 14055.

[57] Yang, Q.; Zhong ,C. *J. Phys. Chem. B* **2006**, *110*, 17776.

[58] Yang, Q.; Zhong, C. *ChemPhysChem* **2006**, *7*, 1417.

[59] Düren, T.; Snurr, R. Q. *J. Phys. Chem. B* **2004**, *108*, 15703.

[60] Latroche, M.; Surblé, S.; Serre, C.; Mellot-Draznieks, C.; Llewellyn, P. L.; Lee, J. H.; Chang, J. S.; Jhung, S. H.; Férey, G. *Angew. Chem. Int. Ed*. **2006**, *45*, 8227.

[61] Li, Y.; Yang, R. T. *J. Am. Chem. Soc.* **2006**, *128*, 8136.

[62] Kaye, S. S.; Dailly, A.; Yaghi, O. M.; Long, J. R. *J. Am. Chem. Soc.* **2007**, *129*, 14176.

[63] Catlow, C. R. A.; van Santen, R. A.; Smit, B. *Computer Modelling of Microporous Materials*; Elsevier Science: Amsterdam, **2004**.

[64] Frenkel, D.; Smit, B. *Understanding Molecular Simulations: From Algorithms to Application*s, 2nd ed.; Academic Press: San Diego, CA, **2002**.

[65] Rosenbluth, M.; Rosenbluth, A. *J. Chem. Phys.* **1955**, *23*, 356.

[66] Dubbeldam, D. *Computer-simulation of Adsorption and Diffusion of Hydrocarbons in Zeolites*, PhD thesis, University of Amsterdam, **2005**.

[67] Panagiotopoulos, A. Z. *Mol. Phys.* **1987**, *61*, 813.

[68] Panagiotopoulos, A. Z.; Quirke, N.; Stapleton, M.; Tildesley, D. J. *Mol. Phys.* **1988**, *63*, 527.

[69] Mooij, G. C. A. M.; Frenkel, D.; Smit, B. *J. Phys.: Condens. Matter* **1992**, *4*, L255.

[70] Smit, B.; Karaborni, S.; Siepmann, J. I. *J. Chem. Phys.* **1995**, *102*, 2126.

[71] Beerdsen, E. *On Diffusion in Zeolites - A simulation Study*, PhD thesis, University of Amsterdam, **2007**.

[72] Beerdsen, E.; Dubbeldam, D.; Smit, B. *J. Phys. Chem. B* **2006**, *110*, 22754.

[73] Rapp´e, A. K.; Casewit, C. J.; Colwell, K. S.; Goddard, W. A.; Skiff, W. M. J. *J. Am. Chem. Soc.* **1992**, *114*, 10024.

[74] Mayo, S. L.; Olafson, B. D.; Goddard, W. A. *J. Phys. Chem.* **1990**, *94*, 8897.

[75] Dauber-Osguthorpe, P.; Roberts, V. A.; Osguthorpe, D. J.; Wolff, J.; Genest, M.; Hagler, A. T. *Proteins: Structure, Function and Genetics* **1988**, *4*, 31.

[76] de Vos Burchart, E.; Verheij, V. A.; van Bekkum, H. *Zeolites* **1989**, *9*, 432.

[77] Cornell,W. D.; Cieplak, P.; Bayly, C. I.; Gould, I. R.; Merz Jr., K. M.; Ferguson, D. M.; Spellmeyer, D. C.; Fox, T.; Caldwell, J.W.; Kollman, P. A. *J. Am. Chem. Soc.* **1992**, *117*, 5179.

[78] Pearlman, D. A.; Case, D. A.; Caldwell, J. C.; Seibel, G. L.; Singh, U. C.; Weiner, P.; Kollman, P. A., *AMBER 4.0* University of California Press; San Francisco, **1991**.

[79] Weiner, P. K.; Kollman, P. A. *J. Comp. Chem.* **1981**, *2*, 287.

[80] Weiner, S. J.; Kollman, P. A.; Case, D. A.; Singh, U. C.; Ghio, C.; Alagona, G.; Profeta Jr., S.; Weiner, P.K. *J. Am. Chem. Soc.* **1984**, *106*, 765.

[81] Weiner, S. J.; Kollman, P. A.; Nguyen, D. T.; Case, D. A. *J. Comp. Chem.* **1986**, *7*, 230.

[82] Brooks, B. R.; Bruccoleri, R. E.; Olafson, B. D.; States, D. J.; Swaminathan, S.; Karplus, M. *J. Comp. Chem.* **1983**, *4*, 187.

[83] Feller, S. E.; Yin, D. X.; MacKerell, R.W. Pastor A. D. *Biophys. J.* **1997**, *73*, 2269.

[84] MacKerell, A. D.; Bashford, D.; Bellott, M.; Dunbrack, R. L.; Evanseck, J. D.; Field, M. J.; Fischer, S.; Gao, J.; Guo, H.; Ha, S.; Joseph-McCarthy, D.; Kuchnir, L.; Kuczera, K.; Lau, F. T. K.; Michnick, C.Mattos S.; Ngo, T.; Nguyen, D. T.; Prodhom, B.; Reiher, W. E.; Roux, B.; Schlenkrich, M.; Smith, J. C.; Stote, R.; Straub, J.; Watanabe, M.; Wiorkiewicz-Kuczera, J.; Yin, D.; Karplus, M. *J. Phys. Chem. B* **1998**, *102*, 3586.

[85] Momany, F. A.; Rone, R. *J. Comp. Chem.* **1992**, *13*, 888.

[86] Pavelites, J. J.; Gao, J.; Bash, P.A.; Mackerell Jr., A. D. *J. Comp. Chem.* **1997**, *18*, 221.

[87] Damm, W.; Frontera, A.; Tirado-Rives, J.; Jorgensen, W. L. *J. Comp. Chem.* **1997**, *18*, 1955.

[88] Jorgensen, W. L.; Maxwell, D. S.; Tirado-Rives, J. *J. Am. Chem. Soc.* **1996**, *118*, 11225.

[89] Jorgensen, W. L.; Tirado-Rives, J. *J. Am. Chem. Soc.* **1988**, *110*, 1657.

[90] Kaminski, G.; Duffy, E. M.; Matsui, T.; Jorgensen, W. L. *J. Phys. Chem.* **1994**, *98*, 13077.

[91] García-Pérez, E.; Parra, J. B.; Ania, C. O.; Garcia-Sanchez, A.; van Baten, J. M.; Krishna, R.; Dubbeldam, D.; Calero, S. *Adsorption* **2007**, 13, 469.

[92] Yang, Q.; Zhong, C. *J. Phys. Chem. B* **2005**, *109*, 11862.

[93] Yang, Q.; Zhong, C.; Chen, J. F. *J. Phys. Chem. C* **2008**, *112*, 1562.

[94] Wang, S.; Yang, Q.; Zhong, C. *Sep. Purif. Technol.* **2008**, *60*, 30.

[95] van Bokhoven, J. A.; Tromp, M.; Koningsberger, D. C.; Miller, J. T.; Pieterse, J. A. Z.; Lercher, J. A.; Williams, B.A.; Kung, H. H., *J.Catal.*, 2001, **202**, 129.

[96] Mitchell, M. C.; Gallo, M.; Nenoff, T. M. *J. Chem. Phys.* **2004**, *121*, 1910.

The recently proposed united atom force field by Dubbeldam *et al*. (*Phys. Rev. Lett.*, 2004, 93, 088302) for the adsorption of alkanes in MFI-type zeolites was extended to other zeolites in this work. Its applicability to FER-type zeolites was evaluated in detail, for which the Henry coefficients, the isosteric heat of adsorption, the adsorption isotherms as well as the locations of alkanes in the FER-type zeolites were computed and compared with experimental values. The results show that the new force field works well for FER zeolites. Furthermore, its applicability to MWW-, MTW-, CFI-, LTA-, and STF-type zeolites was investigated, and we found that the experimental isotherms could be accurately predicted except for STF-type zeolites. This work shows that the new united atom force field proposed by Dubbeldam *et al*. is applicable to most pure silica zeolites.

B. Liu, B. Smit, and S. Calero[*]

Evaluation of a New Force Field for Describing the Adsorption Behavior of Alkanes in Various Pure Silica Zeolites

2.1 Introduction

Zeolites are microporous materials that have found wide applications as efficient heterogeneous catalysts and adsorbents in the petrochemical industry, for which the adsorption of hydrocarbons in zeolite pores plays an important role. Therefore, it is of importance to explore the adsorption behavior of hydrocarbons in different zeolites from both scientific and practical points of view. In addition to experiment, molecular simulation has been proved a useful tool to investigate the properties of fluids confined in porous materials [1]. It not only provides a cost-effective way of determining adsorption isotherms, especially under conditions not readily amenable to experiments, but also gives molecular-level details of the microstructure of the confined fluids, such as the molecular conformation and adsorption location to enable one to examine the underlying physics that may be inaccessible by experiments.

It is commonly recognized that reliable force fields for the interatomic potentials play a key role in molecular simulations [2]. As a result, many force fields [3-7] have been proposed for the interactions between the adsorbates and the zeolite framework and for the adsorbate-adsorbate interactions. Most force fields are zeolite-dependent, and a general force field applicable to most zeolites is of practical importance. Recently, Dubbeldam *et al.* [8, 9] developed a united-atom force field, able to accurately and quantitatively describe the

[*] Liu, B.; Smit, B.; Calero, S. *J. Phys. Chem. B* **2006**, *110*, 20166.

adsorption properties of alkanes in nanoporous framework structures. This force field faithfully reproduces the experimentally determined isotherms (particularly the inflection points) in pure silica MFI-type zeolites and has been successfully extended to TON-, AFI-, DDR-, and MWW-type zeolites. It seems that this force field is promising to become a force field applicable to most types of pure silica zeolites, and thus, in this work we test its applicability to other pure silica zeolites not considered previously to come a conclusion.

The aim of this work is twofold. The first one is to check whether the recently proposed united-atom force field by Dubbeldam *et al*. [8, 9] correctly predicts the adsorption isotherms of FER-type zeolites. The reason why FER is chosen is that the *n*-alkanes tightly fit in the pores of FER and the adsorption is therefore very sensitive to the details of the force field [10-12]. Pascual *et al.* [13, 14] pointed out that the united-atom (UA) force fields are questionable for describing the adsorption of alkanes in FER-type zeolites and attributed this to the approximations in the UA force field. The more complex anisotropic united atom (AUA) potential scheme was used in their work. Therefore, it is worth performing a systematic study for *n*-alkane-FER system by using the new UA force field of Dubbeldam *et al.* The second aim is to check the applicability of this force field to other pure silica zeolites to evaluate whether it can serve as a general force field for most structures.

2.2 Simulation models and methods

2.2.1 Zeolite models

In the simulations, zeolites were constructed using the atomic coordinates reported in refs. [15-20] and some details of these structures are summarized in Table 2.1. The zeolite lattices were assumed to be rigid in the simulations, because the flexibility of the framework has a negligible influence on the adsorption of alkanes [22].

Zeolite	IZA Code[21]	Structure, Pore dimension (Å)	Unit cell (Å)	Simulation cell size (Å)		
				x	y	z
ferrierite	FER	10, 5.4×4.2 8, 4.8×3.5	a=19.156, b=14.127, c=7.489	38.312	28.254	29.956
ZSM-12	MTW	12, 6.0×5.6	a=24.863, b=5.012, c=24.326	49.726	40.096	48.652
ITQ-1	MWW	10, 7.1×18.0 10, 4.0×5.5	a=24.447, b=14.114, c=24.882	24.447	28.228	24.882
CIT-5	CFI	14, 7.3×7.55	a=13.695, b=5.021, c=25.497	41.085	30.126	50.994
ITQ-29	LTA	supercages,11.8	a=11.867	47.468	47.468	47.468
SSZ-35	STF	10, 5.5×6.1 18, 12.5×9	a=11.411, b=11.526, c=7.377	34.233	34.578	36.885

Table 2.1: Structural information for the pure-silica zeolites considered in this work.

2.2.2 Force field

The force field used in this work is the united-atom force field proposed by Dubbeldam *et al*. [8, 9] The alkanes are described with a united-atom model, in which CH_3 and CH_2 groups are considered as single interaction centers [23]. The beads in the chain are connected by harmonic bonding potentials. A harmonic cosine bending potential models the bond bending between three neighboring beads, and a Ryckaert-Bellemans potential controls the torsional angle. The interactions between the adsorbates as well as the adsorbates and the zeolite are described by Lennard-Jones potentials. For a detailed description of the force field, the reader is referred to Ref. 9.

2.2.3 Simulation technique

For the calculation of the Henry coefficients and the isosteric heats of adsorption at infinite dilution Q_{st}^0, we performed configurational-bias Monte Carlo (CBMC) simulations in the *NVT* ensemble. Each simulation consists of at least 4×10^7 cycles and in each cycle one move is chosen at random with a fixed probability 0.1 for a molecule translation, 0.1 for rotation around the center of mass, and 0.8 for regrowth of the entire molecule. During the simulation we compute the Rosenbluth factor and the internal energy ΔU, which are directly related to the Henry coefficient and Q_{st}^0, respectively [24, 25].

Adsorption isotherms were calculated in the grand-canonical ensemble using the CBMC method. The CB-GCMC method simulates an open system specified by fixed temperature *T*, volume *V*, and fugacity *f*. We converted the imposed fugacity to the corresponding pressure using the Peng-Robinson equation of state. Four types of moves were carried out: translation, rotation, exchange of molecules between the zeolite and a molecule reservoir, and partial regrowths. All simulations included at least 2×10^7 cycles.

The statistical uncertainty was estimated by dividing each run into 5 blocks and calculating the standard deviation from the block averages. The standard deviation is within ± 10 % for every simulation. A detailed description of the simulation methods can be found in our previous work [9].

2.3 Results and discussion

2.3.1 Validation of the applicability of the new force field to ferrierite (FER topology) zeolites

As a first step towards validation of the applicability of the force field proposed by Dubbeldam *et al.* to ferrierite zeolites, the Henry coefficients of C_1-C_3 and the isosteric heat of adsorption Q_{st}^0 of C_1-C_6 were calculated and compared with experimental [26, 27] and simulation [14, 28] results, as shown in Table 2.2 and Figure 2.1. The force field shows improved or comparable results with previous simulations and the agreement with the experimental values is also

satisfactory considering the fact that the experiments have been performed in the protonated ferrierite samples. It has been shown that the presence of the protons can give a negative contribution to the heat of adsorption of up to 10 kJ/mol for H-MFI and H-MOR [29, 30].

	CH_4		C_2H_6		C_3H_8	
	K_H	Q_{st}^0	K_H	Q_{st}^0	K_H	Q_{st}^0
experimental data[26]	2.0×10^{-5}	27.7	7.2×10^{-4}	41.7	-	53.3
this work	9.38×10^{-6}	21.43	2.3×10^{-4}	33.43	1.51×10^{-3}	44.27
Ndjaka *et al.* (simulation data)[28]	7.2×10^{-6}	21.6	1.9×10^{-4}	34.2	9.1×10^{-4}	43.9

Table 2.2: Henry coefficients K_H [mmol/g/Pa] and isosteric heats of adsorption at infinite dilution Q_{st}^0 [kJ/mol] of C_1-C_3 in FER-type zeolites.

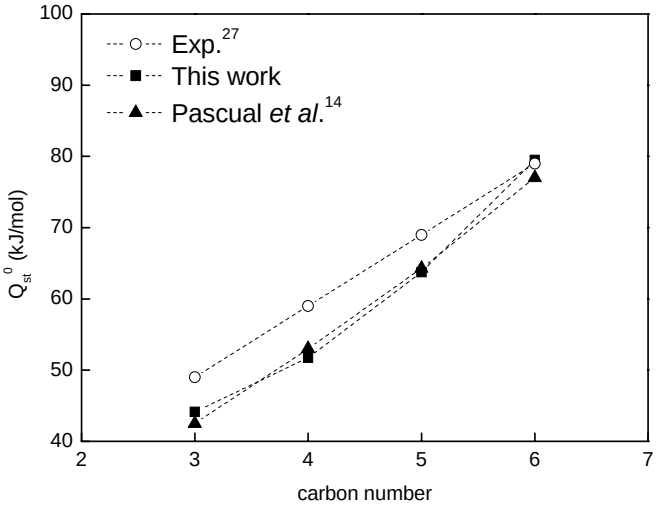

Figure 2.1: Heats of adsorption of linear alkanes in FER as a function of the carbon number, as compared to experiments and previous simulations.

To test the applicability of the force field further, the adsorption isotherms of C_1-C_6 were computed and compared with experimental data [11, 26, 27] and previous simulation results [12-14], as shown in Figures 2.2a-f. It should be pointed out that all the adsorption isotherms were measured in the protonated ferrierite samples, and no measurements in pure silica ferrierite samples have been performed.

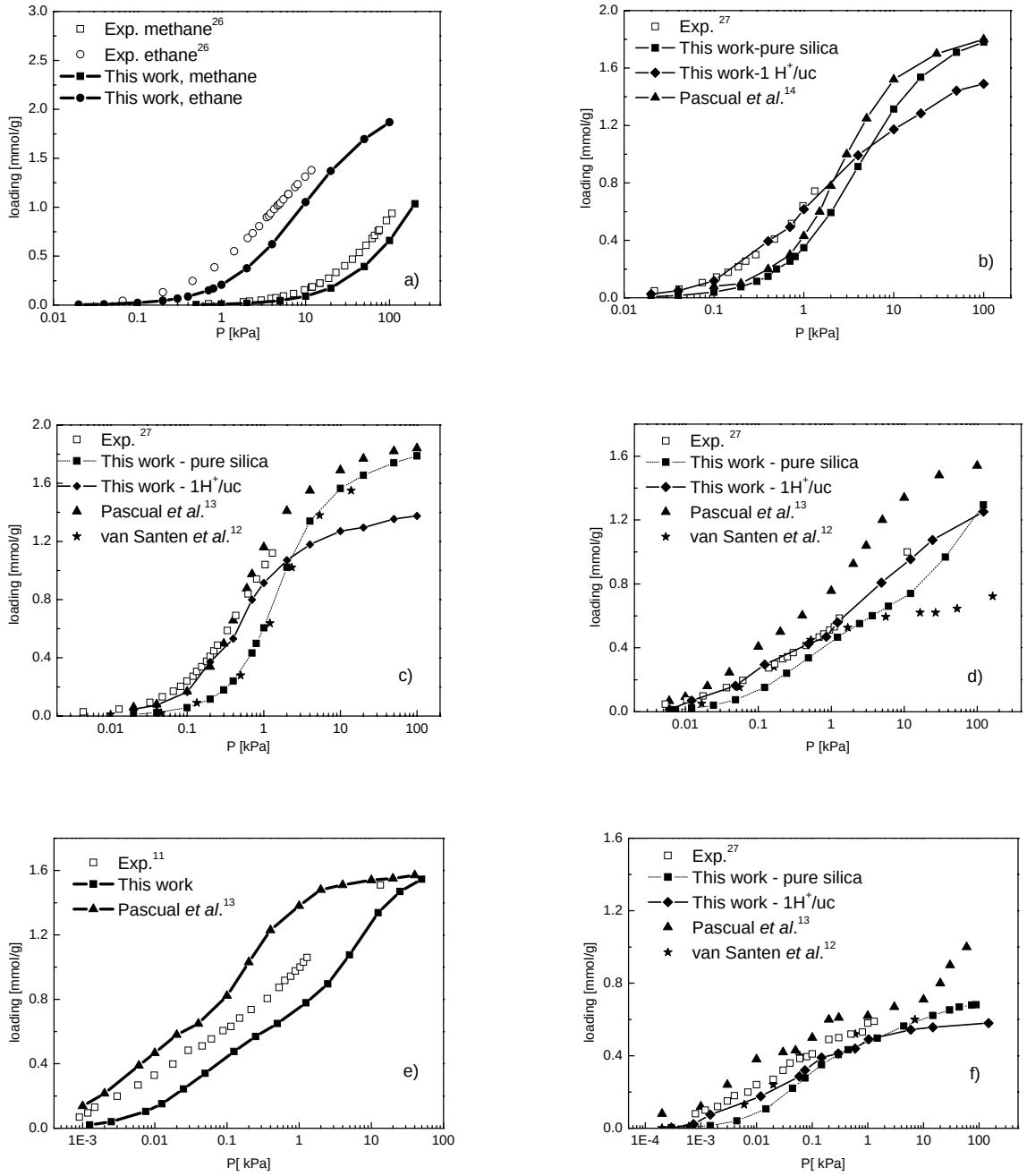

Figure 2.2: Comparison of the experimental and simulated adsorption isotherms of a) methane and ethane, b) propane, c) *n*-butane, d) *n*-pentane-333K, e) *n*-pentane-298K, and f) *n*-hexane in ferrierite zeolite at various temperatures.

Figure 2.2a shows the computed adsorption isotherms of methane and ethane at 309 K. Our simulations give lower values for the loading than the experimental observations and similar deviations have been observed by other simulations using a different force field [28]. The computed isotherms for propane at 333 K are shown in Figure 2.2b, and a good agreement with Pascual *et al.*'s simulation results is obtained for the adsorption in pure silica FER. In the case of *n*-butane, the isotherm in pure silica structure agrees well with the simulation results of van Santen *et al.* [12]; however, we obtain lower values for the amount adsorbed compared to

both the experimental and simulation results of Pascual *et al.* [13]. The adsorption isotherms for *n*-pentane at 333 K and 298 K are shown in Figures 2.2d and 2.2e, respectively. We found that our UA force field faithfully reproduces the experimental type-I isotherms. The simulations of van Santen and co-workers suggested a stepped isotherm, which disagrees with the experimental data. Figure 2.2f shows the adsorption isotherms for *n*-hexane at 333 K. A difference on the shape of the simulated adsorption isotherms was found. Pascual *et al.* predicted that hexane molecules could adsorb in the 8-ring cages when the pressure is higher than 10 kPa, which has not been confirmed by experiments. In contrast, our simulation shows that, before the bulk saturation pressure being reached, hexane molecules can only adsorb in the 10-ring channels, as shown in Figure 2.3, which is consistent with the experimental observations [11, 31-33].

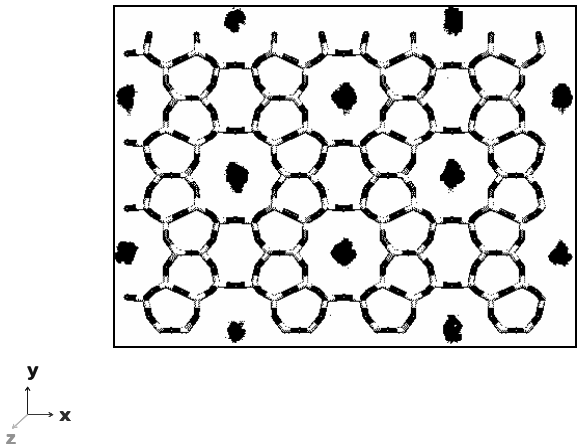

Figure 2.3: Distribution of hexane in FER zeolites at 74 kPa and 333 K. The centers of mass of the hexane molecules are represented by black dots.

Figures 2.2a-f show that our simulations, which are based on the new UA force field, give systematic lower adsorption capacities in pure silica FER-type zeolite than the experimental values for all the alkanes tested. This might be attributed to the presence of protons in the experimental zeolite samples. To test this hypothesis we performed some simulations using the force field of Calero *et al.* [30]. This force field is an extended version of the force field of Dubbeldam *et al.* that takes into account the effects of protons, for alkanes in protonated zeolites, as shown in Figures 2.2b-2.2d, and 2.2f. For Figures 2.2a and 2.2e the experiments are for zeolites with a different Si/Al ratios compared to the other isotherms in FER. For these zeolites the proton distribution is much more complex, since there are four distinct T-sites aluminum can be located and the positions and stability of protons in the zeolites are strongly related to its Al distribution. Our simulations show that the adsorption properties are very sensitive to the exact location of Al [34]; however, in this work only the structure that gives best agreement with the experimental data is presented. Figure 2.2 shows that indeed this shift could be explained by the presence of protons. We could also have shown results for different Al distributions that are less successful, which makes it very difficult to conclude that protons are the only explanation. However, these results do show that the disagreement with the experimental data does not necessarily imply difficulties with the force

field of Dubbeldam *et al*. On the other hand, the simulated results of Pascual *et al.* show that the presence of protons can increase the adsorption capacity of propane, the effects are negligible for n-butane, and it decreases the adsorption capacity of *n*-pentane and *n*-hexane. However, from the physical point of view one would expect that protons will affect the adsorption of alkanes in a similar way. Therefore, our simulations using the new force field give more reasonable results as compared with those of Pascual *et al.* These results together with those of Henry coefficients and heats of adsorption show that the UA force field of Dubbeldam *et al.* is applicable to the characterization of FER-type zeolites. Unlike the statement of Pascual *et al.* [13, 14] that the UA force fields are questionable for describing the adsorption of alkanes in FER-type zeolites, this work shows that UA force fields are workable for this type of systems.

2.3.2 Validation of the applicability of the new force field to other pure silica zeolites

In addition to the ferrierite zeolites, the applicability of this force field to ITQ-1 (MWW), ZSM-12 (MTW), CIT-5 (CFI), ITQ-29 (LTA), and SSZ-35 (STF) zeolites were further examined in this work. The results of the simulations at infinite dilution are given in Tables 2.3 and 2.4, and the results for the adsorption isotherms are shown in Figures 2.4-2.6. In both cases the results are compared with the experiments of Savitz *et a*l. [26], Du *et al*. [35], Guil *et a*l. [36], and Gribov *et al* [37]. It should be pointed out that all the experimental data used were measured in pure silica samples.

	CH_4		C_2H_6		C_3H_8	
	this work	Exp.[26]	this work.	Exp.[26]	this work	Exp.[26]
K_H [mmol/g/Pa]	3.6×10^{-6}	4.0×10^{-6}	6.9×10^{-5}	9.3×10^{-5}	4.0×10^{-6}	-
Q_{st}^0 [kJ/mol]	18.5	20.9	28.1	29.5	37.5	37.6

Table 2.3: Henry coefficients K_H and isosteric heats of adsorption at infinite dilution Q_{st}^0 of C_1-C_3 in MTW-type zeolites.

zeolite	this work	Exp.[37]	Cal.[37]
ZSM-12(MTW)	71.98 ± 0.63	72	64.2 ± 2.5
CIT-5(CFI)	51.90 ± 0.20	46	55.6 ± 0.4
ITQ-29(LTA)	46.62 ± 0.40	39	46.6
SSZ-35(STF)	52.04 ± 0.17	57	54.4 ± 2.6

Table 2.4: Heats of hexane adsorption in four zeolites.

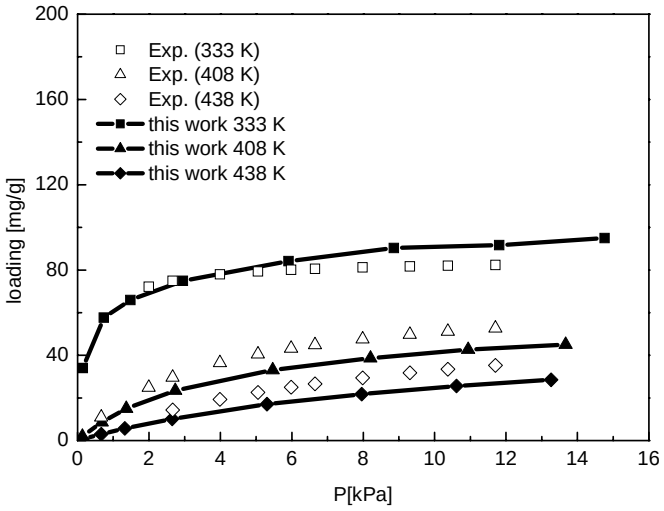

Figure 2.4: Comparison of the experimental [35] and simulated adsorption isotherms of *n*-hexane in ITQ-1 zeolite.

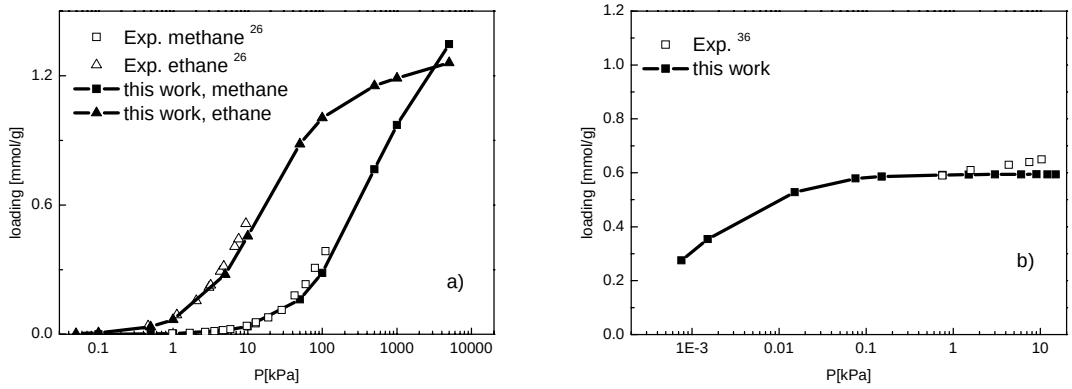

Figure 2.5: Comparison of the experimental and simulated adsorption isotherms of a) methane and ethane and b) *n*-hexane in ZSM-12 zeolite.

Figure 2.4 shows our simulation results for hexane at various temperatures as compared with the experimental data of Du *et al*. [35] for zeolite ITQ-1, and a good agreement was obtained. Savitz *et a*l. [26] measured adsorption data for methane, ethane, and propane in ZSM-12 zeolite. Our simulations are in excellent agreement with their experimental values (Table 2.3 and Figure 2.5a). In addition to small alkanes, *n*-hexane was also considered, and the simulation results at 315 K are shown in Figure 2.5b, in which the experimental data of Guil *et a*l. [36] are also given for comparison. Again, the agreement is good. It is shown that the force field can be successfully extended from MFI-type to MWW- and MTW-type zeolites.

Recently, Gribov *et al.* [37] carried out a systematic theoretical and experimental study on the adsorption of *n*-hexane on a series of pure silica zeolites. The heat of adsorption of *n*-hexane on different zeolites was investigated in detail, and for ZSM-12, CIT-5, ITQ-29, and SSZ-35 zeolites the adsorption isotherms were also measured at various temperatures. A detailed comparison with their results was carried out in this work. Table 2.4 shows the computed heat of adsorption, as compared to their experimental and calculation results. Our values are in agreement with their results. The comparisons between our computed isotherms with their results are given in Figure 2.6. Since the unit of loading is Absorbance (a. u.) in the experimental work, a conversion factor is needed to translate their IR data into quantitative values. We have fitted our data to the experimental values to obtain this conversion factor.

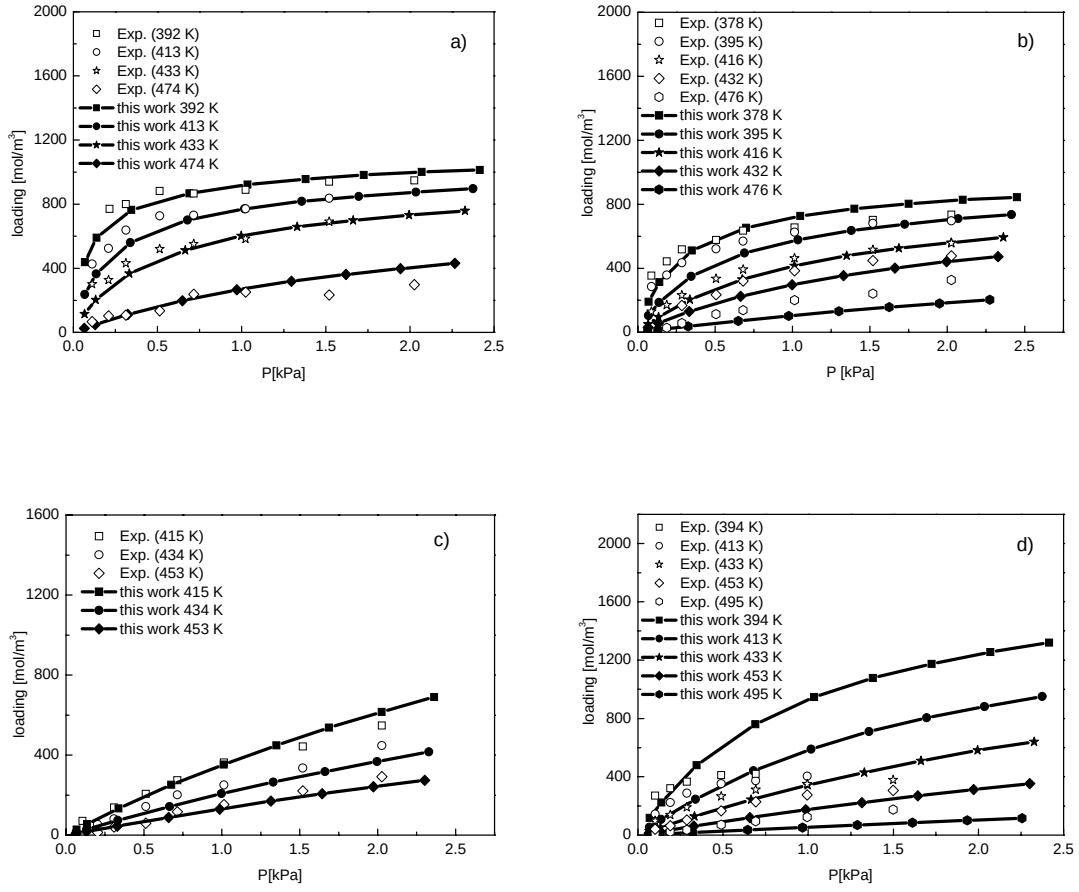

Figure 2.6: Comparison of the experimental [37] and simulated adsorption isotherms of *n*-hexane in four silica zeolites: a) ZSM-12, b) CIT-5, c) ITQ-29, and d) SSZ-35.

Figure 2.6 shows that the experimental isotherms could be accurately predicted except for STF-type zeolites. The discrepancy between simulations and experiments for STF-type zeolites may be attributed to the reasons that perfect structures are used in the simulations, while the experimental samples may be not completely accessible due to intergrowths and partial block of the pores.

2.4 Conclusions

The simulation results presented in this work show that the UA force field of Dubbeldam *et al.* developed for MFI-type zeolites is applicable to other pure silica zeolites, such as FER-, MWW-, MTW-, CFI-, and LTA-type zeolites. It may be concluded that this UA force field is a general force field applicable to most pure silica zeolites that may find wide applications in the field of petrochemical industry.

Bibliography

[1] Catlow, C. R. A.; van Santen, R. A.; Smit, B. *Computer Modelling of Microporous Materials*; Elsevier Science: Amsterdam, 2004.

[2] Krishna, R.; Smit, B.; Calero, S. *Chem. Soc. Rev.* **2002**, *31*, 185.

[3] June, R. L.; Bell, A. T.; Theodorou, D. N. *J. Phys. Chem.* **1992**, *96*, 1051.

[4] Smit, B.; Loyens, L. D. J. C.; Verbist, G. L. M. M. *Faraday Discuss.* **1997**, *106*, 93.

[5] Maris, T.; Vlugt, T. J. H.; Smit, B. *J. Phys. Chem. B* **1998**, *102*, 7183.

[6] Vlugt, T. J. H.; Krishna, R.; Smit, B. *J. Phys. Chem. B* **1999**, *103*, 1102.

[7] Pascual, P.; Ungerer, P.; Tavitian, B.; Pernot, P.; Boutin,A. *Phys. Chem. Chem. Phys.* **2003**, *5***,** 3684.

[8] Dubbeldam, D.; Calero, S.; Vlugt, T. J. H.; Krishna, R.; Maesen, T. L. M.; Beerdsen, E.; Smit, B. *Phys. Rev. Lett.* **2004**, *93*, 088302.

[9] Dubbeldam, D.; Calero, S.; Vlugt, T. J. H.; Krishna, R.; Maesen, T. L. M.; Smit, B. *J. Phys. Chem. B* **2004**, *108*, 12301.

[10] van Well, W. J. M.; Cottin, X.; de Haan, J. W.; van Santen, R. A.; Smit, B. *Angew. Chem., Int. Ed.* **1998**, *37*, 1081.

[11] van Well, W. J. M.; Cottin, X.; de Haan, J. W.; Smit, B.; Nivarthy, G.; Lercher, J. A.; van Hooff, J. H. C.; van Santen, R. A. *J. Phys. Chem. B* **1998**, *102*, 3945.

[12] van Well, W. J. M.; Cottin, X.; Smit, B.; van Hooff, J. H. C.; van Santen, R. A. *J. Phys. Chem. B* **1998**, *102*, 3952.

[13] Pascual, P.; Boutin, A. *Phys. Chem. Chem. Phys.* **2004**, *6***,** 2015.

[14] Pascual, P.; Boutin, A.; Ungerer, P.; Tavitian, B.; Fuchs, A. H. *Mol. Simulation* **2004**, *30*, 593.

[15] Vaughan, P. A. *Acta. Crystallogr.* **1966**, *21*, 983.

[16] Fyfe, C.A.; Gies, H.; Kokotailo, G. T.; Marler, B.; Cox, D. E. *J. Phys. Chem.* **1990**, *94*, 3718.

[17] Camblor, M. A.; Corma, A.; Díaz-Cabañas, M.-J.; Baerlocher, Ch. *J. Phys. Chem. B* **1998**, *102*, 44.

[18] Wagner, P.; Yoshikawa, M.; Lovallo, M.; Tsuji, K.; Taspastis, M.; Davis, M. E. *Chem. Commun.***1997**, 2179.

[19] Corma, A.; Rey, F.; Rius, J.; Sabater, M. J.; Valencia, S. *Nature*, **2004**, *431*, 287.

[20] Wagner, P.; Zones, S. I.; Davis, M. E.; Medrud, R. C. *Angew. Chem., Int. Ed.* **1999**, *38*, 1269.

[21] Baerlocher, Ch.; Meier, W. M.; Olson, D. H. *Atlas of Zeolite Structure Types, 5th revised ed.*; Elsevier Science: Amsterdam, 2001.

[22] Vlugt, T. J. H.; Schenk, M. *J. Phys. Chem. B* **2002**, *106*, 12757.

[23] Ryckaert, J.P.; Bellemans, A. *Faraday Discuss. Chem. Soc*. **1978**, *66*, 95.

[24] Smit, B.; Siepmann, J. I. *J. Phys. Chem.* **1996**, *98*, 8442.

[25] Frenkel, D.; Smit, B. *Understanding Molecular Simulations: From Algorithms to Application*s, 2nd ed.; Academic Press: San Diego, CA, **2002**.

[26] Savitz, S.; Siperstein, F.; Gorte, R. J.; Myers, A. L. *J. Phys. Chem. B* **1998**, *102*, 6865.

[27] Eder, F.; Lercher, J. A. *J. Phys. Chem. B* **1997**, *101*, 1273.

[28] Ndjaka, J.-M. B.; Zwanenburg, G.; Smit, B.; Schenk, M. *Micropor. Mesopor. Mater.* **2004**, *68*, 37.

[29] Eder, F.; Lercher, J. A. *Zeolites* **1997**, *18*, 75.

[30] Calero, S.; Lobato, M. D.; García-Pérez, E.; Mejías, J. A.; Lago, S.; Vlugt, T. J. H.; Maesen, T. L. M.; Smit, B.; Dubbeldam, D. *J. Phys. Chem. B* **2006**, *110*, 5838.

[31] Karsli, H.; Çulfaz, A.; Yücel, H. *Chem. Eng. Comm.* **2003**, *190*, 693.

[32] Long, Y. C.; Ma, M. H.; Sun, Y. J.; Jiang, H. W. *J. Incl. Phenom. Macro.* **2000**, *37*, 103.

[33] Ma, M. H.; Jiang, H. W.; Long, Y. C.; Sun, Y. J. *Acta. Chimica Sinica* **1998**, *56*, 405.

[34] García-Pérez, E.; Dubbeldam, D.; Liu, B.; Smit, B.; Calero, S. *Angew. Chem., Int. Ed.* **2007**, *46*, 276.

[35] Du, H. W.; Kalyanaraman, M.; Camblor, M. A.; Olson, D. H. *Micropor. Mesopor. Mater.* **2000**, *40*, 305.

[36] Guil, J. M.;Guil-López, R.; Perdigón-Melón, J. A.; Corma, A. *Micropor. Mesopor. Mater*.**1998**, *22***,** 269.

[37] Gribov, E. N.; Sastre, G.; Corma, A. *J. Phys. Chem. B* **2005**, *109*, 23794.

A new united atom force field was developed which accurately describes the adsorption properties of linear alkenes in zeolites. The force field was specifically designed for use in the inhomogeneous system and therefore a truncated and shifted potential was used. With the determined force field, we performed a comparative study on the adsorption behaviors of ethene and propene in four pure-silica small pore eight-membered ring zeolites, CHA, DDR, ITE, and IHW (named as Chabazite, DD3R, ITQ-3, and ITQ-32, respectively), characterized for their paraffin/olefin separation capability. The different macroscopic adsorption behaviors of alkenes in the four zeolites were elucidated and related to their structures with the microscopic information obtained from the molecular simulations providing useful information for further rational design of such zeolites with tailored properties.

B. Liu, B. Smit, F. Rey, S. Valencia, and S. Calero*

A New United Atom Force Field for Adsorption of Alkenes in Zeolites

3.1 Introduction

In recent years there has been considerable interest in separation technology concerning olefin/paraffin mixtures. Many microporous materials such as zeolites are recognized as promising candidates for this purpose based on their adsorption and diffusion properties [1-12]. Therefore, it is important to explore the adsorption and diffusion behaviors of hydrocarbons in different zeolites. In addition to experiment, molecular simulation has proved to be a useful tool to investigate the properties of fluids confined in porous materials [13]. Although there are numerous simulation studies on the adsorption and diffusion of alkanes in zeolites, theoretical studies concerning the alkenes in zeolites are scarce [2, 14-18], mainly due to the absence of suitable force fields.

Many united-atom (UA) force fields [19-23] have been proposed recently. These force fields can accurately and quantitatively describe the adsorption and diffusion properties of alkanes in nanoporous framework structures. However, to the best of our knowledge, there are only two UA force fields dealing with the adsorption of alkenes in zeolites [14, 18]. The first one was developed by Jakobtorweihen *et al.* [14] This force field accurately describes the adsorption properties of alkenes in the Silicalite (MFI) zeolite as well as in the Theta-1 (TON) and DD3R (DDR) zeolites. This force field, however, uses tail corrections which make it less practical to use in inhomogeneous systems [24, 25]. The other one is the extended version of this force field to include the effects of sodium cations by Granato *et al.* [18] As most of the

* Liu, B.; Smit, B.; Rey, F.; Valencia, S.; Calero, S. *J. Phys. Chem. C* **2008**, *112*, 2492.

accurate alkane models do not use these tail corrections for doing proper adsorption and diffusion in this type of systems, it is important to have a similar type of model for both alkanes and alkenes.

Pure silica small-pore eight-membered ring (8R) zeolites have been recognized as promising candidates for olefin/paraffin separation [1-4]. Although various pure silica 8R zeolites have been experimentally characterized for their alkene adsorption and olefin/paraffin separation capability [1-4, 8, 15, 26], theoretical studies concerning the diffusion and adsorption of alkenes in these kinds of zeolites are very scarce [2, 15, 16]. The only available work is that of ter Horst *et al.* [16], who studied the diffusion of propene in the pure-silica zeolite DD3R with the commercial program package Cerius^2, and that the very crude simulations on the adsorption of alkenes in the zeolites DD3R and ITQ-12 with Cerius^2 as a support for the experimental measurements [2, 15]. At present there are much more accurate force fields available compared to the ones in Cerius^2. Considering that there are eleven 8R zeolites that can be prepared as pure silica and their potential application for olefin separation, it is worth performing a systematic comparative study for some of them, for which molecular simulation is the most suitable tool. Therefore, with the newly developed force field, this work performed a systematic molecular simulation study on the adsorption of ethene and propene in four pure-silica 8R zeolites with different pore topologies, Chabazite (CHA), DD3R (DDR), ITQ-3 (ITE), and ITQ-32 (IHW). The microscopic information obtained from the molecular simulations was used to elucidate the different macroscopic adsorption behavior of the four zeolites to provide useful information for further rational use of such zeolites.

3.2 Simulation technique

To test the accuracy of the alkene-alkene interactions, the vapor-liquid coexistence curves (VLCC) were computed using the *NVT* version of Gibbs ensemble [27, 28]. For the calculation of Henry coefficient and the isosteric heats of adsorption at infinite dilution Q_{st}^0, we performed configurational-bias Monte Carlo (CBMC) simulations in the *NVT* ensemble. During the simulation we computed the Rosenbluth factor and the internal energy ΔU, which are directly related to the Henry coefficient and Q_{st}^0, respectively [20, 29]. Adsorption isotherms were calculated in the grand-canonical ensemble using the CBMC method. A detailed description of the simulation methods can be found in Ref. 20.

3.3 Results and discussion

3.3.1 Development of the new UA force field

In the present work, the united-atom model was used, in which CH_3 (sp^3), CH_2 (sp^2), and CH (sp^2) groups are considered as a single pseudo-atom or united atom. The Lennard-Jones 12-6 potential was used which is truncated at a cutoff (r_{cut}) of 12 Å and shifted so that the energy tends smoothly to zero at the cutoff.

Alkene-alkene interaction

The TraPPE-UA force field for alkenes [30] was used in this work. The bond length between the atoms was kept fixed. Harmonic potential models the bond bending between three neighboring beads, and the torsion potential used in the TraPPE-UA force field [30] was adopted in this work to control the torsional angle. The effective Lennard-Jones (LJ) interaction parameters for the $CH_i(sp^3)$ groups were taken from the Ref. 19 and the ones between the $CH_2(sp^2)$-$CH_2(sp^2)$ and $CH(sp^2)$-$CH(sp^2)$ groups were optimized in this work to reproduce the vapor-liquid coexistence curves for ethene and propene. The experimental curves [31] and our simulation results based on the TraPPE-UA (using the truncated and shifted potential instead of the truncated potential with tail corrections) as well as on the new LJ parameters (all the parameters are listed in Table 3.1) are shown in Figures 3.1a-b. Obviously, the coexistence densities were well reproduced by our new parameters, much better than that from the original TraPPE-UA parameters.

σ_{ij} ε_{ij}	O	$CH_3(sp^3)$	$CH_2(sp^3)$	$CH_2(sp^2)$	$CH(sp^2)$
$CH_3(sp^3)$	3.48 93	3.76 108	3.86 77.77	3.72 100.22	3.75 75.66
$CH_2(sp^3)$	3.58 60.5	3.86 77.77	3.96 56	3.82 72.17	3.85 54.48
$CH_2(sp^2)$	***3.53*** ***82.05***	3.72 100.22	3.82 72.17	***3.685*** ***93***	3.71 70.21
$CH(sp^2)$	***3.502*** ***55.215***	3.75 75.66	3.85 54.48	3.71 70.21	***3.74*** ***53***
bond lengths	r_0 (Å)				
CH_i-CH_j	1.54				
CH_i=CH_j	1.33				
bend	$U^{bend}=1/2\ k_0\ (\theta-\theta_0)^2$				
	k_0/k_B = 70400K, θ_0=119.70^0				
torsion	$U_{torsion} = c_0 + c_1[1+\cos(\phi)] + c_2[1-\cos(2\phi)] + c_3[1+\cos(3\phi)]$				
c_n/k_B in K	c_0	c_1	c_2	c_3	
	688.5	86.36	-109.77	-282.24	

Table 3.1: Force field parameters used in this work. LJ parameters σ_{ij}[Å] is in the upper left corner and ε_{ij}/k_B [K] is in the lower right corner of each field. The $CH_i(sp^3)$- $CH_i(sp^3)$ and $CH_i(sp^3)$-oxygen interaction parameters were taken from Ref. 19 and the internal bond, bend, and torsion parameters were taken from Ref. 30. The parameters proposed in this work are given as bold italics.

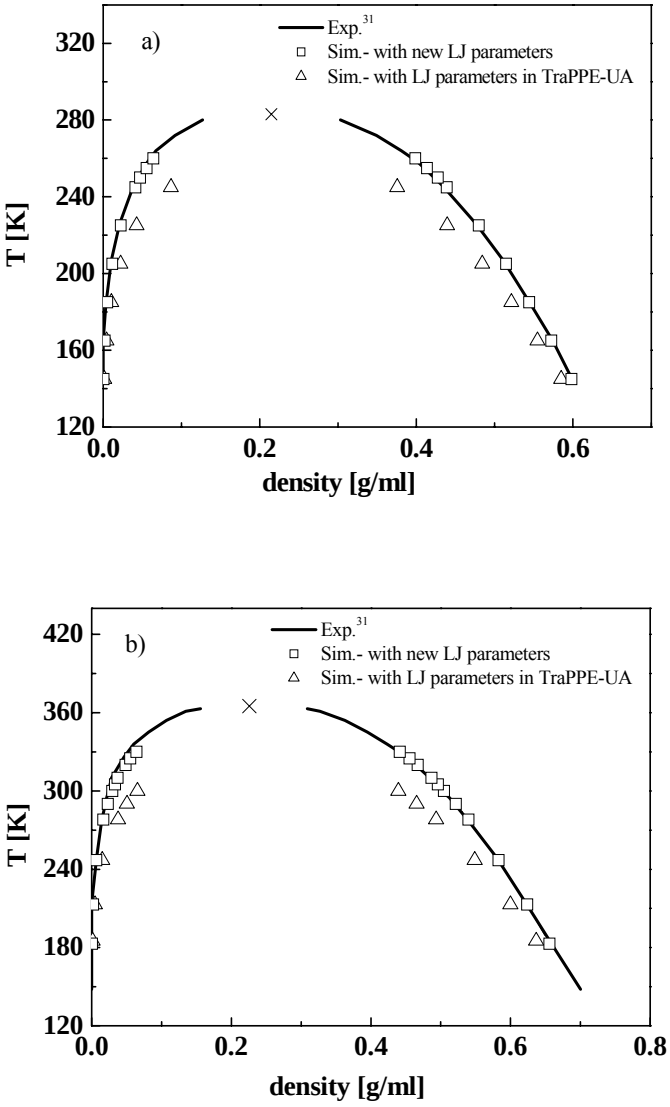

Figure 3.1: Vapor-liquid coexistence curves for a) ethene and b) propene.

Alkane-zeolite interaction

To keep the consistency of all interaction parameters used in this work, we adopted the united-atom force field proposed by Dubbeldam *et al*. [19] for describing the interactions between $CH_i(sp^3)$ centers and the oxygen atoms of the zeolite framework. This force field faithfully reproduces the experimentally determined isotherms (particularly the inflection points) in pure silica MFI-type zeolites and has been successfully extended to most types of pure silica zeolites [20, 32, 33].

Alkene-zeolite interaction

Following a similar strategy as employed in our previous work [19-23] for the development of the UA force field for alkane-zeolite systems, simulations were performed first for the adsorption isotherms of ethene, propene, and 1-butene to determine the effective LJ interaction

parameters for the $CH_2(sp^2)$, $CH(sp^2)$ and the oxygen atoms of the zeolite framework. Ideally, one would like to calibrate a force field using various data sets from different authors. Therefore the experimental values measured in MFI zeolites were adopted here as the calibration set. Our simulation results as well as the experimental [34-41] and previous simulation results [14, 17] are shown in Figures 3.2a-c. We found that our UA force field faithfully reproduces the experimental isotherms and shows comparable results with previous simulations. It should be pointed out that in Jakobtorweihen *et al.*'s work [14] the tail correction was used, while in Pascual *et al.*'s work [17] a more complex anisotropic united atom (AUA) potential scheme was used.

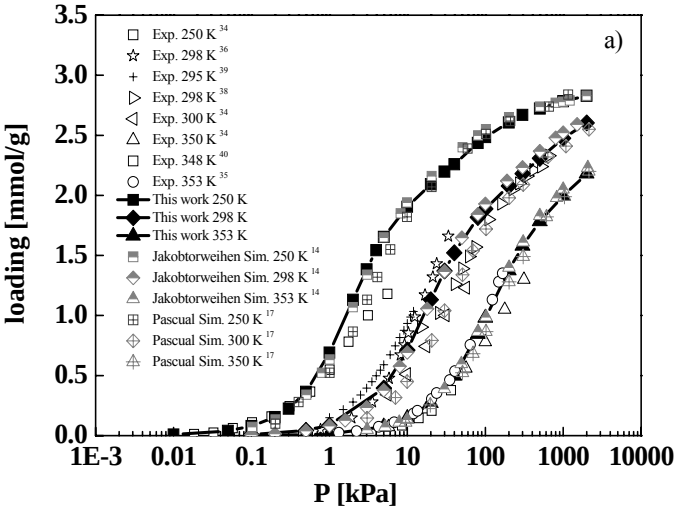

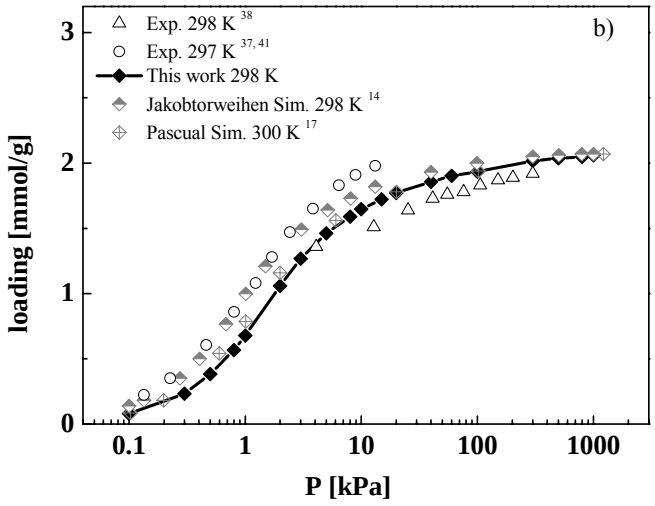

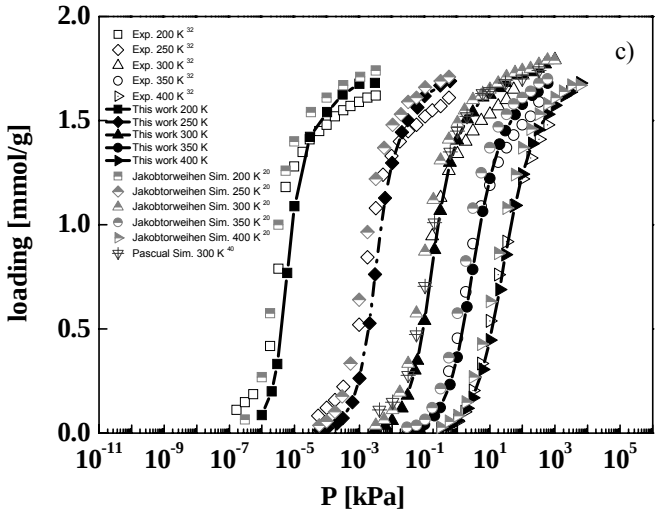

Figure 3.2: Comparison of the experimental and simulated adsorption isotherms of a) ethene, b) propene, and c) 1-butene in MFI zeolites.

Having obtained the parameters for $CH_2(sp^2)$-O and $CH(sp^2)$-O, we need to check their validity. Firstly, the isosteric heats of adsorption at infinite dilution Q_{st}^0 for ethene, propene, and 1-butene in MFI zeolite were calculated, as shown in Table 3.2. The calculated results based on our new force field show comparable results with Jakobtorweihen *et al.*'s simulations and are in the range of the experimental data, closing to the mean value between the lowest and the highest experimental values.

	ethene	**propene**	**1-butene**
experimental data [a]	24.0-32.7	40.0	46.0-51.5
this work	28.2	38.1	46.6
Jakobtorweihen *et al.* [14]	27.6	38.3	46.4

Table 3.2: Isosteric heats of adsorption at infinite dilution Q_{st}^0 [kJ/mol] of alkenes in MFI zeolite at 298 K. [a] The experimental data are taken from the Table 3 in Ref. 14.

To demonstrate that our parameters are transferable to other pure silica zeolites other than MFI, we also calculated the adsorption isotherms, together with the Henry coefficients and isosteric heat of adsorption at infinite dilution of ethene and propene in TON, DD3R, ITQ-29, CHA, ITQ-3, and ITQ-32 zeolites. A comparison with the experimental data is shown in table and figure and compared with experimental data available [2, 3, 42-45], as shown in Table 3.3 and Figures 3.3 and 3.4.

Zeolite	K_H (mol/kg/Pa)		Q_{st}^0 (kJ/mol)	
	Sim.	Exp. [2, 45]	Sim.	Exp.
DD3R	9.67×10^{-4}	7.54×10^{-4}	35.6	36.0 [2]
CHA	5.28×10^{-4}	-	33.0	33.5 [3]
ITQ-3	4.52×10^{-4}	-	31.6	28.5 [3]
ITQ-32	7.25×10^{-4}	11.61×10^{-4}	36.0	33.6 [45]
TON	4.24×10^{-4}	-	39.8	-

Table 3.3: Henry coefficients K_H and isosteric heats of adsorption at infinite dilution Q_{st}^0 of propene at 303 K.

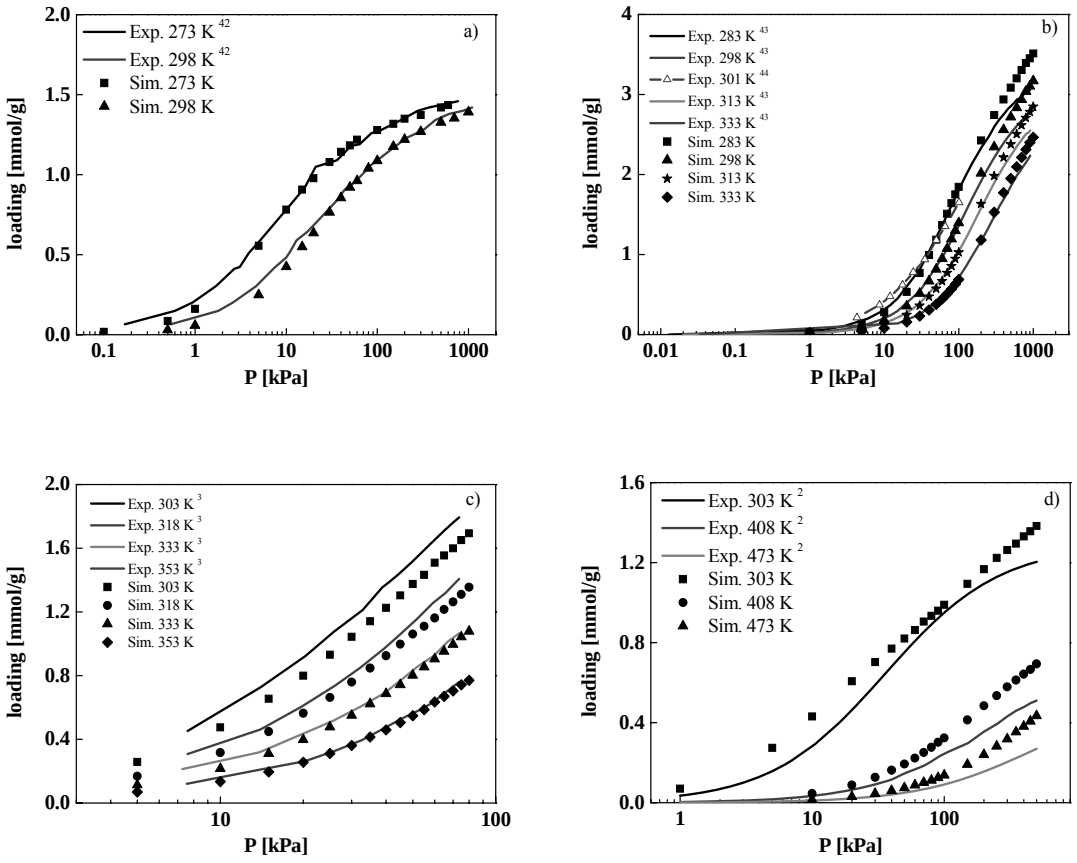

Figure 3.3: Comparison of the experimental and simulated adsorption isotherms of ethene in a) TON, b) ITQ-29, c) CHA, and d) DD3R zeolites.

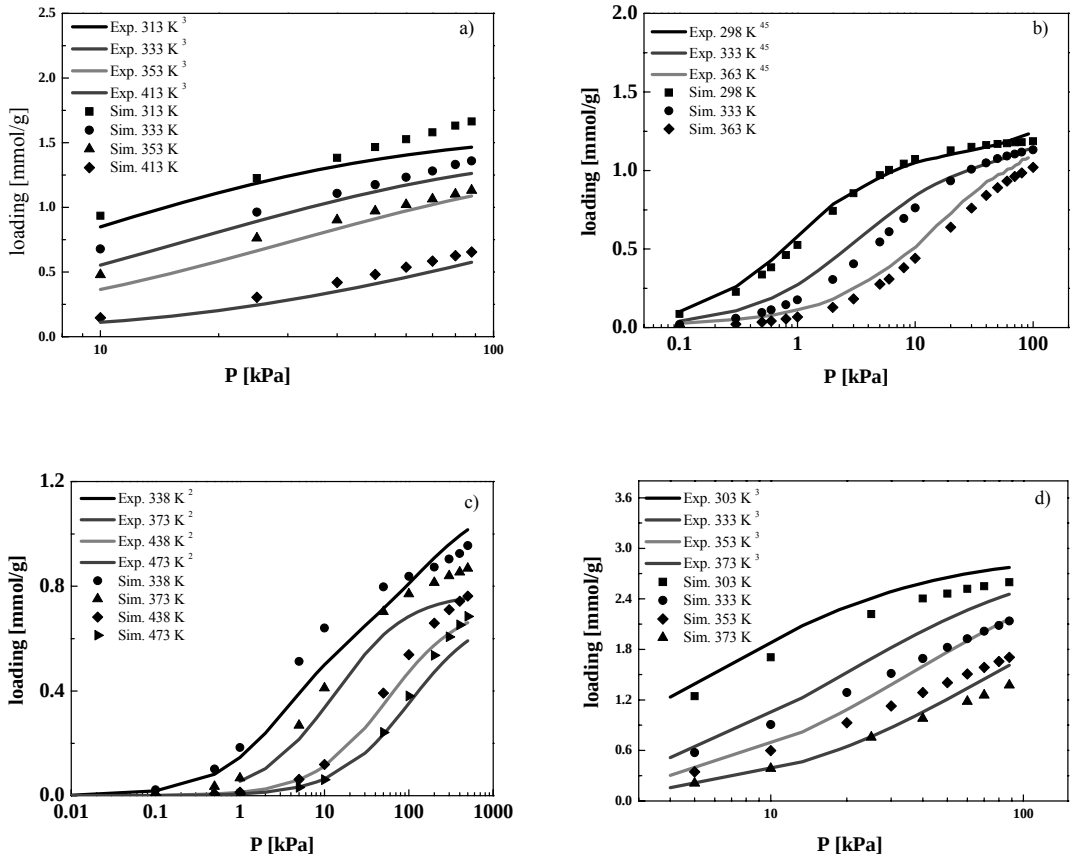

Figure 3.4: Comparison of the experimental and simulated adsorption isotherms of propene in a) ITQ-3, b) ITQ-32, c) DD3R, and d) CHA zeolites.

Figure 3.3 shows that for ethene the agreement between our simulations and the experiments is good for TON, ITQ-29 (our simulations agree well with the experimental data of Ref. 43 at 298 K, but less with that of Ref. 44 at 301 K, attributing to the existence of discrepancy between experimental data measured by different authors) and CHA, but less for DD3R. For the latter, our simulations show systematically higher values than the experimental observations and similar deviation has been observed by other simulations using a different force field [14]. The discrepancy between simulations and experiments may be attributed to the perfect structures are used in the simulations, while the experimental samples may be not completely accessible due to intergrowths and partial blocking of the pores. Also this discrepancy can be related to the large diffusional limitations due to the very large crystal size that generally is observed in pure silica zeolites, precluding reaching thermodynamic equilibrium in the experimental data.

For propene, as a first step the Henry coefficients and the isosteric heat of adsorption at infinite dilution Q_{st}^{0} were calculated, and compared with experimental values [2, 3, 45], as shown in Table 3.3. Again the discrepancy between simulations and experiments may be attributed to the reasons that simulations are always assuming perfect and infinite crystals as well as equilibrium. However, experimentally this is not the case and generally crystals are far

from being perfect. Of course, the amount of defects will depend on the thermal history, synthesis method, etc used to prepare the sample. These non-idealities have not been taken into account in our simulation studies. A second source (and at least equally important) is the accuracy of experimental methods and the corresponding adsorption models used during the data analysis for calculating the Henry coefficients and heats of adsorption. For instance, the experimental data on pure silica ITQ-32 sample were published in ref. 45 as supplementary information. In this work, these data were fitted using the Virial formalism to describe the isotherm and the Henry coefficients were calculated at each temperature (25, 60, and 90 ºC). The Heats of adsorption were calculated using the Clausius-Clapeyron equation. The experimental error for the heat of adsorption is larger than 3 kJ/mol and therefore, there is a good agreement between experimental and calculated results. On the other hand, since the uncertainty of the K_H values in this case is much higher than in Q_{st} values, the differences in order of magnitude are meaningful. Furthermore, Figure 3.4 shows that the computed adsorption isotherms of propene can predict the experimental isotherms of ITQ-3 and ITQ-32 zeolites accurately. For DD3R, a similar behavior as ethene was found, that is, simulated adsorption isotherms are higher than the experimental data. Again, this may be attributed to the fact that diffusional restrictions are limiting to fully reach equilibrium in the experimental measurements or to the presence of some low-porous amorphous silica which could accompany to the DD3R sample studied in ref. 2. CHA is another case, in which our simulations show systematically lower values than the experimental observations. The reason might be the sensitivity of the Lennard-Jones potential for small changes in the parameters when the oxygen and carbon groups are in close proximity [46]. This effect would be enlarged when the adsorbate is bigger.

The simulation results of the adsorption isotherms, together with those of the Henry coefficients and the isosteric heat of adsorption at infinite dilution, show that the UA force field proposed in this work is applicable to most pure silica zeolites and can be used for the characterization of alkenes adsorption in the zeolites.

3.3.2 Comparison of alkene adsorption in pure-silica CHA, DD3R, ITQ-3, and ITQ-32 zeolites

With the determined force field, we further performed a molecular simulation study on the adsorption of alkenes in four typical pure silica 8R zeolites with different pore topologies, CHA, DD3R, ITQ-3, and ITQ-32, since they have been recognized as promising candidates for the separation of alkene from olefin/paraffin mixtures in the petrochemical industry [1-4, 45].

3.3.2.1 Zeolite models

The structures of DD3R, CHA, and ITQ-3 are well known and have been used in many previous simulation studies [14, 16, 20, 48-51]. The DDR-type zeolite consists of 19-hedron cavities connected through 8R windows across into a hexagonally arranged two-dimensional

cage/window-type system. The CHA-type zeolite consists of ellipsoidal cavity through 0.38 nm wide 8R windows. ITQ-3 has a one-dimensional pore system with small windows of about 0.4 nm in diameter made up of 8R that open to larger cavities. A second straight channel runs through the material but is too narrow to accommodate guest molecules. ITQ-32 has been synthesized recently [26] and has never been the focus of a simulation. It exhibits a unidirectional small 8R channel system along the x-axis, with a pore aperture of 3.5×4.3 Å, which is crossed perpendicularly by relatively short 12R channels. The 12R channels interconnect two neighbored 8R channels along the z direction, resulting in a bidirectional pore structure. The structures of the four zeolites are shown in Figure 3.5, and some details of the structures of the four zeolites are summarized in Table 3.4. In the simulations, the zeolite structures were constructed by using the atomic coordinates reported [26, 47, 52, 53], and the zeolite lattices were assumed to be rigid in the simulations since the flexibility of the framework has a negligible influence on the adsorption properties [54].

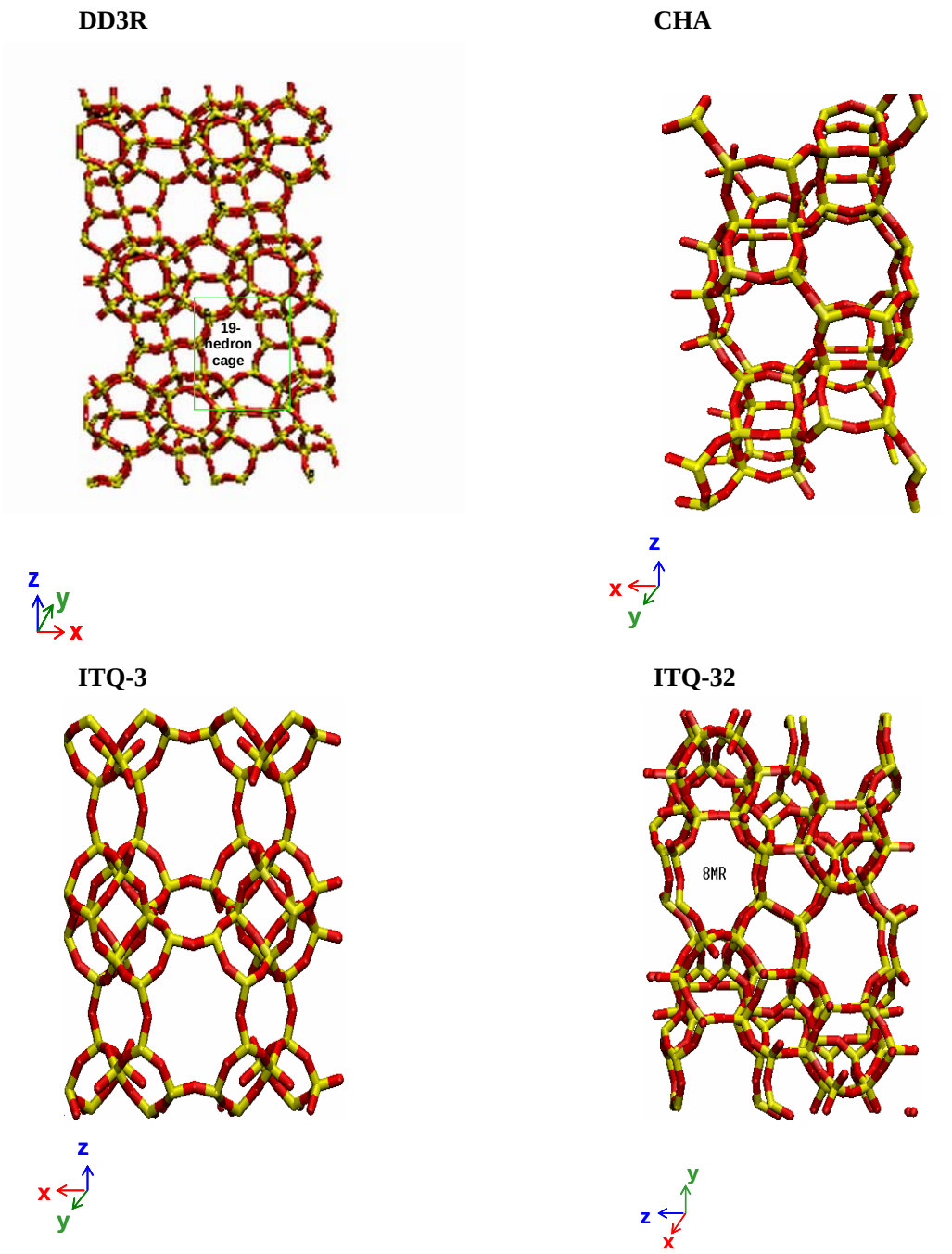

Figure 3.5: The structures of DD3R, CHA, ITQ-3, and ITQ-32.

Zeolite	Topology	Unit Cell	Simulation cell size (Å)			Ring size (Å)
			x	y	z	
DD3R [52]	2-d	a=13.860, c=40.89 Å Trigonal (R-3m)	41.58	41.58	40.89	3.7×4.4
CHA [47]	3-d	a=13.529, c=14.748 Å Trigonal (R-3m)	27.058	27.058	29.496	3.8×3.8
ITQ-3 [53]	1-d	a=20.622,b=9.724,c=19.623 Å Orthorhombic (Cmcm)	41.244	38.896	39.246	3.8×4.3
ITQ-32 [26]	2-d	a=13.699,b=24.067,c=18.197 Å Orthorhombic (Cmca)	27.398	48.134	36.394	3.5×4.3

Table 3.4: Structural information for the four pure silica 8R zeolites used in this work.

3.3.2.2 Comparison of alkene adsorption behaviors

In Figure 3.6 we compare the adsorption behavior of alkenes in the four typical 8R zeolites, DD3R, CHA, ITQ-3, and ITQ-32.

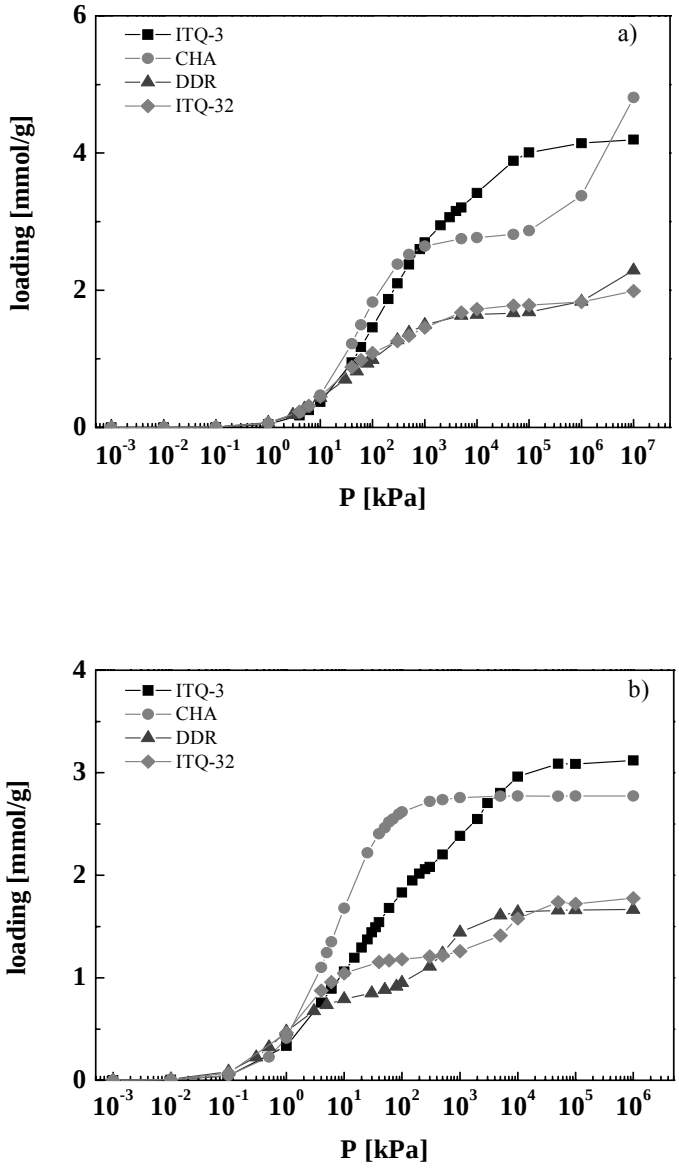

Figure 3.6: Simulated adsorption isotherms of a) ethene and b) propene in DD3R, CHA, ITQ-3, and ITQ-32 zeolites at 303 K.

For ethene at low pressures, the order of the adsorption capacity is: DD3R>ITQ-32 >CHA>ITQ-3; at high pressures, the order changed to: CHA>ITQ-3> DD3R≈ITQ-32. This agrees with the order of the experimentally measured void volumes of the four zeolites determined by N_2 adsorption measurements: CHA: 0.3 cm^3/g [47], ITQ-3: 0.23 cm^3/g [47], ITQ-32: 0.16 cm^3/g [26], DD3R: 0.15 cm^3/g [2]. The order of the propene adsorption capacity is same as the one for ethene at low pressures, agreeing well with the order of the experimental Q_{st}^0 presented in Table 3.3; while at high pressures, the order changed to: ITQ-3> CHA> ITQ-32≈DD3R. The adsorption capacity of a zeolite is affected by various factors, and the main ones are surface area, the interactions between adsorbate and adsorbent, packing of adsorbate molecules inside the void spaces of the adsorbent, and the available void volumes.

At very low pressures (close to infinite dilution), the interactions between adsorbate and adsorbent are predominant factor, while at sufficient high pressures it is determined by the effective void volume. The adsorption behavior is the result of the cooperative effects of the various factors. This explains the changes of the adsorption capacities with pressures of the four zeolites shown in Figures 3.6a-b.

In addition to the differences in adsorption capacities, the shapes of the adsorption isotherms are also different for the four zeolites. The inflection behavior was found on the adsorption isotherm for DD3R at a loading of 12 molecules per unit cell for ethene and 6 for propene. This corresponds to 2 molecules per accessible cage for ethene and 1 for propene since one unit cell of DD3R has six 19-hedron cages [2]. In view of the free volume, the 19-hedron cavity is large enough for 2 ethene molecules, but also allows the adsorption of exactly two propene molecules, which is possible only in a certain arrangement. If all the cages are filled with one molecule, insertion of an additional molecule requires some energy for the rearrangement. Consequently, a second inflection behavior occurs evidently at higher pressures, for a loading of 2 propene molecules per accessible cage. In the case of ITQ-32, similar adsorption behavior as DDR is observed, that is, the inflection behavior occurs at a loading of 12 molecules per unit cell for ethene and 6 for propene. The underlying mechanism is the same as that for DD3R. As to CHA, the inflection behavior was found at a loading of 6 molecules per unit cell for ethene and no inflection occurred for propene. A unit cell of CHA contains a single cage with 6 eight-membered 0.38nm wide ring windows. The guest molecules have to pass through the windows to enter the cage. The cage can host optimally 6 ethene molecules, more energy is needed for insertion of additional molecules. The CHA cage can hold exactly 6 propene molecules. ITQ-3, on the other hand, has four cavities per unit cell. The adsorption isotherms do not show any obvious inflection and the maximum capacity for ethene is 4 molecules/cavity and 3 molecules/cavity for propene.

3.4 Conclusions

The UA force field developed in this work can accurately describe the adsorption properties of linear alkenes in several pure silica zeolites, such as MFI, TON, ITQ-29, ITQ-3, ITQ-32, CHA, and DD3R. The results show that it is a general force field applicable to most pure silica zeolites.

Based on this new force field, the different macroscopic alkene adsorption behavior of the four 8R zeolites, CHA, DD3R, ITQ-3, and ITQ-32, were elucidated with the microscopic information obtained from the molecular simulations, and a systematic comparison was made by relating their adsorption behavior to their structures.

Finally, it should be pointed out that, compared with the available UA force field of Jakobtorweihen *et al.*, the new force field does not include tail corrections, and thus can be used in a molecular dynamics simulation to, for example, simulate the diffusion of alkenes in zeolites.

Bibliography

[1] Zhu, W.; Kapteijn, F.; Moulijn, J. A. *Chem. Commun.* **1999**, 2453.

[2] Zhu, W.; Kapteijn, F.; Moulijn, J. A.; den Exter, M. C.; Jansen, J. C. *Langmuir* **2000**, *16*, 3322.

[3] Olson, D. H.; Camblor, M. A.; Villaescusa, L. A.; Kuehl, G. H. *Micropor. Mesopor. Mater.* **2004**, *67*, 27.

[4] Olson, D. H. U. S. Patent No. 6, 488, 741, 2002.

[5] Kantner, E.; Savage, D. W.; Bellows, R. J. U. S. Patent No. 5, 292, 990, 1994.

[6] Kulprathipanja, S. U. S. Patent No. 4, 433, 195, 1984.

[7] Daems, I.; Leflaive, P.; Methivier, A.; Denayer, J. F. M.; Baron, G. V. *Micropor. Mesopor. Mater.* **2005**, *82*, 191.

[8] Olson, D. H.; Yang, X.; Camblor, M. A. *J. Phys. Chem. B* **2004**, *108*, 11044.

[9] Grande, C. A.; Gigola, C.; Rodrigues, A. E. *Adsorption* **2003**, *9*,321.

[10] Da Silva, F. A.; Rodrigues, A. E. *Ind. Eng. Chem. Res.* **1999**, *38*, 2434.

[11] Jarvelin, H.; Fair, J. R. *Ind. Eng. Chem. Res.* **1993**, *32*, 2201.

[12] Rege, S. U.; Padin, J.; Yang, R. T. *AIChE J*. **1998**, *44*, 799.

[13] Catlow, C. R. A.; van Santen, R. A.; Smit, B. *Computer Modelling of Microporous Materials*; Elsevier Science: Amsterdam, 2004.

[14] Jakobtorweihen, S.; Hansen, N.; Keil, F. J. *Mol. Phys.* **2005**, *103*, 471.

[15] Yang, X.; Toby, B. H.; Camblor, M. A.; Lee, Y.; Olson, D. H. *J. Phys. Chem. B* **2005**, *109*, 7894.

[16] ter Horst, J. H.; Bromley, S. T.; van Rosmalen, G. M.; Jansen, J. C. *Micropor. Mesopor. Mater.* **2002**, *53*, 45.

[17] Pascual, P.; Ungerer, P.; Tavitian, B.; Boutin, A. *J. Phys. Chem. B* **2004**, *108*, 393.

[18] Granato, M. A.; Vlugt, T. J. H.; Rodrigues, A. E. *Ind. Eng. Chem. Res.* **2007**, *46*, 321.

[19] Dubbeldam, D.; Calero, S.; Vlugt, T. J. H.; Krishna, R.; Maesen, T. L. M.; Beerdsen, E.; Smit, B. *Phys. Rev. Lett.* **2004**, *93*, 088302.

[20] Dubbeldam, D.; Calero, S.; Vlugt, T. J. H.; Krishna, R.; Maesen, T. L. M.; Smit, B. *J. Phys. Chem. B* **2004**, *108*, 12301.

[21] Calero, S.; Dubbeldam, D.; Krishna, R.; Smit, B.; Vlugt, T. J. H.; Denayer, J. F. M.; Martens, J.A.; Maesen, T. L. M. *J. Am. Chem. Soc.* **2004**, *126*, 11377.

[22] Calero, S.; Lobato, M. D.; García-Pérez, E.; Mejías, J. A.; Lago, S.; Vlugt, T. J. H.; Maesen, T. L. M.; Smit, B.; Dubbeldam, D. *J. Phys. Chem. B* **2006**, *110*, 5838.

[23] García-Pérez, E.; Dubbeldam, D.; Maesen, T. L. M.; Calero, S. *J. Phys. Chem. B*, **2006**, *110*, 23968.

[24] Martin, M. G.; Thompson, A. P.; Nenoff, T. M. *J. Chem. Phys.* **2001**, *114*, 7174.

[25] Wilding, N. B.; Schoen, M. *Phys. Rev. E* **1999**, *60*, 1081.

[26] Cantín, A.; Corma, A.; Leiva, S.; Rey, F.; Rius, J.; Valencia, S. *J. Am. Chem. Soc.* **2005**, *127*, 11560.

[27] Panagiotopoulos, A. Z. *Mol. Phys.* **1987**, *61*, 813.

[28] Panagiotopoulos, A. Z.; Quirke, N.; Stapleton, M.; Tildesley, D. J. *Mol. Phys.* **1988**, *63*, 527.

[29] Frenkel, D.; Smit, B. *Understanding Molecular Simulations: From Algorithms to Applications*, 2nd ed.; Academic Press: San Diego, CA, 2002.

[30] Wick, C. D.; Martin, M. G.; Siepmann, J. I. *J. Phys. Chem. B* **2000**, *104*, 8008.

[31] Smith B. D.; Srivastava, R.; *Thermodynamic Data for Pure Compounds: Part A, Hydrocarbons and Ketones*; Elsevier: Amsterdam, 1986.

[32] Liu, B.; Smit, B.; Calero, S. *J. Phys. Chem. B* **2006**, *110*, 20166.

[33] Chong, S.S.; Jobic, H.; Plazanet, M. *Chem. Phys. Lett.* **2005**, *408*, 157.

[34] Stach, H.; Lohse, U.; Thamm, H.; Schirmer, W. *Zeolites* **1986**, *6*, 74.

[35] Choudhary, V. R.; Mayadevi, S. *Zeolites* **1996**, *17*, 501.

[36] Hampson, J. A.; Rees, L. V. C. *Fundamentals of Adsorption*, Suzuki, M. Ed.; pp. 259-266. *Studies in Surface Science and Catalysis*; Kodansha/Elsevier: Tokoy/Amserdam, 1993.

[37] Jen, H. W.; Otto, K. *Catal. Lett.* **1994**, *26*, 217.

[38] Hampson, J. A.; Jasra, R. V.; Rees, L. V. C. *Characterization of porous Solids II*, Rodriguez-Reinoso, F.; Rouquerol, J.; Sing, K. S. W.; Unger, K. K. Eds.; pp. 509-517. *Studies in Surface Science and Catalysis*; Elsevier: Amserdam, 1991.

[39] Bakker, W. J. W.; Kapteijn, F.; Poppe, J.; Moulijn, J. A. *J. Membrane Sci.* **1996**, *117*, 57.

[40] Gladden, L. F.; Hargreaves, M.; Alexander, P. *Chem. Eng. J.* **1999**, *74*, 57.

[41] Otto, K.; Montreuil, C. N.; Todor, O.; McCabe, R. W.; Gandhi, H. S. *Ind. Eng. Chem. Res.* **1991**, *30*, 2333.

[42] Hampson, J. A.; Rees, L. V. C. *Zeolites and Microporous Crystals,* Hattori, T.; Yashima, T. Eds.; pp. 197-208. *Studies in Surface Science and Catalysis*; Kodansha/Elsevier: Tokoy/Amserdam, 1994.

[43] Rey, F. private communication.

[44] Hedin, N.; DeMartin, G. J.; Strohmaier, K. G.; Reyes, S. C. *Micropor. Mesopor. Mater.* **2007**, *98*, 182.

[45] Palomino, M.; Cantín, A.; Corma, A.; Leiva, S.; Rey, F.; Valencia, S. *Chem. Commun.,* **2007**, 1233.

[46] Ndjaka, J.-M. B.; Zwanenburg, G.; Smit, B.; Schenk, M. *Micropor. Mesopor. Mater.* **2004**, *68*, 37.

[47] Díaz-Cabañas, M.-J.; Barrett, P. A.; Camblor, M. A. *Chem. Commun*. **1998**, 1881.

[48] Dubbeldam, D.; Smit, B. *J. Phys. Chem. B* **2003**, *107*, 12138.

[49] Dubbeldam, D.; Beerdsen, E.; Calero, S.; Smit, B. *Proc. Natl. Acad. Sci. U.S.A.* **2005**, *102*, 12317.

[50] Goj, A.; Sholl, D. S.; Akten, E. D.; Kohen, D. *J. Phys. Chem. B* **2002**, *106*, 8367.

[51] Skoulidas, A. I.; Sholl, D. S. *J. Phys. Chem. A* **2003**, *107*, 10132.

[52] Gies, H. Z. *Kristallogr.* **1986**, *175*, 93.

[53] Camblor, M. A.; Corma, A.; Lightfoot, P.; Villaescusa, L. A.; Wright, P. A. *Angew. Chem., Int. Ed.* **1997**, *36*, 2659.

[54] Vlugt, T. J. H.; Schenk, M. *J. Phys. Chem. B* **2002**, *106*, 12757.

The applicability of a recently proposed force field of Calero *et al.* (*J. Am. Chem. Soc.*, 2004, **126**, 11377) to Na-MOR zeolites is evaluated. The Henry coefficients of ethane and C_5-C_9 as well as the adsorption isotherms of ethane, propane, butane, and hexane in various Na-MOR zeolites are computed and compared with experimental values. These comparisons show that the new force field is suitable for Na-MOR zeolites. Furthermore, this force field is used to study the effects of sodium cations on the adsorption behavior of larger alkanes, such as C_4-C_7, in MOR-type zeolites. These simulations give a better understanding of the underlying mechanisms of the influences of the position and density of cations on adsorption. In addition, a characteristic pressure named "reversal pressure" is introduced which characterizes the efficiency of the presence of cations in zeolites.

B. Liu and B. Smit*

Molecular Simulation of Adsorption of Alkanes in Sodium MOR-type Zeolites using a New Force Field

4.1 Introduction

Zeolites are microporous materials that have been found widespread applications in many fields, particularly in heterogeneously catalyzed processes in the petrochemical industry. Mordenite (MOR), among the various zeolites, is a particularly useful zeolite for several catalytic applications, such as dewaxing of heavy petroleum fractions and cracking or isomerization of hydrocarbons [1]. Zeolites can be synthesized with a large range of different Si/Al ratios, where the anionic character of the lattice caused by the substitution of silicon by aluminum is compensated by cations. The presence of cations influences the adsorption and the catalytic properties of zeolites. The type, density, and location of non-framework cations can be tailored by adjusting the Si/Al ratio and also depends on the type of synthesis, leading to tailored adsorption and catalytic properties.

The sodium form of MOR-type zeolites (Na-MOR) is commonly used in practical applications. Although many experimental investigations have been performed on the

* Liu, B.; Smit, B. *Phys. Chem. Chem. Phys.* **2006**, *8*, 1852.

adsorption properties of Na-MOR zeolites [2-12], our understanding of the effects of cations on the adsorption properties at the molecular level is as yet incomplete. Molecular simulations might be a suitable tool to complement experimental efforts. However, so far a limited number of simulations have been performed on the adsorption properties of alkanes in Na-MOR zeolites, mainly due to the absence of suitable force fields. Most of these simulations describe the interactions of relatively small alkanes. For example, Smit and den Ouden [13] performed a Metropolis Monte Carlo (MC) study of small molecules in Na-MOR, Macedonia *et al.* [9] studied the adsorption isotherms of methane, ethane, and argon in Na-MOR zeolite by grand-canonical Monte Carlo (GCMC) simulations. Beerdsen *et al.* [14], on the other hand, used the configurational-bias Monte Carlo (CBMC) method to investigate the influence of non-framework sodium cations on the adsorption of C_1-C_4 in MOR-type zeolites. It is well known that large alkanes are important in petrochemical processes; however, so far simulations on alkanes larger than C_4 have been performed only on a purely siliceous representation of MOR [15, 16], hence, without considering the influences of cations on adsorption.

It is commonly recognized that reliable force fields for the interatomic potentials play a key role in molecular simulations. As a result, many force fields [17-22] have been proposed for the interactions between the adsorbates and the zeolite framework and for the adsorbate-adsorbate interactions. Recently, Calero *et al.* [23] developed a united-atom force field, able to accurately describe the adsorption properties of linear alkanes in the sodium form of FAU-type zeolites. In this force field the nature, density, and mobility of the non-framework cations are carefully taken into account, and good agreement was obtained between experiments and simulations. This force field gives a very good description of the interactions between alkanes, sodium cations in FAU-type zeolites. Because this force field is based on a set of superimposed empirical potentials of which the parameters have been fitted to experimental data directly without using mixing rules, the values of these parameters may be different with one would expect. For example, the positively charged Na ion has a strength parameter, ε/k, which may look surprisingly high for a "non-polarizable" molecule and the Na-CH_3 interaction has a relatively high dispersion interaction. If such values would be completely unphysical, it would be very unlikely that transferring these potentials to other systems would give equally satisfactory results. Therefore, it is necessary to test the applicability of this force field to other zeolite structures. Recently, García-Pérez et al. [24] have successfully reproduced the adsorption properties of alkanes in sodium-exchanged MFI structure using this force field, encouraging us to test its applicability to the Na-MOR zeolites.

The aim of this work is threefold. The first aim is to validate a suitable force field for Na-MOR zeolites, for which we evaluate the recently proposed force field by Calero *et al.* against experimental data and also existing simulations using other force fields whenever

possible. The second aim is to use the validated force field to study the relationship between sodium cations and the adsorption behavior of butane in MOR-type zeolites. Finally, the adsorption behavior of larger alkanes such as C_5-C_7 is investigated, based on the force field of Calero *et al.* to give insight into molecular-level details of the influences of the location and density of cations on the adsorption.

4.2 Simulation models and methods

4.2.1 Mordenite zeolite models

To compare with experimental data directly, four Na-MOR unit cell compositions were used in the simulations, with varying Si/Al ratio: $Na_8Al_8Si_{40}O_{96}$ (the maximum amount of Al in the structure), $Na_6Al_6Si_{42}O_{96}$, $Na_2Al_2Si_{46}O_{96}$, and $Na_0Al_0Si_{48}O_{96}$. The structure corresponding to Na_8 was taken directly from the work of Meier *et al.* [25]. Zeolite structures with lower framework-aluminum densities were obtained by randomly removing Al atoms and replacing them by Si atoms, following the criteria of previous works [26, 27]. Through this procedure, the Löwenstein rule is automatically observed and it affords a reasonable approximation of the framework aluminum distributions obtained by experimental methods. The zeolite lattices were assumed to be rigid in the simulations, because the flexibility of the framework has a negligible influence on the adsorption of alkanes [28].

4.2.2 Force field

The force field used in this work is the united-atom force field recently proposed by Calero *et al.* [23]. The alkanes are described with a united-atom model, in which CH_3 and CH_2 groups are considered as single, charge-less interaction centers [29]. The beads in the chain are connected by harmonic bonding potentials. A harmonic cosine bending potential models the bond bending between three neighboring beads, and a Ryckaert-Bellemans potential controls the torsional angle. The interactions between the adsorbates as well as the adsorbates and the zeolite are described by Lennard-Jones potentials, and the interactions between the sodium cations and the zeolite are modeled by Coulombic potentials. The parameters used are listed in Table 4.1. For a detailed description of the force field, the reader is referred to Ref. 23.

σ_{ij} ε_{ij}	O_{Al}	O_{Si}	Na	CH_3	CH_2
CH_3	3.48 93	3.48 93	2.65 443.73	3.76 108	3.86 77.7
CH_2	3.58 60.5	3.58 60.5	2.95 310	3.86 77.7	3.96 56.0
Na	3.4 23	3.4 23	2.16 124.4	2.65 443.73	2.95 310
charge	O_{Al}	O_{Si}	Na	Si	Al
q(e)	-1.20	-1.025	+1.00	+2.05	+1.75
bond	$U^{bond} = 1/2k_1(r\text{-}r_0)2$ k_1/k_B = 96500 K/Å^2, r_0=1.54Å				
bend	$U^{bend}=1/2k_2(\cos\theta - \cos\theta_0)^2$ k_2/k_B = 62500K, $\theta_0=114^0$				
torsion	Utorsion= $\sum_{n=0}^{5}\eta_n \cos^n\phi$, η_n/k_B in K				
	η_0	η_1	η_2	η_3	η_4	η_5
	1204.654	1947.740	-357.854	-1944.666	715.690	-1565.572

Table 4.1: Force field parameters used in this work. All parameters listed in this table are taken from Ref.23. σ_{ij}[Å] value is in the Upper Left Corner and ε_{ij}/k_B [K] is in the Lower Right Corner of Each Field. The partial charges [e] of the framework and the sodium cations are given at the lower part of the table. O_{Al} are oxygen atoms bridging one silicon and one aluminum atom, and O_{Si} are oxygen atoms bridging two silicon atoms.

4.2.3 Simulation technique

For the calculation of Henry coefficients we performed configurational-bias Monte Carlo (CBMC) simulations in the *NVT* ensemble. Each simulation consists of at least 4×10^7 cycles and in each cycle one move is chosen at random with a fixed probability 0.1 for a molecule translation, 0.1 for rotation around the center of mass, 0.1 for partial regrowth of a molecule, and 0.7 for regrowth of the entire molecule. During the simulation we compute the Rosenbluth factor, which is directly related to the Henry coefficient [30].

Adsorption isotherms were calculated in the grand-canonical ensemble using the CBMC method. The CB-GCMC method simulates an open system specified by fixed temperature *T*, volume *V*, and fugacity *f*. We converted the imposed fugacity to the

corresponding pressure using the Peng-Robinson equation of state. Four types of moves were carried out: translation, rotation, exchange of molecules between the zeolite and a molecule reservoir, and partial regrowths. All simulations included at least 2×10^7 cycles. As the total number of cations is constant during simulations, only translation movements and regrowth at a random position in the zeolite are considered for these particles.

The statistical uncertainty was estimated by dividing each run into 5 blocks and calculating the standard deviation from the block averages. The standard deviation was within ± 2 % for every simulation. A detailed description of the simulation methods can be found in our previous work [14,19,22,23].

4.3 Results and discussion

4.3.1 Validation of the new force field for Na-MOR zeolites

As a first step towards validation of the applicability to Na-MOR zeolites of the new force field proposed by Calero *et al.* for Na-FAU zeolites, the Henry law coefficients of ethane and linear C_5-C_9 in $Na_8Al_8Si_{40}O_{96}$ were calculated and compared with experimental [7,9] and simulation [9,14] results, as shown in Table 4.2 and Figure 4.1. The new force field shows improved results over previous simulations for ethane and the calculated results for C_5-C_9 are also in good agreement with the experimental values obtained by Denayer *et al.* [7], illustrating that this force field is suitable for Na-MOR zeolites.

***T* [K]**	**273.15**	**296.15**	**323.15**
experimental data[9]	79.103	23.984	7.783
this work	89.100	26.850	8.940
Macedonia *et al.* (simulation data)[9]	61.744	15.905	4.157
Beerdsen *et al.* (simulation data)[14]	90.667	28.965	9.023

Table 4.2: Henry law coefficients [mg/g/kPa] of ethane in the MOR-Na_8 zeolite.

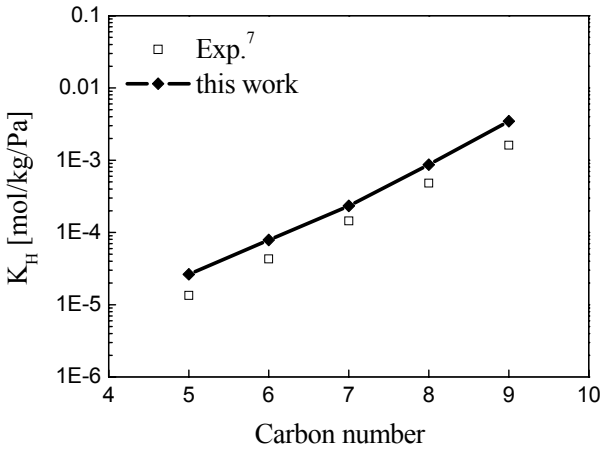

Figure 4.1: Comparison of the experimental [7] and simulated Henry coefficients K_H for C_5-C_9 in MOR-Na_8 zeolite at 598.15 K

To further test the applicability of the new force field, the adsorption isotherms of ethane, propane, butane, and hexane were computed and compared with experimental data [2, 3, 4, 8], as shown in Figures 4.2-4.5. The number of sodium cations and the temperature used for each isotherm were chosen in such a way as to allow a direct comparison with experimental data.

The experimental adsorption isotherms of ethane and hexane in MOR zeolite with 8 Na^+ cations, as obtained from the literatures [2-4], are shown in Figures 4.2 and 4.3, in which our simulated results are also presented. Our computed isotherms are in good agreement with the experimental ones for all the temperatures considered.

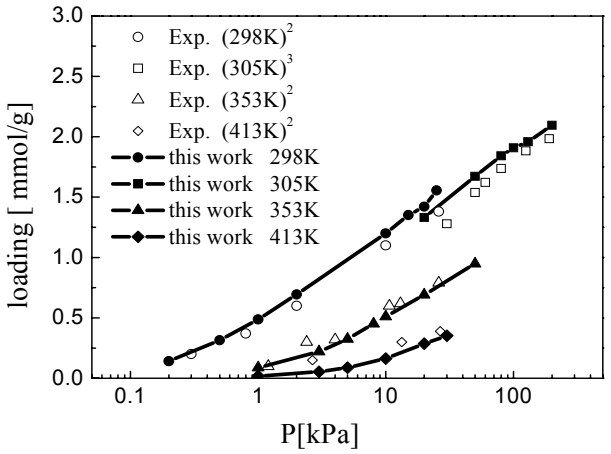

Figure 4.2: Comparison of the experimental [2, 3] and simulated adsorption isotherms of ethane in MOR-Na_8 zeolite.

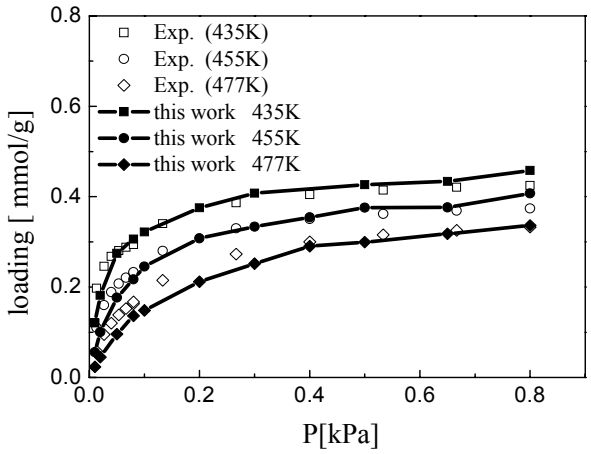

Figure 4.3: Comparison of the experimental [4] and simulated adsorption isotherms of hexane in MOR-Na_8 zeolite.

Additional isotherms were calculated for the MOR zeolites, with 2 Na^+, for propane at 373 K and for butane at 438 K. These results are shown in Figures 4.4 and 4.5, respectively, with the experimental data [8] for comparison.

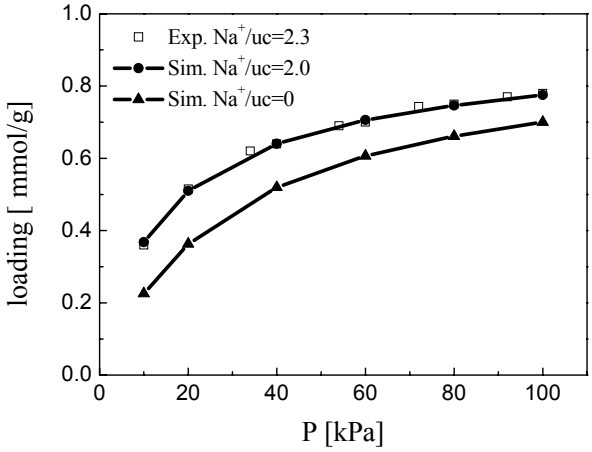

Figure 4.4: Comparison of the experimental [8] and simulated adsorption isotherms of propane in MOR-Na_2 zeolite at 373 K.

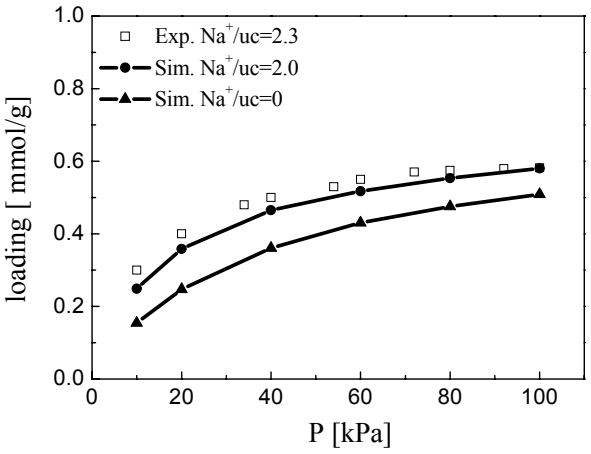

Figure 4.5: Comparison of the experimental [8] and simulated adsorption isotherms of butane in MOR-Na_2 zeolite at 438 K.

Since there are several possible MOR structures with 2 Na^+, the simulation results were obtained by averaging over different aluminum-atom arrangements in the simulation cell (details of the method are given in Section 4.2). To illustrate the importance of including cations in the simulation, we have also performed some calculations on the purely siliceous structure. Experimentally, it is observed that, at a given temperature and pressure, the amount of adsorption increases with increasing sodium density at low and intermediate loadings. Our simulations give a correct trend and are in good agreement with the experimental data [8].

The simulation results of adsorption isotherms together with those of Henry law coefficients show that the force field of Calero *et al.* is applicable for the characterization of Na-MOR zeolites.

4.3.2 Relationship between cation location and alkane adsorption

To study the effects of the cation location on the adsorption behavior, we performed simulations to obtain the adsorption isotherms of butane in six different Na-MOR structures with 6 sodium cations per unit cell (CBV 10A, Zeolyst^{TM} Product) at 343 K. The results are presented in Figure 4.6.

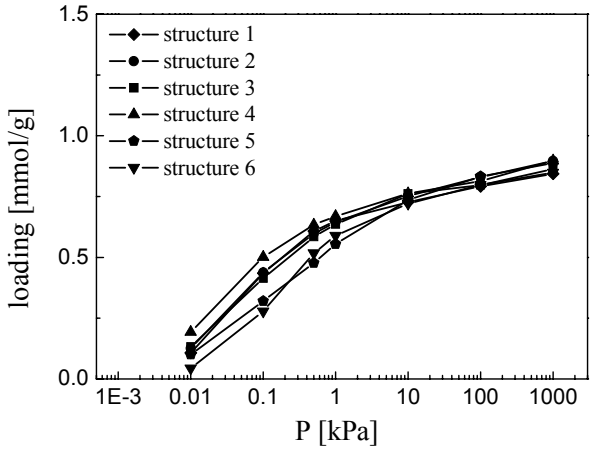

Figure 4.6: Simulated adsorption isotherms of *n*-butane in six MOR-Na6 zeolites 343 K.

Experimentally, it has been observed that the distribution of sodium cations in CBV 10A is essentially random [12]. As the positions and stability of sodium cations in the zeolite are strongly related to its Al distribution [31], three of the six structures we have considered, were obtained by randomly removing Al atoms from the structure corresponding to 8 sodium cations per unit cell and replacing them by silicon atoms (structures 1-3, in Figure 4.6), while the remaining three were built randomly from silicon, aluminum and oxygen following the criteria of previous works [26, 27] (structures 4-6 in Figure 4.6).

Figure 4.6 shows that when the pressure is higher than 10 kPa, the six structures give nearly identical results. But in the pressure range of 0.01-10 kPa, the six structures show different results. Since the side pockets, the small side channels parallel to [010] with 8 AlO_4 or SiO_4 cross sections, are not accessible for larger alkanes [32, 33], adsorption tends to be limited to the main channels. Structure 4, where all 6 sodium cations are located in the main channels, presents the highest adsorption capacity, while structures 5 and 6, with a large amount of aluminum on the crystallographic site T3, corresponding to the sodium cations near site I, i.e. in the small side channels [27, 34], give the lowest adsorption capacity. This illustrates that the presence of non-framework sodium cations creates additional preferred adsorption sites in the zeolites at low and intermediate loadings.

In addition, the effects of alkane adsorption on the cation distribution were also studied. First, we performed simulations on the adsorbate-free MOR with 8 Al atoms per unit cell. Nearly half of the sodium cations were found to reside at site I. These results agree with the available experimental data [25, 35]. This further confirms the applicability of the force field. Next, butane adsorption was simulated at 300 K from 0.01 to 1000 kPa. The results show that the presence of butane in the zeolites does not significantly influence the distribution of cations between site I and the main channel. This in spite of the fact that the number of

possible Na^+ cation positions in the main channel is increased by the presence of butane. Site I is located midway between the 12-ring pores in both the [100] and [010] directions; this area of the zeolite is very constrained, i.e. not accessible to butane. This explains the difference in behavior between MOR and FAU, in the latter it is found that the adsorption of butane redistributes the sodium cations [23].

4.3.3 Adsorption isotherms for linear C_5-C_7

From both scientific and practical points of view, larger alkanes are important. We computed the adsorption isotherms of C_5-C_7 in $Na_8Al_8Si_{40}O_{96}$ and $Na_0Al_0Si_{48}O_{96}$, corresponding to the highest and lowest Al/Si ratios for Na-MOR. The simulation results are shown in Figures 4.7-4.9.

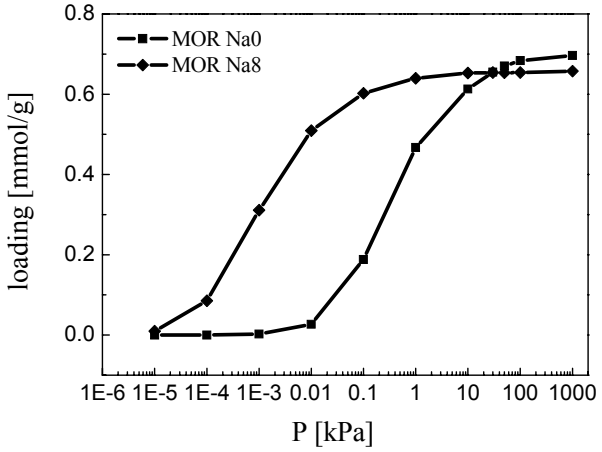

Figure 4.7: Simulated adsorption isotherms of *n*-pentane in MOR-type zeolites with 0 and 8 sodium cations per unit cell at 343 K.

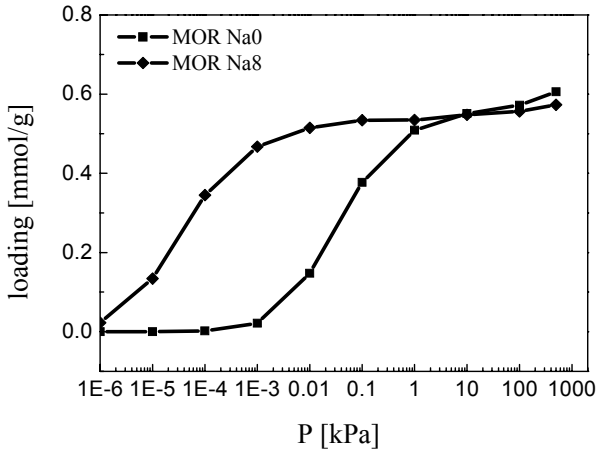

Figure 4.8: Simulated adsorption isotherms of *n*-hexane in MOR-type zeolites with 0 and 8 sodium cations per unit cell at 343 K.

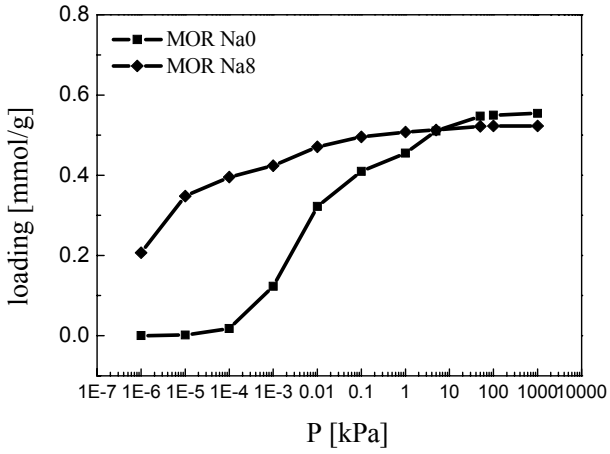

Figure 4.9: Simulated adsorption isotherms of *n*-heptane in MOR-type zeolites with 0 and 8 sodium cations per unit cell at 343 K.

Figure 4.7 shows that, at low pressures, the pressure needed to reach a given loading in the structure without cations is up to 3 orders of magnitude higher than the pressure required in the cationic structure. At elevated pressures, the amount adsorbed in pure silica is higher than that in the structure with cations. As a consequence, there is a well-defined pressure in which the two structures have identical adsorption capacities. These results are attributed to the fact that there are two effects of cations on the adsorption. Cations create additional preferred adsorption sites, which results in an increase of the adsorption, while they also take up adsorption volume, which results in a decrease of the adsorption volume. Which of the two

effects dominates the adsorption depends on the loadings for a given zeolite structure. Generally, at low and intermediate loadings, the first effect dominates, while at high loadings the second effect takes over. A similar trend is observed for C_6 and C_7.

The pressure at which the structures with and without cations show identical adsorption capacities can be called the "reversal pressure", which can be seen as a measure of the effectiveness of the presence of cations (corresponding to the degree of replacement of Si by Al in the frameworks), the lower the reversal pressure, the less effective the cations are for augmenting the adsorption. Therefore, the reversal pressure might be a useful quantity that could be considered in designing or selecting zeolites for a particular process.

A comparison of Figures 4.7-4.9 shows that the effect of cations on the adsorption capacity is more pronounced for smaller alkanes, and the "reversal pressure" shifts to lower pressure (lower loadings) for larger alkanes, as shown in Figure 4.10.

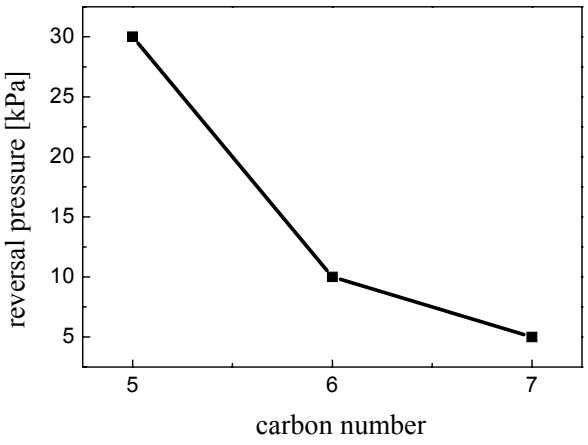

Figure 4.10: "reversal pressure" versus carbon number for C_5-C_7 adsorption in MOR at 343K. The line has been added to guide the eye.

The reason for this is that for a given zeolite structure, the larger the alkane, a larger adsorption volume is required for a certain loading. Hence, the negative effect of cations on the adsorption (cations take up adsorption volume) occurs at lower loading compared to smaller alkanes, leading to the shifting of the "reversal pressure" to lower pressure for larger alkanes. Therefore, it seems the positive effects of cations on the adsorption capacity of alkanes in zeolites become less evident with increasing carbon number. This should be taken into account when a practical process is to be designed.

4.4 Conclusions

The molecular simulation results presented in this work show that the united-atom force field recently proposed by Calero *et al.* for Na-FAU zeolites is applicable to Na-MOR zeolites. Based on this force field, the influence of the location and density of sodium cations on the adsorption behavior of alkanes as well as the adsorption behaviors of larger alkanes (C_5-C_7) in MOR-type zeolites were investigated. In this work the "reversal pressure" was introduced, as a measure for the adsorption of alkanes in cation-containing zeolites. For pressures below the reversal pressure, cations enhance the adsorption, while above the reversal pressure the effects of cations decrease the adsorption. In addition, this work shows that the enhancement of adsorption caused by the presence of cations becomes weaker with increasing alkane length. As a result, the present work not only demonstrates that the new force field is suitable to Na-MOR zeolites, but also provides some useful molecular-level information on the adsorption behavior of alkanes in Na-MOR zeolites, that could contribute to a better understanding of the mechanisms of alkane adsorption in zeolites.

Bibliography

[1] van Bokhoven, J. A.; Tromp, M.; Koningsberger, D. C.; Miller, J. T.; Pieterse, J. A. Z.; Lercher, J. A.; Williams, B.A.; Kung, H. H., *J.Catal.*, 2001, **202**, 129.

[2] Satterfield, C. N.; Frabetti, A. J., Jr., *AIChE J.*, 1967, **13,** 731.

[3] Choudhary, V. R.; Mayadevi, S.; Pai Singh, A., *J. Chem. Soc. Faraday Trans.*, 1995, **91**, 2935.

[4] Eberly, P. E., Jr., *J. Phys. Chem.*, 1963, **67**, 2404.

[5] Xu, Q.; Eguchi, T.; Nakayama, H.; Nakamura, N., *J. Chem. Soc. Faraday Trans.*, 1995, **91**, 2949.

[6] Xu, Q.; Eguchi, T.; Nakayama, H.; Nakamura, N., *J. Chem. Soc. Faraday Trans.*, 1996, **92**, 1039.

[7] Denayer, J. F.; Baron, G. V.; Martens, J. A. and Jacobs, P. A., *J. Phys. Chem. B*, 1998, **102**, 3077.

[8] Webster, C. E.; Cottone, A. III; Drago, R. S., *J. Am. Chem. Soc.*, 1999, **121**, 12127.

[9] Macedonia, M. D.; Moore, D. D.; Maginn, E. J., *Langmuir,* 2000, **16**, 3823.

[10] Yamazaki, T.; Hasegawa, K.; Honma Ken-ichi and Ozawa S., *Phys. Chem. Chem. Phys.*, 2001, **3**, 2686.

[11] Yuvaraj, S.; Chang, T. H.; Yeh, C. T., *J. Phys. Chem. B*, 2003, **107**, 4971.

[12] Salla, I.; Montanari, T.; Salagre, P.; Cesteros, Y. and Busca G., *J. Phys. Chem. B*, 2005, **109**, 915.

[13] Smit, B.; den Ouden, C. J. J., *J. Phys. Chem.*, 1988, **92**, 7169

[14] Beerdsen, E.; Smit, B.; Calero, S., *J. Phys. Chem. B*, 2002, **106**, 10659.

[15] Lu, L.-H.; Wang, Q.; Liu, Y.-C., *J. Phys. Chem. B*, 2005, **109**, 8845.

[16] van Baten, J. M.; Krishna, R., *Micropor. Mesopor. Mater.* , 2005, **84**, 179.

[17] June, R. L.; Bell, A. T.; Theodorou, D. N., *J. Phys. Chem.*, 1992, **96**, 1051.

[18] Smit, B.; Loyens, L. D. J. C.; Verbist, G. L. M. M., *Faraday Discuss.*, 1997, **106**, 93.

[19] Vlugt, T. J. H.; Krishna, R.; Smit, B., *J. Phys. Chem. B*, 1999, **103**, 1102.

[20] Macedonia, M. D.; Maginn, E. J., *Mol. Phys.*, 1999, **96**, 1375.

[21] Pascual, P.; Ungerer, P.; Tavitian, B.; Pernot, P.; Boutin, A., *Phys. Chem. Chem. Phys.*, 2003, **5,** 3684.

[22] Dubbeldam, D.; Calero, S.; Vlugt, T. J. H.; Krishna, R.; Maesen, T. L. M. and Smit, B., *J. Phys. Chem. B*, 2004, **108**, 12301.

[23] Calero, S.; Dubbeldam, D.; Krishna, R.; Smit, B.; Vlugt, T. J. H.; Denayer, J. F. M.; Martens, J.A. and Maesen, T. L. M., *J. Am. Chem. Soc.*, 2004, **126**, 11377.

[24] García-Pérez, E.; Torréns, I. M.; Lago, S.; Dubbeldam, D.; Vlugt, T. J. H.; Maesen, T. L. M.; Smit, B.; Krishna, R.; Calero, S., *Appl. Surf. Sci.*, 2005, **252**, 716.

[25] Meier, W. M. Z., *Z. Kristallogr.*, 1961, **115**, 439.

[26] Ricchiardi, G.; Newsam, J. M., *J. Phys. Chem. B*, 1997, **101**, 9943.

[27] Maurin, G.; Senet, P.; Devautour, S.; Gaveau, P.; Henn, F.; van Doren, V. E.; Giuntini, J. C., *J. Phys. Chem. B*, 2001, **105**, 9157.

[28] Vlugt, T. J. H.; Schenk, M., *J. Phys. Chem. B*, 2002, **106**, 12757.

[29] Ryckaert, J.P.; Bellemans, A., *Faraday Discuss. Chem. Soc*., 1978, **66**, 95.

[30] Frenkel, D.; Smit, B., *Understanding Molecular Simulations: From Algorithms to Applications*, 2nd ed.; Academic Press: San Diego, CA, 2002.

[31] Buttefey, S.; Boutin, A.; Mellot-Draznieks, C.; Fuchs, A. H., *J. Phys. Chem. B*, 2001, **105**, 9569.

[32] Bates, S. P.; van Well, W. J. M.; van Santen, R. A.; Smit, B., *J. Am. Chem. Soc.*, 1996, **118**, 6753.

[33] Bates, S.P.; van Well, W. J. M.; van Santen, R. A.; Smit, B., *J. Phys. Chem.*, 1996, **100**, 17573.

[34] Maurin, G.; Bell, R. G.; Devautour, S.; Henn, F and Giuntini, J. C., *J. Phys. Chem. B*, 2004, **108**, 3739.

[35] International Zeolite Association, Structure Commission, http://www.iza-structure.org.

In our previous work, a computational method to characterize framework aluminium in aluminosilicates was proposed (E. García-Pérez et al., *Angew. Chem. Int. Ed.*, **2007**, *46*, 276). In this work, this method was adopted to identify the most likely positions of aluminium in TON, FER, and MOR zeolites and to understand their different adsorption behavior in detail. The simulations show that the location of aluminium affects the positions of the ions, and thus influences the adsorption. With the determined structures, the effects of non-framework ions on the adsorption behavior of alkanes in these zeolites were studied systematically and the relation between the macroscopic adsorption behavior of alkanes and their microscopic structures was elucidated. The results provided a better understanding of the influences of the position and density of aluminium on adsorption in zeolites from a microscopic level that may guide the future rational synthesis of new structures.

B. Liu, E. García-Pérez, D. Dubbeldam, B. Smit, and S. Calero*

Understanding Aluminium Location and Non-framework Ions Effects on Alkane Adsorption in Aluminosilicates: A Molecular Simulation Study

5.1 Introduction

Zeolites are microporous materials that have found wide applications as efficient heterogeneous catalysts and adsorbents in the petrochemical industry. In these materials the adsorption and diffusion of hydrocarbons in the zeolite pores play an important role [1, 2]. Zeolites are composed of silicon and aluminium oxide tetrahedra and charge-balancing cations. The presence of cations influences the adsorption properties of the zeolites. As the positions and stability of cations in the zeolites are strongly related to their Al distributions [3], it is therefore important to identify the aluminium site locations. Whereas it is relatively easy to determine the Si/Al ratio of the material, it is much more difficult to locate the exact positions of the aluminium atoms in the framework experimentally [4-9]. These difficulties motivate us

* Liu, B.; García-Pérez, E.; Dubbeldam, D.; Smit, B.; Calero, S. *J. Phys. Chem. C* **2007**, *111*, 10419.

to complement the experimental efforts with modeling and simulations.

H-TON, H-FER, and Na-MOR are structures used for industrial applications and many experimental investigations have been performed on the adsorption properties of these zeolites [10-30]. In these studies the positions of the aluminium atoms in these materials are not very clear and the understanding of the effects of non-framework ions on the adsorption properties at the molecular level is yet incomplete. To date most of the simulations [31-39] about the adsorption properties of alkanes have been performed on the pure silica representation of TON and FER zeolites and only a limited number of simulations [26, 40-42] on Na-MOR zeolites. In this work we perform a systematic study on these materials by molecular simulations to reveal the underlying mechanisms at a microscopic level.

The aluminum distribution on the crystal level, as well as the distribution on the level of a single unit cell, remains a subject of much debate and continued research efforts [43-49]. Macroscopically, the amount of aluminium might vary from the center of the crystal to the outer edges, while microscopically the Löwenstein rule, that is, two negatively charged Al atoms can never bond the same O atom, is well established. Because of the periodic boundary conditions, our approach implicitly assumes the same aluminium distribution for the entire zeolite. To obtain some insights in the effect of variations of the amount of aluminium around an average value, we estimated the Henry coefficients of model materials in which some unit cells contain slightly less and others slightly more aluminium concentrations. These calculations agreed very well with those for a uniform aluminium distribution, giving us some confidence that we can compare our results with experimental samples.

The remainder of this chapter is organized as follows. In section 5.2, we present the details of our simulation methodology, including descriptions of the zeolite models, the force fields, and the simulation technique used. In section 5.3, computed Henry coefficients, adsorption isotherms, and heats of adsorption for linear alkanes in several zeolite structures are given, and those in H-TON, H-FER, and Na-MOR zeolites are analyzed and discussed in detail. Finally, some concluding remarks are given in section 5.4.

5.2 Simulation models and methods

5.2.1 Zeolite models

The structures of zeolites considered in this work are well known and have been used in many previous simulation studies. The pure silica structures were constructed by using the crystallographic coordinates reported [50] and the structures with aluminium were obtained by randomly replacing silicon by aluminium atoms, satisfying the Löwenstein rule.

Since TON, FER, and MOR zeolites were studied in detail in this work, their structures

are shown in Figure 5.1, while the structures for the other zeolites considered can be found easily in the literature [41, 51 – 53].

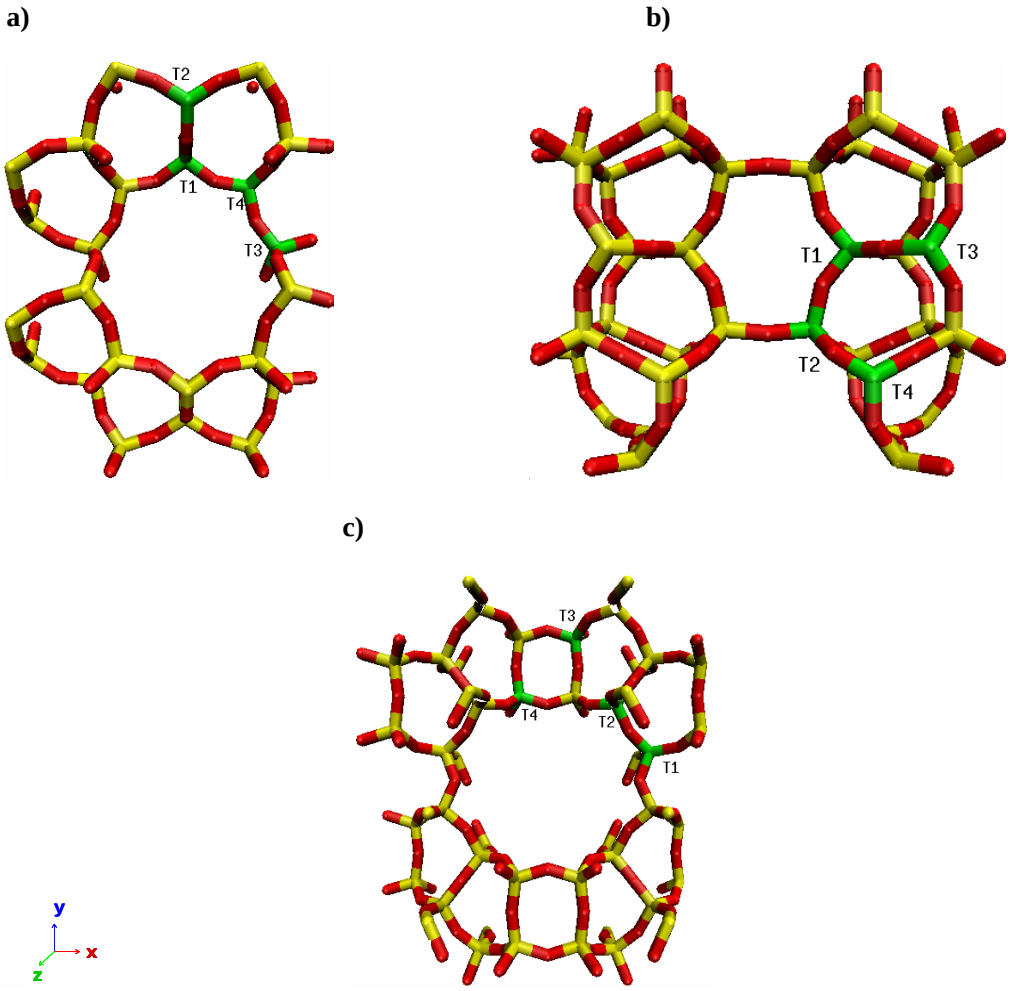

Figure 5.1: Representation of the model unit cell of a) TON, b) FER, and c) MOR with distinct T-sites where Al atoms can be located. Silicon is given in yellow, oxygen is given in red, and the aluminum positions are indicated in green.

The TON-type zeolite exhibits a unidirectional 10-ring pore system along the z-axis, with a pore aperture of 5 Å. The FER-type zeolite consists of straight 10-ring channels (5.4×4.2 Å) parallel to the *z*-axis which are interconnected by cages with 8-ring windows (4.8×3.5 Å) in the *y*-direction. The MOR-type zeolite has main channels parallel to [001], having a slightly elliptical cross section with 12 TO_4 tetrahedron units (T= Si, Al), which are connected with small side channels parallel to [010], with 8 TO_4 cross sections called side pockets. Four distinct T-sites aluminium can be located in them, shown in Figure 5.1 as T1, T2, T3, and T4. The zeolite lattices were assumed to be rigid in the simulations, because the flexibility of the framework has a negligible influence on the adsorption of alkanes [54].

5.2.2 Force fields

Our simulations have been performed using the force field developed by Dubbeldam *et al.*, which accurately reproduce alkane-alkane and alkane-zeolite interactions in all silica structures [55, 56]. Simulations in zeolites with aluminium in the framework require additional parameters for all interactions involving non-framework cations. Consequently, the force fields recently proposed by Calero et al. [51, 57] are used in this work to describe the interactions of sodium cations and protons, both are extensions of the force field of Dubbeldam *et al.* [55, 56]. In these force fields the nature, density, and mobility of the non-framework cations, the density of the framework aluminium, and all host-guest interactions are carefully taken into account. The alkanes are described with a united-atom model, in which CH_4, CH_3, and CH_2 groups are considered as single, charge-less interaction centers [58]. The beads in the chain are connected by harmonic bonding potentials. A harmonic cosine bending potential models the bond bending between three neighboring beads, and a Ryckaert-Bellemans potential controls the torsional angle. The interactions between the adsorbates as well as the adsorbates and the zeolite are described by Lennard-Jones potentials and the interactions between the non-framework ions and the zeolite are modeled by Coulombic potentials. For a detailed description of the force fields, the reader is referred to refs. 51, 55-57.

5.2.3 Simulation technique

For the calculation of the Henry coefficients and the isosteric heats of adsorption at infinite dilution Q_{st}^0, we performed configurational-bias Monte Carlo (CBMC) simulations in the *NVT* ensemble. Each simulation consists of at least 4×10^7 cycles, and in each cycle one move is chosen at random with a fixed probability 0.1 for a molecule translation, 0.1 for rotation around the center of mass, and 0.8 for regrowth of the entire molecule. During the simulation we compute the Rosenbluth factor and the internal energy ΔU, which are directly related to the Henry coefficients and the Q_{st}^0 [56, 59].

Adsorption isotherms were calculated in the grand-canonical ensemble using the CBMC method. The CB-GCMC method simulates an open system specified by fixed temperature *T*, volume *V*, and fugacity *f*. We converted the imposed fugacity to the corresponding pressure using the Peng-Robinson equation of state. Four types of moves were carried out: translation, rotation, exchange of molecules between the zeolite and a molecule reservoir, and partial regrowth. All simulations included at least 2×10^7 cycles. As the total number of ions is constant during simulations, only translation movements and regrowth at a random position in the zeolite are considered for these particles.

The statistical uncertainty was estimated by dividing each run into five blocks and calculating the standard deviation from the block averages. The standard deviation was within

± 10 % for every simulation. A detailed description of the simulation methods can be found in our previous work [51].

5.3 Results and discussion

5.3.1 Categorizing zeolites according to the sensitivity of adsorption properties to the aluminium distributions

In this work, we firstly categorized the commonly used zeolites (FAU, LTA, MEL, MFI, LTL, FER, MOR, and TON) into two groups according to the sensitivity of their adsorption properties to the details of the aluminium distributions by computing the Henry coefficients of linear alkanes in these materials. The results are shown in Figure 5.2. In the simulations the Si/Al ratio is kept fixed for each zeolite by varying the aluminium distribution for different structures (the details about the exact location of the Al atoms in the different structures are given in Tables 5.1-5.5) and using Na^+ and H^+ as non-framework ions.

a) FAU - 52Na$^+$/uc

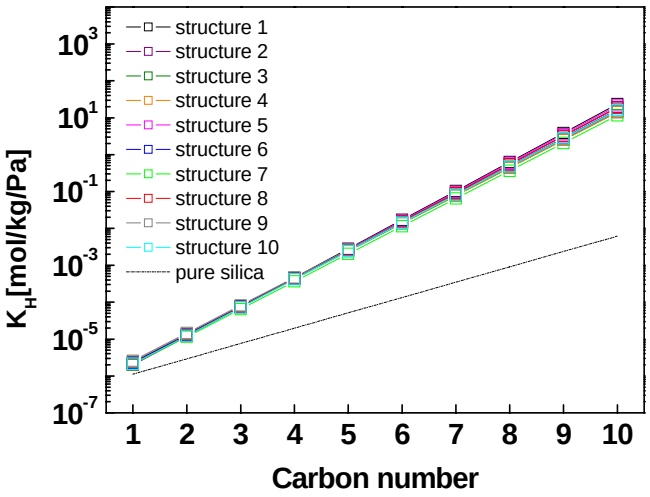

b) LTA - 48Na$^+$/uc

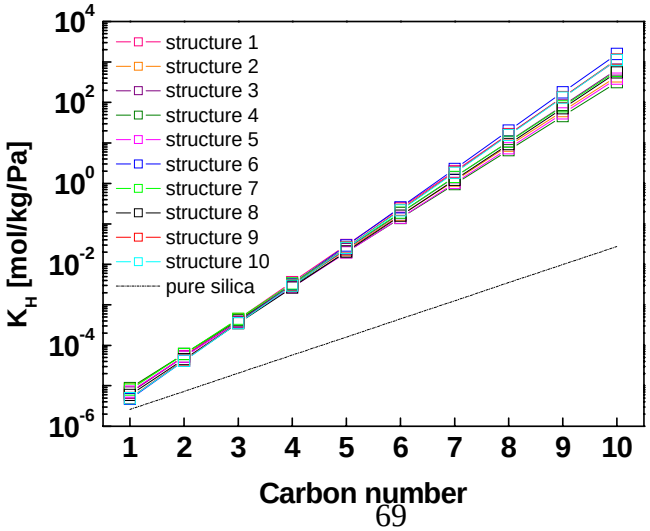

c) MEL - 4Na$^+$/uc

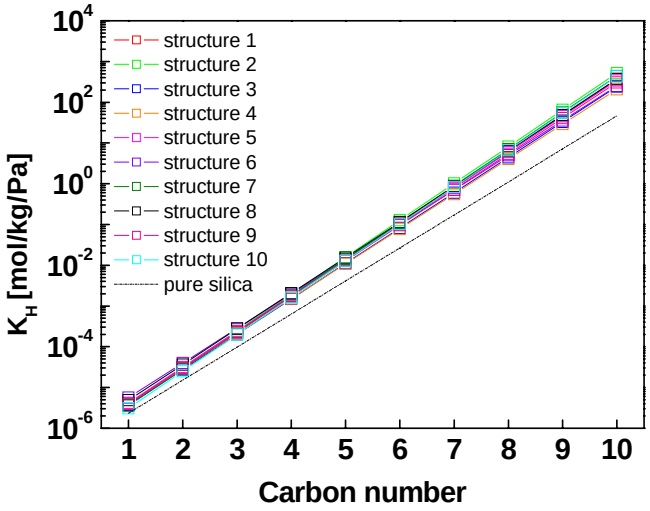

d) MFI – 4Na$^+$/uc

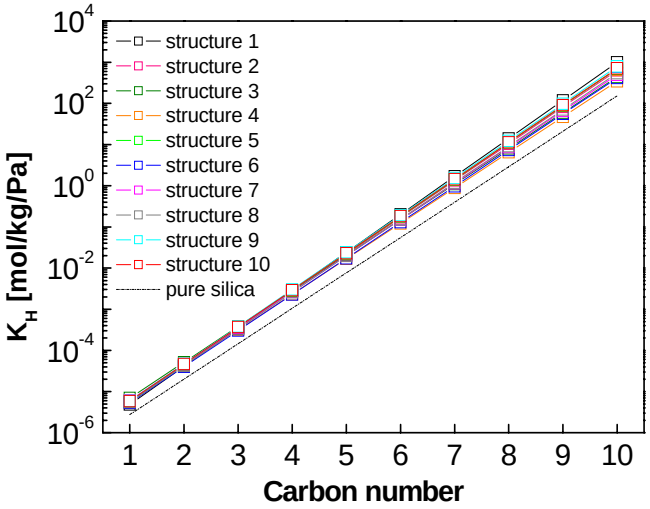

e) LTL - 6Na$^+$/uc

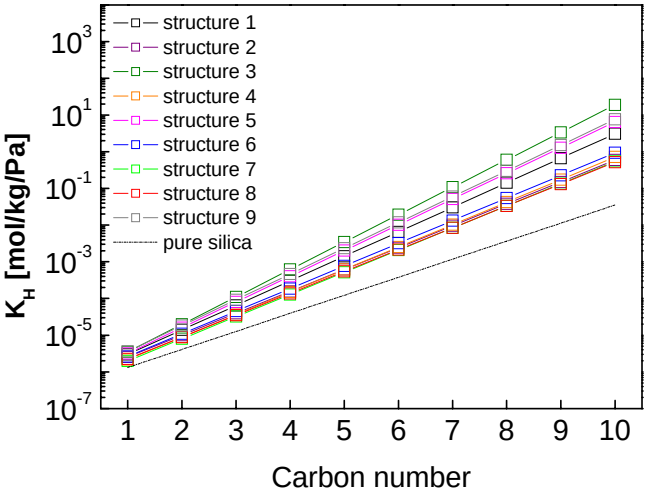

f) FER - 4Na$^+$/uc

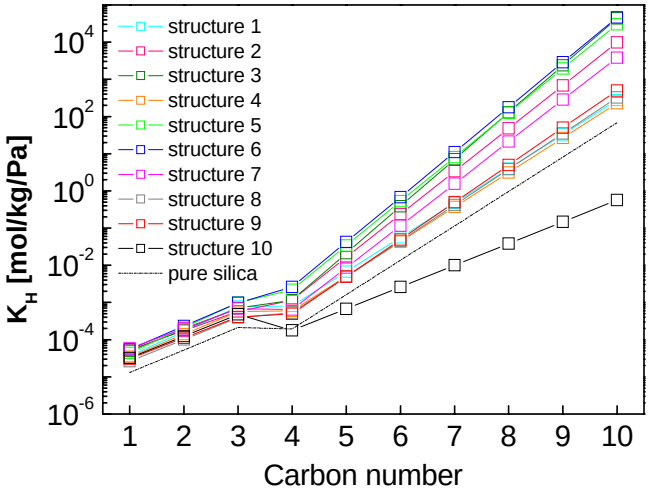

g) MOR - 4Na$^+$/uc

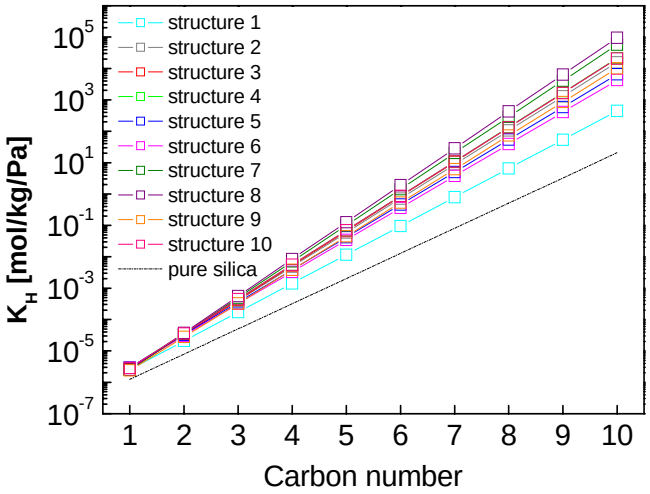

h) TON – 1H$^+$/uc

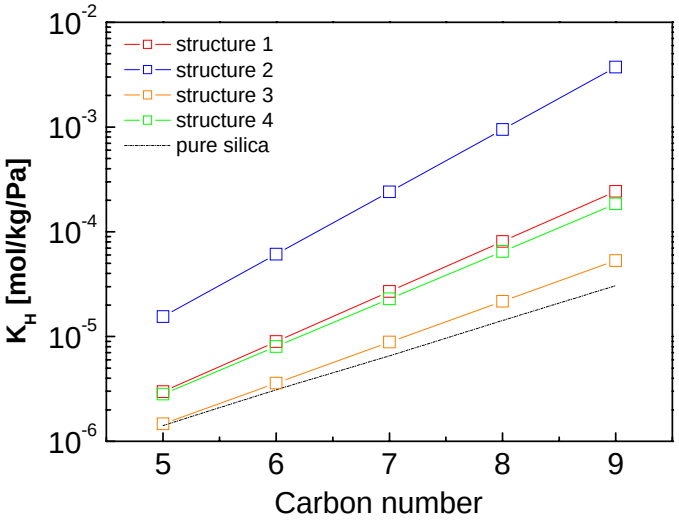

Figure 5.2: Henry coefficients of linear alkanes in a) FAU, b) LTA, c) MEL, d) MFI, e) LTL, f) FER, g) MOR zeolites at 350 K and h) TON zeolite at 548 K.

	Al location sites
Structure 1	Si2, Si26, Si38, Si44, Si62, Si68, Si86, Si92, Si98, Si110, Si134, Si140, Si158, Si164, Si176, Si182, Si188, Si194, Si224, Si230, Si236, Si242, Si248, Si272, Si284, Si290, Si314, Si332, Si344, Si350, Si356, Si368, Si380, Si392, Si404, Si410, Si416, Si422, Si428, Si434, Si440, Si452, Si458, Si470, Si476, Si500, Si506, Si512, Si536, Si542, Si554, and Si560.
Structure 2	Si2, Si8, Si14, Si20, Si26, Si44, Si50, Si68, Si74, Si80, Si92, Si104, Si110, Si116, Si128, Si134, Si146, Si152, Si164, Si170, Si188, Si218, Si230, Si236, Si242, Si248, Si254, Si278, Si284, Si308, Si314, Si332, Si338, Si344, Si350, Si356, Si374, Si386, Si398, Si404, Si422, Si434, Si446, Si452, Si494, Si500, Si506, Si512, Si530, Si542, Si560, and Si572.
Structure 3	Si14, Si38, Si50, Si56, Si62, Si68, Si80, Si92, Si116, Si140, Si158, Si164, Si182, Si188, Si194, Si200, Si230, Si236, Si242, Si248, Si260, Si284, Si290, Si302, Si314, Si326, Si332, Si344, Si356, Si362, Si374, Si392, Si404, Si410, Si428, Si434, Si440, Si452, Si458, Si464, Si470, Si476, Si482, Si488, Si494, Si500, Si512, Si518, Si530, Si536, Si542, and Si572.
Structure 4	Si2, Si8, Si20, Si26, Si44, Si56, Si80, Si104, Si110, Si122, Si128, Si134, Si140, Si146, Si152, Si176, Si182, Si188, Si194, Si206, Si218, Si224, Si230, Si254, Si260, Si272, Si284, Si296, Si302, Si314, Si332, Si344, Si368, Si380, Si386, Si398, Si404, Si410, Si416, Si440, Si446, Si452, Si458, Si470, Si476, Si488, Si494, Si530, Si542, Si548, Si554, and Si566.
Structure 5	Si2, Si8, Si14, Si26, Si32, Si38, Si50, Si56, Si74, Si92, Si98, Si104, Si128, Si140, Si152, Si158, Si164, Si170, Si176, Si182, Si188, Si200, Si206, Si218, Si224, Si236, Si254, Si260, Si284, Si290, Si314, Si320, Si338, Si344, Si368, Si374, Si392, Si428, Si434, Si440, Si452, Si464, Si476, Si488, Si494, Si500, Si506, Si518, Si530, Si548, Si554, and Si566.
Structure 6	Si56, Si62, Si74, Si86, Si98, Si104, Si122, Si134, Si140, Si152, Si158, Si182, Si188, Si194, Si200, Si206, Si218, Si230, Si236, Si242, Si254, Si278, Si284, Si290, Si296, Si308, Si320, Si326, Si332, Si344, Si350, Si356, Si362, Si368, Si380, Si392, Si404, Si410, Si416, Si428, Si440, Si452, Si458, Si470, Si494, Si500, Si506, Si518, Si524, Si536. Si554, and Si566.
Structure 7	Si14, Si20, Si50, Si56, Si68, Si86, Si104, Si110, Si116, Si122, Si128, Si134, Si152, Si158, Si164, Si170, Si176, Si188, Si200, Si206, Si218, Si224, Si230, Si236, Si242, Si254, Si260, Si266, Si272, Si302, Si308, Si314, Si326, Si332, Si344, Si356, Si362, Si368, Si404, Si422, Si434, Si440, Si458, Si470. Si476, Si482, Si530, Si536, Si542, Si560, and Si572.
Structure 8	Si44, Si50, Si56, Si62, Si74, Si86, Si104, Si110, Si116, Si128, Si140, Si146, Si152, Si170, Si176, Si182, Si194, Si206, Si224, Si242, Si248, Si260, Si266, Si272, Si290, Si296, Si302, Si308, Si314, Si320, Si332,Si338, Si344, Si350, Si362, Si368, Si374, Si380, Si398, Si410, Si416, Si428, Si434, Si440, Si452, Si458, Si464, Si476, Si494, Si518, Si530, and Si542.
Structure 9	Si8, Si32, Si38, Si44, Si50, Si56, Si62, Si68, Si80, Si86, Si98, Si110, Si128, Si134, Si140, Si164, Si176, Si188, Si194, Si206, Si218, Si224, Si236, Si248, Si260, Si266, Si272, Si296, Si302, Si314, Si326, Si344, Si368, Si380, Si386, Si392, Si416, Si440, Si446, Si458, Si464, Si470, Si476, Si494, Si500, Si518, Si536, Si548, Si554, Si560, Si566, and Si572.
Structure 10	Si14, Si56, Si62, Si74, Si80, Si86, Si98, Si104, Si122, Si134, Si140, Si152, Si158, Si164, Si182, Si188, Si194, Si200, Si206, Si218, Si230, Si236, Si242, Si254, Si266, Si272, Si278, Si284, Si290, Si296, Si308, Si320, Si326, Si332, Si338, Si344, Si350, Si356, Si362, Si368, Si380, Si392, Si404, Si410, Si416, Si428, Si440, Si452, Si458, Si494, Si500, and Si506.

Table 5.1: Structural Information for FAU zeolite considered in this work.

	Al location sites
Structure 1	Si17, Si27, Si47, Si52, Si57, Si72, Si77, Si87, Si102, Si112, Si171, Si181, Si191, Si196, Si211, Si216, Si231, Si236, Si246, Si251, Si261, Si295, Si300, Si305, Si320, Si340, Si350, Si355, Si365, Si375, Si380, Si385, Si400, Si439, Si454, Si469, Si474, Si479, Si484, Si499, Si504, Si519, Si524, Si529, Si534, Si539, Si544, and Si549.
Structure 2	Si12, Si17, Si32, Si47, Si57, Si67, Si72, Si82, Si87, Si92, Si107, Si117, Si151, Si156, Si166, Si171, Si181, Si186, Si196, Si201, Si211, Si221, Si226, Si231, Si241, Si246, Si251, Si261, Si295, Si300, Si315, Si320, Si330, Si340, Si345, Si355, Si365, Si380, Si390, Si400, Si439, Si444, Si454, Si474, Si494, Si514, Si524, and Si534.
Structure 3	Si2, Si22, Si32, Si42, Si52, Si62, Si72, Si82, Si92, Si102, Si112, Si146, Si156, Si161, Si171, Si181, Si191, Si196, Si206, Si211, Si216, Si226, Si231, Si241, Si251, Si261, Si295, Si305, Si310, Si315, Si325, Si335, Si350, Si360, Si370, Si375, Si385, Si395, Si405, Si439, Si444, Si454, Si489, Si504, Si519, Si529, Si539, and Si544.
Structure 4	Si7, Si12, Si22, Si32, Si47, Si57, Si67, Si72, Si77, Si82, Si87, Si92, Si107, Si117, Si156, Si166, Si176, Si181, Si191, Si196, Si201, Si211, Si221, Si231, Si236, Si246, Si251, Si261, Si300, Si310, Si320, Si335, Si350, Si360, Si370, Si400, Si439, Si454, Si474, Si504, Si514, Si519, Si524, Si529, Si534, Si539, Si544, and Si549.
Structure 5	Si12, Si67, Si77, Si87, Si117, Si156, Si166, Si206, Si216, Si221, Si241, Si290, Si295, Si300, Si310, Si320, Si330, Si340, Si345, Si350, Si355, Si360, Si365, Si370, Si375, Si380, Si385, Si390, Si395, Si400, Si405, Si434, Si439, Si444, Si449, Si454, Si459, Si464, Si469, Si494, Si504, Si514, Si519, Si524, Si534, Si539, Si544, and Si549.
Structure 6	Si12, Si22, Si27, Si32, Si37, Si42, Si47, Si52, Si67, Si77, Si87, Si92, Si102, Si112, Si151, Si161, Si166, Si181, Si191, Si196, Si201, Si206, Si226, Si231, Si290, Si300, Si315, Si325, Si335, Si345, Si360, Si370, Si380, Si390, Si400, Si439, Si444, Si454, Si469, Si479, Si494, Si504, Si509, Si514, Si534, Si539, Si544, and Si549.
Structure 7	Si2, Si7, Si12, Si17, Si27, Si37, Si47, Si52, Si57, Si67, Si72, Si82, Si87, Si97, Si107, Si117, Si151, Si156, Si166, Si176, Si186, Si196, Si206, Si256, Si295, Si305, Si325, Si345, Si355, Si360, Si370, Si380, Si385, Si400, Si439, Si444, Si454, Si464, Si469, Si479, Si489, Si499, Si504, Si514, Si519, Si529, Si539, and Si549.
Structure 8	Si2, Si7, Si17, Si27, Si32, Si42, Si47, Si57, Si67, Si77, Si97, Si102, Si146, Si151, Si156, Si161, Si166, Si181, Si196, Si201, Si206, Si211, Si221, Si231, Si241, Si246, Si251, Si261, Si300, Si305, Si310, Si325, Si330, Si340, Si345, Si360, Si365, Si380, Si385, Si400, Si439, Si444, Si459, Si464, Si484, Si494, Si509, and Si519.
Structure 9	Si7, Si17, Si27, Si42, Si72, Si87, Si107, Si151, Si156, Si166, Si176, Si181, Si191, Si196, Si206, Si216, Si221, Si236, Si241, Si251, Si256, Si295, Si300, Si305, Si325, Si330, Si340, Si345, Si360, Si370, Si380, Si395, Si405, Si439, Si444, Si449, Si454, Si459, Si464, Si474, Si479, Si489, Si499, Si504, Si509, Si524, Si529, and Si539.
Structure 10	Si2, Si12, Si17, Si27, Si32, Si47, Si72, Si77, Si82, Si87, Si92, Si97, Si102, Si107, Si112, Si117, Si161, Si166, Si176, Si181, Si196, Si201, Si206, Si216, Si221, Si226, Si236, Si241, Si246, Si256, Si261, Si290, Si295, Si305, Si310, Si315, Si330, Si345, Si355, Si395, Si400, Si454, Si479, Si484, Si494, Si504, Si529, and Si534.

Table 5.2: Structural Information for LTA zeolite considered in this work.

	Al location sites	
	MEL	**MFI**
Structure 1	Si7, Si50, Si67, and Si125.	Si10, Si124, Si162, and Si264.
Structure 2	Si27, Si72, Si90, and Si178.	Si3, Si11, Si225, and Si263.
Structure 3	Si2, Si73, Si193, and Si278.	Si39, Si164, Si197, and Si260.
Structure 4	Si1, Si68, Si137, and Si153.	Si39, Si163, Si197, and Si266.
Structure 5	Si45, Si71, Si72, and Si125.	Si1, Si195, Si230, and Si265.
Structure 6	Si3, Si67, Si92, and Si137.	Si42, Si48, Si88, and Si259.
Structure 7	Si3, Si29, Si137, and Si153.	Si10, Si154, Si197, and Si266.
Structure 8	Si2, Si27, Si69, and Si122.	Si10, Si163, Si196, and Si265.
Structure 9	Si5, Si29, Si73, and Si125.	Si115, Si158, Si192, and Si221.
Structure 10	Si7, Si50, Si73, and Si92.	Si10, Si41, Si50, and Si83.

Table 5.3: Structural Information for MEL and MFI zeolites considered in this work.

	Al location sites		
	LTL	**FER**	**TON**
Structure 1	Si34, Si66, Si82, Si110, Si121, and Si145.	Si4, Si15, Si36, and Si73.	Si1
Structure 2	Si35, Si67, Si83, Si111, Si122, and Si146.	Si14, Si27, Si43, and Si97.	Si2
Structure 3	Si1, Si33, Si65, Si81, Si109, and Si124.	Si1, Si47, Si51, and Si106.	Si3
Structure 4	Si17, Si36, Si52, Si84, Si99, and Si123.	Si25, Si35, Si62, and Si81.	Si4
Structure 5	Si4, Si33, Si81, Si112, Si122, and Si145.	Si43. Si51, Si72, and Si100.	
Structure 6	Si3, Si35, Si65, Si98, Si186, and Si202.	Si16, Si34, Si55, and Si72.	
Structure 7	Si19, Si84, Si121, Si174, Si201, and Si210.	Si14, Si47, Si72, and Si91.	
Structure 8	Si4, Si19, Si52, Si83, Si124, and Si129.	Si34, Si60, Si73, and Si103.	
Structure 9	Si35, Si66, Si97, Si121, Si148, and Si209.	Si3, Si25, Si81, and Si106.	
Structure 10	Si2, Si51, Si97, Si123, Si145, and Si189.	Si13, Si51, Si90, and Si106.	

Table 5.4: Structural Information for LTL, FER, and TON zeolites considered in this work.

	Al location sites
	MOR
Structure 1	Si3, Si17, Si32, Si43, Si79, Si92, Si106, and Si116.
Structure 2	Si3, Si17, Si32, Si43, Si79, Si93, Si106, and Si115.
Structure 3	Si3, Si17, Si32, Si43, Si80, Si92, Si105, and Si116.
Structure 4	Si3, Si17, Si32, Si43, Si89, Si93, Si105, and Si115.
Structure 5	Si3, Si18, Si32, Si42, Si79, Si92, Si106, and Si116.
Structure 6	Si3, Si18, Si32, Si42, Si79, Si93, Si106, and Si115.
Structure 7	Si3, Si18, Si32, Si42, Si80, Si92, Si105, and Si116.
Structure 8	Si3, Si18, Si32, Si42, Si80, Si93, Si105, and Si115.
Structure 9	Si4, Si17, Si31, Si43, Si79, Si92, Si106, and Si116.
Structure 10	Si4, Si17, Si31, Si43, Si79, Si93, Si106, and Si115.
Structure 11	Si4, Si17, Si31, Si43, Si80, Si92, Si105, and Si116.
Structure 12	Si4, Si17, Si31, Si43, Si80, Si93, Si105, and Si115.
Structure 13	Si4, Si18, Si31, Si42, Si79, Si92, Si106, and Si116.
Structure 14	Si4, Si18, Si31, Si42, Si79, Si93, Si106, and Si115.
Structure 15	Si4, Si18, Si31, Si42, Si80, Si92, Si105, and Si116.
Structure 16	Si4, Si18, Si31, Si42, Si80, Si93, Si105, and Si115.

Table 5.5: Structural Information for MOR zeolite considered in this work.

The results (see Figure 5.2) show that the adsorption properties of FAU, LTA, MEL, and MFI are insensitive to aluminium distribution and they can be included in the insensitive group, while LTL, FER, TON, and MOR belong to the sensitive class. Therefore, the first group of zeolites can be used to accurately parameterize our simulation method [51, 57] and for the second group of zeolites, their average aluminium distributions can be identified by matching the simulations with experiments using the parameterized simulation method [60].

5.3.2 Aluminium positions and alkane adsorptions in TON, FER, and MOR zeolites

We have performed molecular simulations to identify the aluminium positions in TON, FER, and MOR zeolites, as well as to provide a better molecular understanding of the alkane adsorption in them. For these zeolites, experimental adsorption data are available, and it is feasible to consider all possible aluminium distributions per unit cell: $H^{+}_{1}[Al_1Si_{23}O_{48}]$-TON, $H^{+}_{1}[Al_1Si_{35}O_{72}]$-FER (both with 4 possible aluminium distributions per unit cell), and $Na^{+}_{8}[Al_8Si_{40}O_{96}]$-MOR (with 16 possible aluminium distributions per unit cell).

H-TON zeolite

Figure 5.3 shows the calculated Henry coefficients of linear alkanes in H-TON zeolite at 473 K, 498 K, 523 K, and 573 K. The number of protons is kept one per unit cell to allow a direct comparison with experimental data. Since there are four distinct T-sites where aluminum can be located and as the positions and stability of protons in the zeolite are strongly related to its Al distribution [3], four different structures were considered in this work, which correspond to the four T-sites. A comparison with the experimental values [16] indicates that most of the aluminium atoms on the zeolite sample are a combination of T3 and T4 substitutions for H-TON structures. Simulation at 548 K was also performed showing similar behavior (see ref. 60).

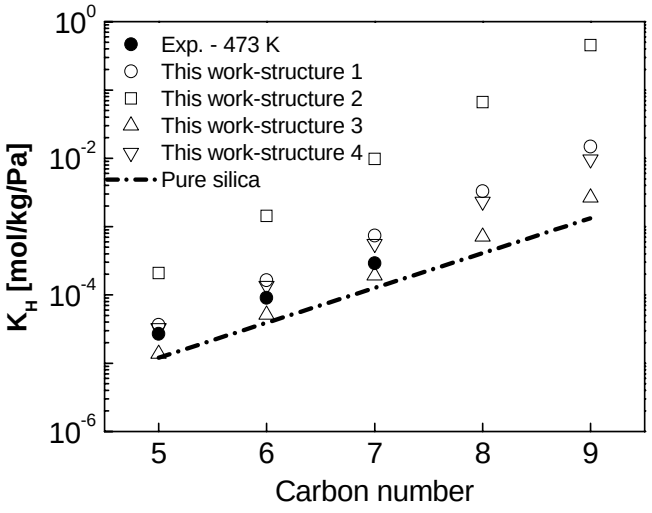

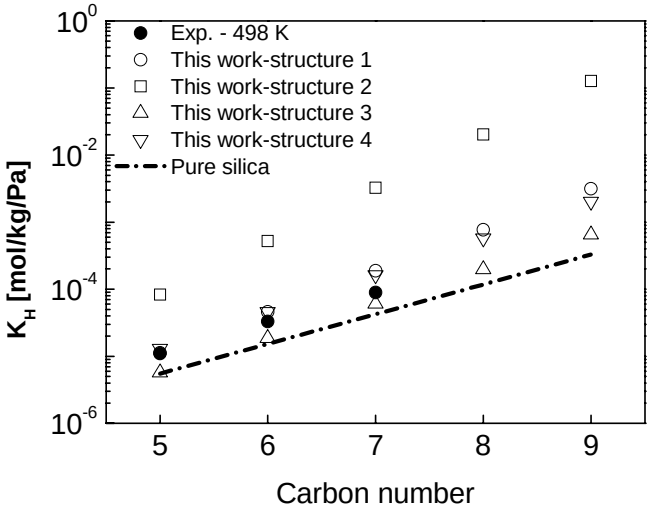

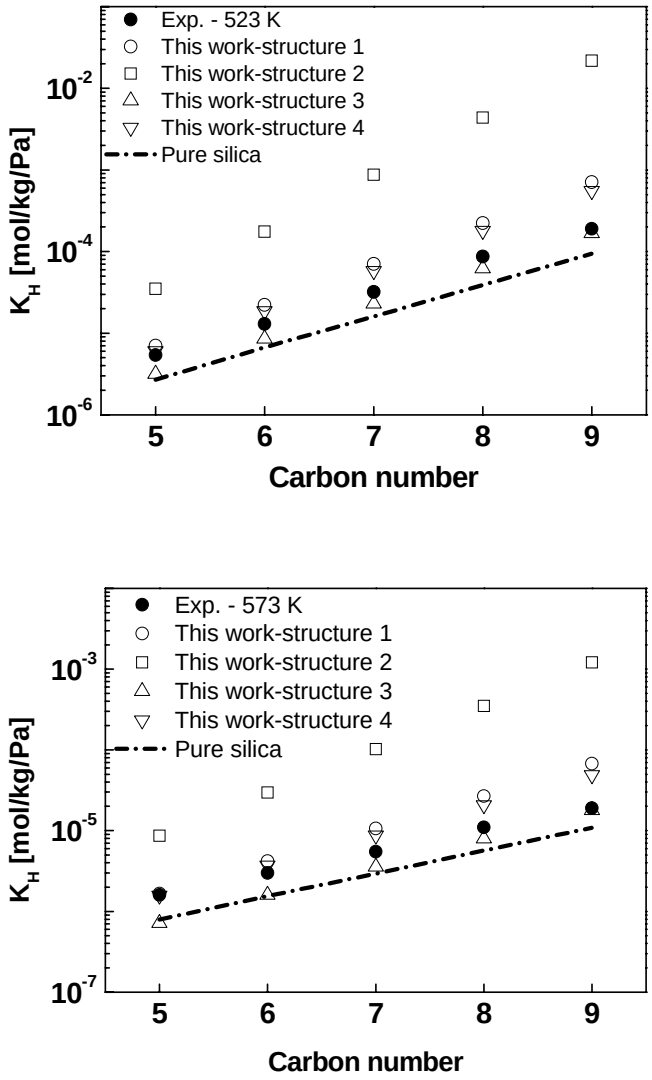

Figure 5.3: Comparison of the experimental [16] and simulated Henry coefficients of linear alkanes in H-TON zeolites at 473 K, 498 K, 523 K, and 573 K. Structures 1, 2, 3, and 4 indicate that the Al atom is located in T-site 1, 2, 3, and 4, respectively.

To clarify the differences among the structures, we examined the snapshots of these zeolites with adsorbed alkanes and those for hexane are shown in Figure 5.4.

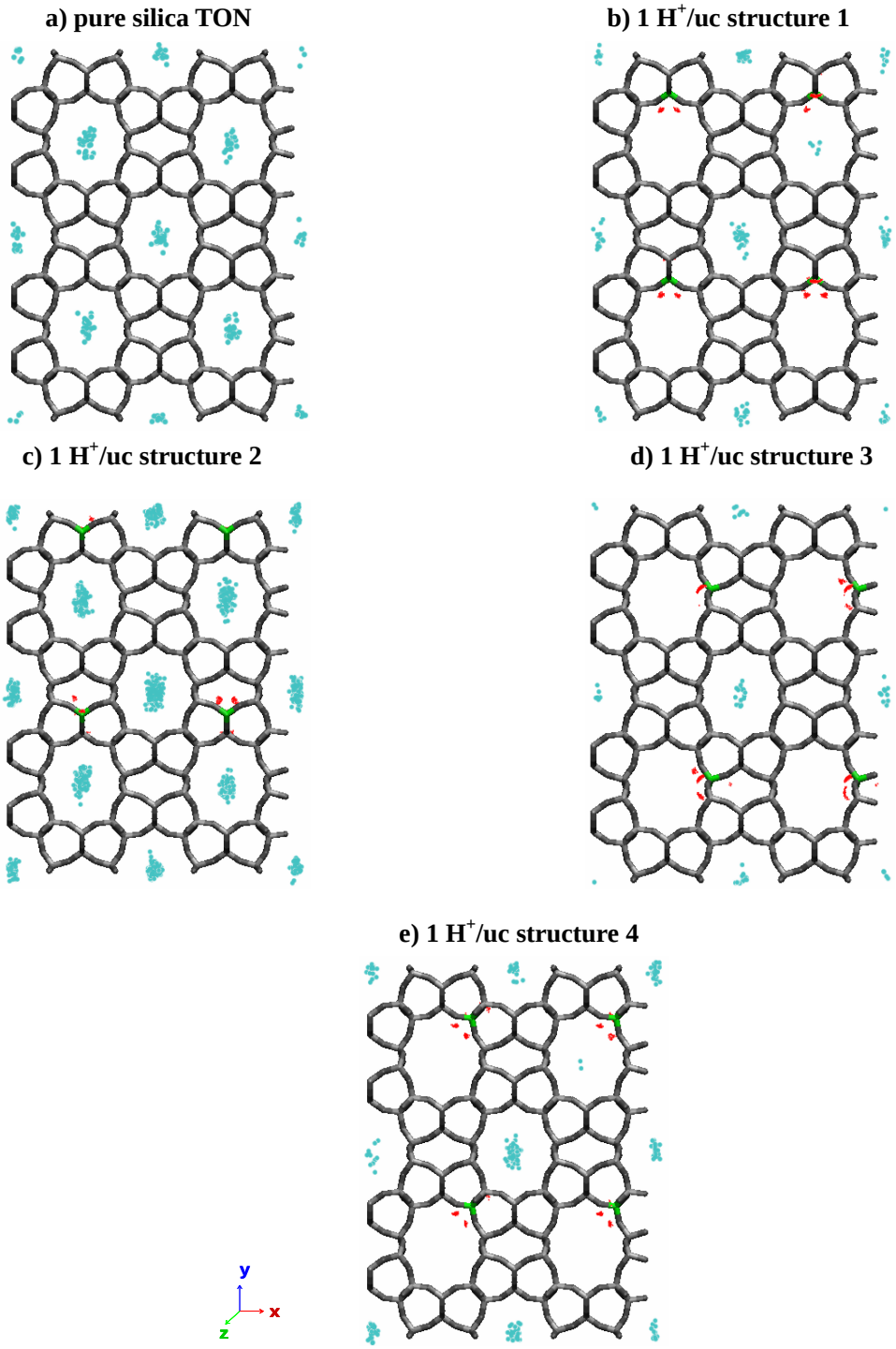

Figure 5.4: Distributions of hexane and the non-framework protons in TON zeolites at 5 kPa and 548 K. The centers of mass of the hexane molecules are represented by blue dots and the non-framework proton positions by red dots. The aluminum positions are indicated in green color.

To illustrate the influences of protons on the adsorption, the results on pure silica structure are also shown for comparison. In the pure silica structure, the hexane molecules adsorb homogeneously throughout the channels. In structures 1 and 4, protons were found to be partly

located in the 10-ring channel. Protons take up adsorption volume in the channels where they are located but create additional preferred adsorption sites in the neighboring channels, which results in an increase of the adsorption comparing with the pure silica structure. As discussed in ref. 57 the proton model assumes that there some traces of water in contact with the proton providing an effective adsorption volume that is significantly larger than one would expect from a single proton. We found that protons were all excluded from the 10-ring channels for structure 2 and they do increase the amount of adsorption in all 10-ring channels, leading to the highest adsorption capacity. The preferential location for proton in structure 3 is the 10-ring channels and the snapshot shows that protons occupy much volume in the channels, giving the lowest adsorption amount.

H-FER zeolite

The adsorption behavior of alkanes in H-FER zeolite was further investigated. Figure 5.5 shows the calculated adsorption isotherms of propane at 333 K. Again the number of protons is kept one per unit cell and four different structures were considered corresponding to the four T-sites. Figure 5.5 shows that the calculated isotherms based on structure 3, that is, Al located on T3 agree very well with the experimental data.

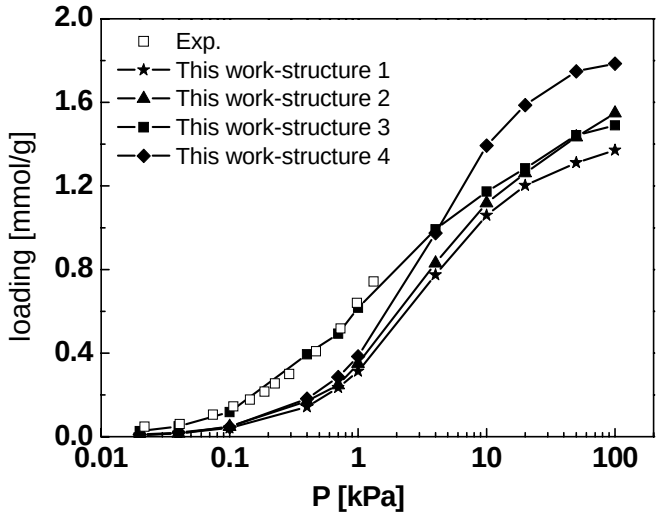

Figure 5.5: Comparison of the experimental [13] and simulated adsorption isotherms of propane in H-FER zeolite at 333 K. Structures 1, 2, 3, and 4 indicate that the Al atom is located in T-site 1, 2, 3, and 4 respectively.

The adsorption isotherms of butane, pentane, and hexane show similar behavior (see ref. 60 and Figure 5.6), illustrating that T3 structure is most likely the structure of the H-FER

experimental sample.

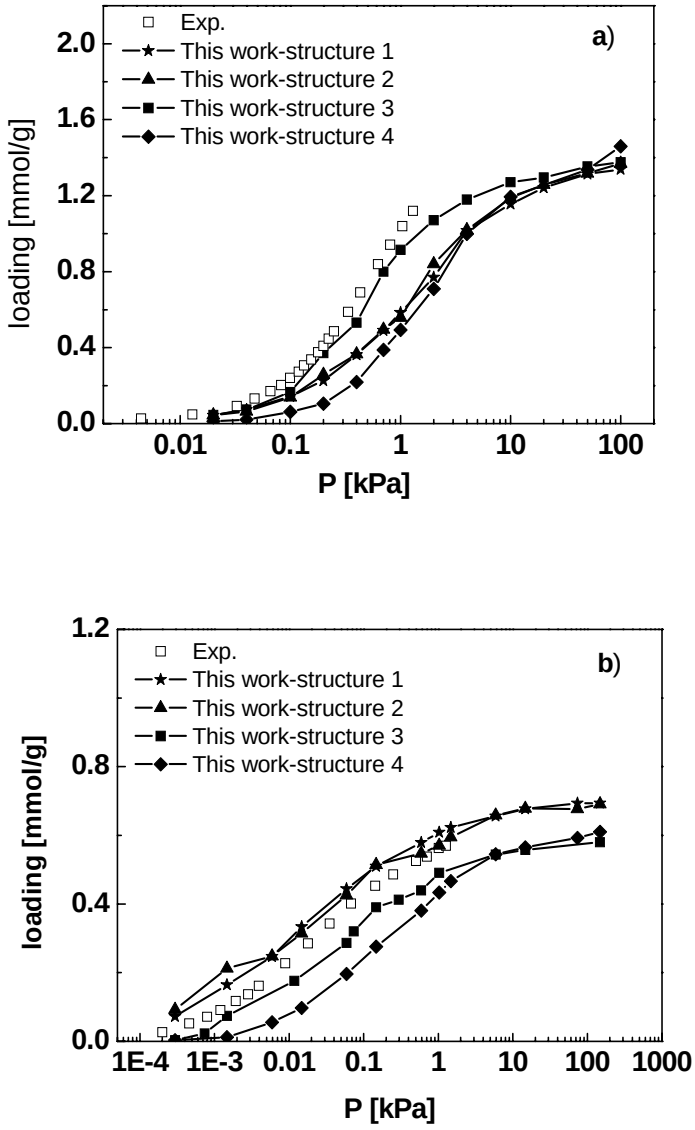

Figure 5.6: Comparison of the experimental [13] and simulated adsorption isotherms of a) *n*-butane and b) *n*-hexane in H-FER zeolite at 333 K. Structures 1, 2, 3, and 4 indicate that the Al atom is located in T-site 1, 2, 3, and 4 respectively.

Heats of adsorption were also computed for this structure and comparison with experimental data [13] is provided in Table 5.6.

	propane	***n*-butane**	***n*-pentane**	***n*-hexane**
experimental data[13]	49	59	69	79
this work	48.43	57.14	67.72	81.90

Table 5.6: Comparison of the experimental and simulated heats of adsorption Q_{st}^{0} [kJ/mol] of C_3-C_6 in H-FER zeolites

The snapshots of the different structures with adsorbed alkanes were examined and those for butane are given, as an example, in Figure 5.7. The snapshots show that butane molecules are distributed over the channels and the cages for all structures considered. For pure silica structure, butane molecules are located almost homogeneously between the channels and the cages. For structure 1, proton was found located in the 8-ring cages and butane molecules adsorbed preferentially in the 10-ring channels. Protons take up adsorption volume in the 8-ring cages but create additional preferred adsorption sites in the 10-ring channels, resulting in an increase of the adsorption. For structure 2, we found that the probability for protons located in the 8-ring cages and the 10-ring channels is almost the same and from the snapshot we can see that protons affect adsorption in a similar way as in structure 1, that is, decreasing the adsorption in the 8-ring cages but increasing it in the 10-ring channels. The preferential locations of protons in structure 3 are the 10-ring channels, which agrees well with the experimental results [13]. The protons occupy some volume in the 10-ring channels but the influence is not as big as in 8-ring cages. At low and intermediate loadings, protons increase the amount of adsorption in both the 10-ring channels and the 8-ring cages, leading to the highest adsorption capacity. In structure 4, the preferential location for protons is the region across the 8-ring cages and the 10-ring channels, giving the lowest adsorption capacity. It seems that protons block the passageway to the 8-ring cages and the 10-ring channels.

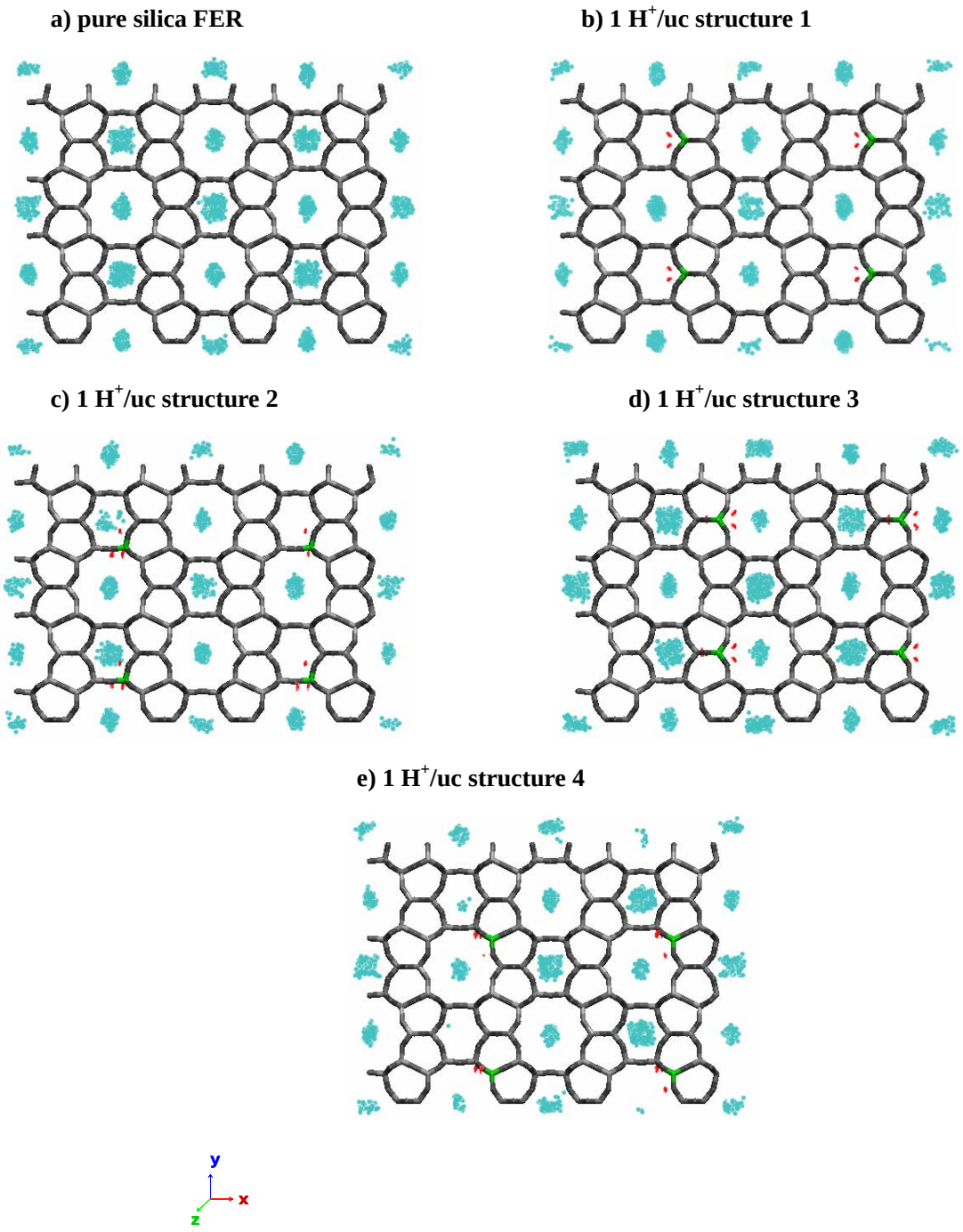

Figure 5.7: Distributions of butane and the non-framework protons in FER zeolites at 0.4 kPa and 333 K. The centers of mass of the butane molecules are represented by blue dots and the non-framework proton positions by red dots. The aluminum positions are indicated in green color.

The fractions of the adsorbed alkane molecules located in the FER 8-ring cages in structure 3 were calculated and the results are given in Figure 5.8 as a function of the loading. The results for pure silica structure are also shown for comparison.

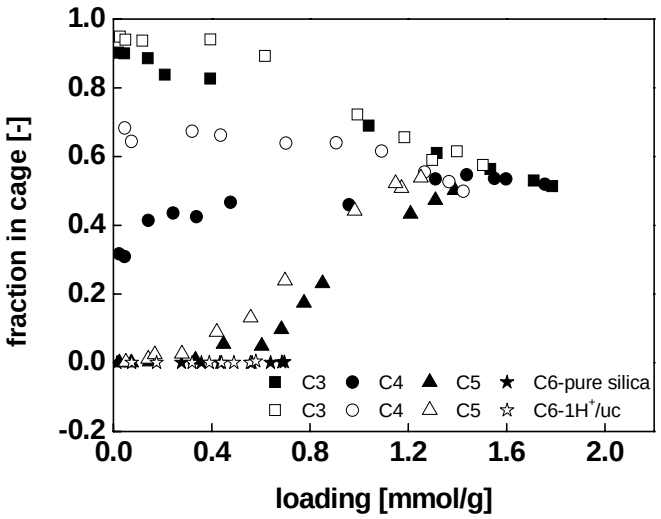

Figure 5.8: Fraction of the adsorbed alkane molecules located in the FER 8-ring cages as a function of loading at 333 K. The results for pure silica structure are represented by full symbols and the ones for H-FER are represented by open symbols.

Experimentally [17, 18], it is found that propane adsorbs preferentially in the 8-ring cage. The adsorption of pentane initially takes place only in the 10-ring channel and adsorption into the 8-ring cage occurs only at higher loadings. Hexane adsorbs only in the 10-ring channels and is excluded from the 8-ring cage. Our simulation results are consistent with the experimental observations. For butane, no preference is found by NMR measurements and our simulations predict that butane adsorption is preferred in the 10-ring channels for pure silica structure and in the 8-ring cage for H-FER structure. This can be explained by examining the snapshots of butane adsorption at low pressures. Figure 5.9 shows the sitting of butane in FER zeolites at 333 K and 0.05 kPa. For pure silica structure butane preferentially adsorbs in the 10-ring channels. Once we put any small amount inside the channels, they will start to repel *n*-alkanes attributed to the fact that the channel of FER-type zeolites is the smallest channel not to repel *n*-alkanes comparing with other zeolites [61]. When *n*-alkanes cannot reside in the 10-ring channel they will head for the 8-ring cage.

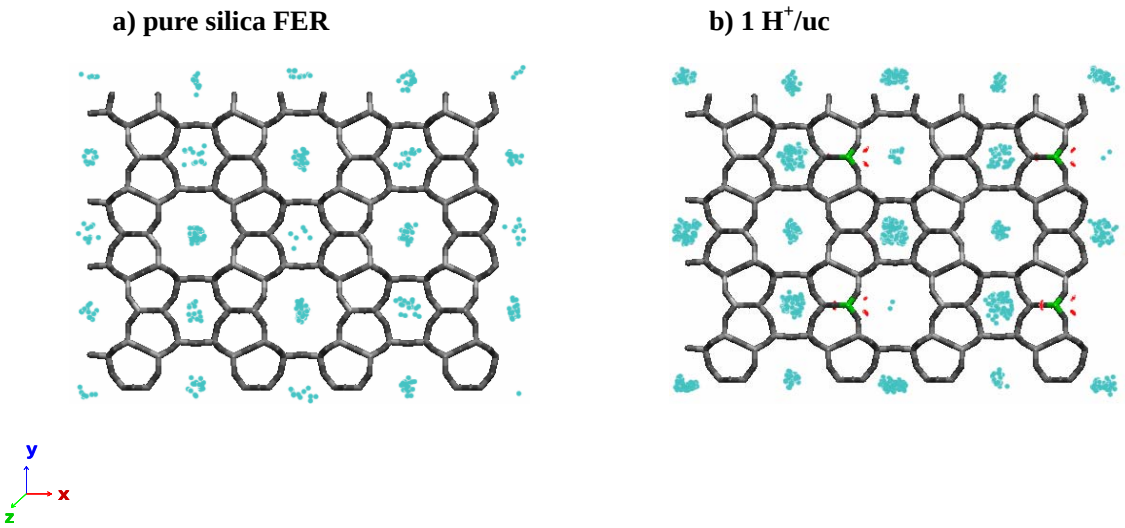

Figure 5.9: Distributions of butane and the non-framework protons in FER zeolites at 0.05 kPa and 333 K. The centers of mass of the butane molecules are represented by blue dots and the non-framework proton positions by red dots. The aluminum positions are indicated in green color.

Na-MOR zeolite

Another important zeolite considered in this work is Na-MOR. The adsorption isotherms and the Henry coefficients of methane in sixteen different structures were calculated and compared with available experimental data [26, 30]. Our results show that the agreement with experimental values is remarkable for the structure where Al atoms replace Si 4, 18, 31, 42, 80, 93, 105, and 115 [60]. In this structure the eight Al atoms are located in the 4-rings, in complete conformity with the suggested preferential sitting of aluminium provided by previous crystallographic, experimental, and theoretical work [43, 44, 62-65]. To study the effects of the cations on the adsorption behavior, we checked the snapshot of this structure with adsorbed methane at 323 K and 1 kPa, and compared with the adsorption in pure silica structure. The results are shown in Figure 5.10. For pure silica structure, the methane molecules are located almost homogeneously between the main channels and the side pockets. However, for the structure with cations, methane molecules were found adsorbed preferentially in the side pockets. Nearly half of the sodium cations were found to reside in the center of the 8-membered oxygen rings outside the main channels [66, 67]. This agrees with the available experimental data [68].

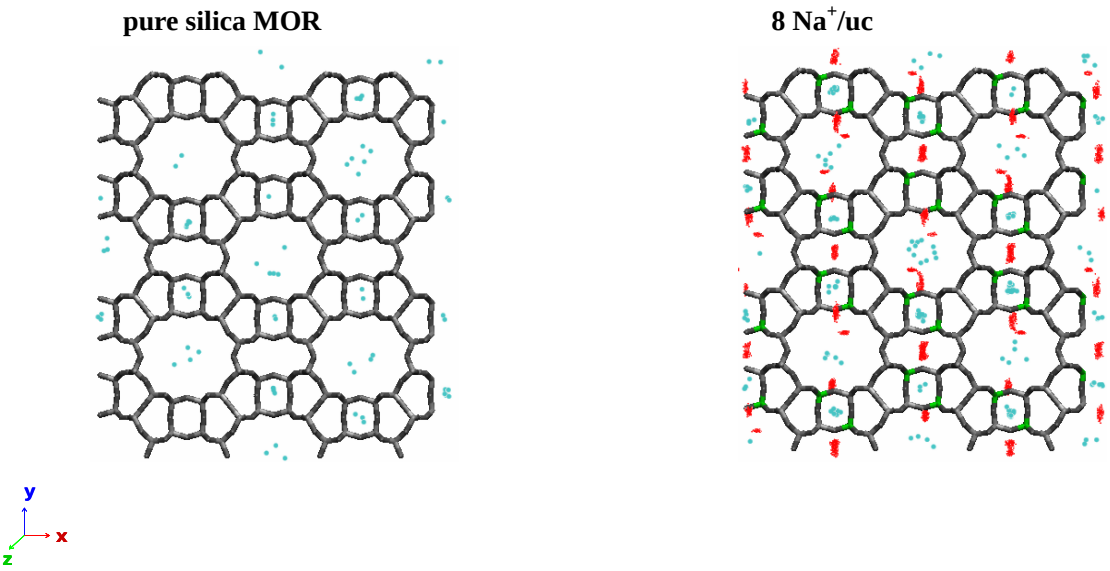

Figure 5.10: Distributions of methane and the non-framework sodium cations in MOR zeolites at 1 kPa and 323 K. The methane molecules are represented by blue dots and the non-framework Na^+ positions by red dots. The aluminum positions are indicated in green color.

Furthermore, the fraction of the adsorbed methane molecules located in the MOR main channels in the sodium and the pure silica structures was also calculated and the results are given in Figure 5.11 as a function of the loading.

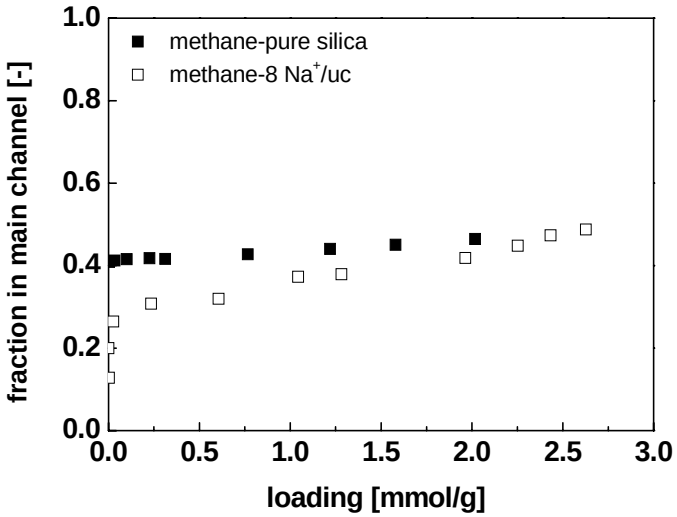

Figure 5.11: Fraction of the adsorbed methane located in the MOR main channels as a function of loading at 323 K. The results for pure silica structure are represented by full symbols and the ones for Na-MOR are represented by open symbols.

For pure silica structure, it is found that the side pockets are favored but not very strongly because the side pocket adsorption sites have a lower energy [26, 69] and the percentage is almost constant with the increasing of the loading. For Na-MOR structure, side pocket adsorption becomes more favorable because the Na cations residing at the opening of the side pockets make these sites more attractive [26]. These results are in complete conformity with the snapshots shown in Figure 5.10 and with all previous results [26, 69], but those obtained by Smit and den Ouden [40]. Smit and den Ouden predicted exclusion of methane from the side pockets in Na-MOR structure considering that the side pockets were effectively blocked by the Na^+ cations and unlike in our work, they fixed the Na^+ cations throughout their simulation.

Our simulation results show that by matching the simulation data with the available experimental values the most likely position of aluminium in zeolites could be identified. The aluminium position determines the cation distribution, and it is the presence and positions of the cations that can cause a difference in adsorption behavior. The Henry coefficients for FAU and LTA increase dramatically by the presence of cations, up to orders of magnitude for the longer chain lengths. As previously noted in literature, the effects of ions are three-fold [41, 42, 51]: a) ions provide additional adsorption sites, b) ions occupy pore volume, and c) ions can block accessible pockets and windows. FAU and LTA are examples of the first, while the second effect is reduced in these structures because ions are allowed to occupy pore volume (the sodalite cages) that is not accessible to the bulkier alkanes. This volume effect is important in zeolites formed by channels, like MFI and MOR, and at high pressures where loadings are close to saturation. MOR is also sensitive to the third effect, showing side pockets that can be blocked [41]. In some zeolites which have very different adsorption "regions" other complications can occur. Examples include MFI, which has straight channels, zig-zag channels, and intersections, and FER which has 10-ring channels and 8-ring side cages. Typically, for many adsorbates, this shows up as inflection in the adsorption isotherms [55, 70-72] and/or in Henry coefficients that do not show the typical monotonic increase over chain length (see Figure 5.2f). One of the main goals of this work is to find systematic trends in this and hopefully a classification or at least same criteria to estimate the influence of cations.

For the adsorption of alkanes we found that FAU, LTA, MEL, and MFI are insensitive to the aluminum distribution, while LTL, FER, TON, and MOR belong to the sensitive class. The insensitivity of the first group originates either from large, spherical cages with a high degree of symmetry (LTA and FAU), or from structures (MEL and MFI) that have preferred aluminium positions at different locations than the alkane adsorption sites. In MFI the preferred aluminium positions are in the big intersection while alkanes prefer the straight channels at low loadings. LTA and FAU show a higher difference with the pure siliceous

structure than MEL and MFI, mainly due to the larger amount of ions per volume present in these structures (see Figures 5.2a-5.2d). The increase per carbon number is the same for MEL and MFI, but for FAU and LTA we clearly find a change in slope. In cage-type zeolites multiple beads of the molecule have interaction with the ions. MFI and MEL have channels that tightly confine the alkanes and only the ends of the alkanes feel the ions resulting in a constant shift of the Henry coefficients as a function of carbon number. The zeolites of second group are channel systems and seem very sensitive to the positions of the aluminium, especially at low loadings. We suspect that MFI and MEL could be sensitive to other adsorbates than alkanes. This means that FAU and LTA (large cages with high degree of symmetry) are ideal to calibrate potential parameters (as we previously did [51, 73]), while almost all other structures are then suitable for the "reverse engineering" [60].

We are aware that our comparisons are subject to several uncertainties as well as to the experimental and simulation errors. However, in our opinion the approach itself remains valid and very attractive as simulations and experiments advances in time. We note that the fitting procedures with the set of structures which are insensitive to the aluminum distribution are based on the same kind of experimental data and procedures. Our potentials might therefore effectively already contain a certain level of experimental error, although these of course might vary from zeolite to zeolite, and sample to sample. However, it is the best we could do using currently available experimental data, and as soon as more experimental data becomes available we can further refine our approach.

5. 4 Conclusions

The simulation results provided a better physical understanding of the effects of the aluminium distributions on the adsorption properties of alkanes in zeolites at a microscopic level. This work shows that the aluminium distributions in zeolites strongly affect the positions and stability of ions, which in turn influence the adsorption behavior of alkanes. Therefore, the effect of aluminium on adsorption depends on the adsorbent, the ion, and the adsorbate type whether or not the adsorption is influenced. Furthermore, it should be possible, in the longer term, to use these data to more clearly delineate the relationships between the aluminium locations and the catalytic activities and selectivities of aluminosilicates.

Bibliography

[1] Krishna, R.; Smit, B.; Calero, S. *Chem. Soc. Rev.* **2002**, *31*, 185.

[2] Smit, B.; Krishna, R. *Chem. Eng. Sci.* **2003**, *58*, 557.

[3] Buttefey, S.; Boutin, A.; Mellot-Draznieks, C.; Fuchs, A. H. *J. Phys. Chem. B* **2001**, *105*, 9569.

[4] van Bokhoven, J. A.; Sambe, H.; Ramaker, D. E.; Koningsberger, D. C. *J. Phys. Chem. B* **1999**, *103*, 7557.

[5] van Bokhoven, J. A.; Koningsberger, D. C.; Kunkeler, P.; van Bekkum, H. *J. Catal.* **2002**, *211*, 540.

[6] Engelhardt, G.; Michel, D. *High resolution solid state NMR of silicates and zeolites*; John Wiley & Sons: New York, **1987**.

[7] Ehresmann, J. O.; Wang, W.; Herreros, B.; Luigi, D. P.; Venkatraman, T. N.; Song, W. G.; Nicholas, J. B.; Haw, J. F. *J. Am. Chem. Soc.* **2002**, *124*, 10868.

[8] Fyfe, C. A.; Thomas, J. M.; Klinowski, J.; Gobbi, G. C. *Angew. Chem.* **1983**, *95*, 257.

[9] Joyner, R. W.; Smith, A. D.; Stockenhuber, M.; van den Berg, M. W. E. *Phys. Chem. Chem. Phys.* **2004**, *6*, 5435.

[10] Denayer, J. F.; Souverijns, W; Jacobs, P. A.; Martens, J. A.; Baron, G. V. *J. Phys. Chem. B* **1998**, *102*, 4588.

[11] Denayer, J. F.; Baron, G. V.; Vanbutsele, G.; Jacobs, P. A.; Martens, J. A. *Chem. Eng. Sci.* **1999**, *54*, 3553.

[12] Savitz, S.; Siperstein, F.; Gorte, R. J.; Myers, A. L. *J. Phys. Chem. B* **1998**, *102*, 6865.

[13] Eder, F; Lercher, J. A. *J. Phys. Chem. B* **1997**, *101*, 1273.

[14] Pieterse, J. A. Z.; Veefkind-Reyes, S.; Seshan, K.; Lercher, J. A. *J. Phys. Chem. B* **2000**, *104*, 5715.

[15] Yang, L.; Trafford, K.; Kresnawahjuesa, O.; Sepa, J.; Gorte, R. J. *J. Phys. Chem. B* **2001**, *105*, 1935.

[16] Ocakoglu, R. A.; Denayer, J. F. M.; Marin, G. B.; Martens, J. A.; Baron, G. V. *J. Phys. Chem. B* **2003**, *107*, 398.

[17] van Well, W. J. M.; Cottin, X.; de Haan, J. W.; Smit, B.; Nivarthy, G.; Lercher, J. A.; van Hooff, J. H. C.; van Santen, R. A. *J. Phys. Chem. B* **1998**, *102*, 3945.

[18] van Well, W. J. M.; Cottin, X.; de Haan, J. W.; van Santen, R. A.; Smit, B. *Angew. Chem., Int. Ed.* **1998**, *37*, 1081.

[19] Satterfield, C. N.; Frabetti, A. J., Jr. *AIChE J.* **1967**, *13***,** 731.

[20] Choudhary, V. R.; Mayadevi, S.; Pai Singh, A. *J. Chem. Soc. Faraday Trans.* **1995**, *91*, 2935.

[21] Eberly, P. E., Jr. *J. Phys. Chem.* **1963**, *67*, 2404.

[22] Xu, Q.; Eguchi, T.; Nakayama, H.; Nakamura, N. *J. Chem. Soc. Faraday Trans.* **1995**, *91*, 2949.

[23] Xu, Q.; Eguchi, T.; Nakayama, H.; Nakamura, N. *J. Chem. Soc. Faraday Trans.* **1996**, *92*, 1039.

[24] Denayer, J. F.; Baron, G. V.; Martens, J. A. and Jacobs, P. A. *J. Phys. Chem. B* **1998**, *102*, 3077.

[25] Webster, C. E.; Cottone, A. III; Drago, R. S. *J. Am. Chem. Soc.* **1999**, *121*, 12127.

[26] Macedonia, M. D.; Moore, D. D.; Maginn, E. J. *Langmuir* **2000**, *16*, 3823.

[27] Yamazaki, T.; Hasegawa, K.; Honma Ken-ichi and Ozawa S. *Phys. Chem. Chem. Phys.* **2001**, *3*, 2686.

[28] Yuvaray, S.; Chang, T. H.; Yeh, C. T. *J. Phys. Chem. B* **2003**, *107*, 4971.

[29] Salla, I.; Montanari, T.; Salagre, P.; Cesteros, Y. and Busca G. *J. Phys. Chem. B* **2005**, *109*, 915.

[30] Delgado, J. A.; Uguina, M. A.; Gomez, J. M. *Stud. Surf. Sci. Catal.* **2005,** *158 A and B*, 1065.

[31] Maesen, T. L. M.; Schenk, M.; Vlugt, T. J. H.; de Jonge, J. P.; Smit, B. *J. Catal*. **1999**, *188*, 403.

[32] Schenk, M.; Smit, B.; Vlugt, T. J. H.; Maesen, T. L. M. *Angew. Chem., Int. Ed.* **2001**, *40*, 736.

[33] Domokos, L.; Lefferts, L.; Seshan, K.; Lercher, J. A. *J. Catal*. **2001**, *203*, 351.

[34] Raybaud, P.; Patrigeon, A.; Toulhoat, H. *J. Catal.* **2001**, *197*, 98.

[35] Lu, L.-H.; Wang, Q.; Liu, Y.-C., *Acta Chimica Sinica* **2003**, *61*, 1232.

[36] Ndjaka, J.-M. B.; Zwanenburg, G.; Smit, B.; Schenk, M. *Micropor. Mesopor. Mater.* **2004**, *68*, 37.

[37] van Well, W. J. M.; Cottin, X.; Smit, B.; van Hooff, J. H. C.; van Santen, R. A. *J. Phys. Chem. B* **1998**, *102*, 3952.

[38] Pascual, P.; Boutin, A. *Phys. Chem. Chem. Phys.* **2004**, *6***,** 2015.

[39] Pascual, P.; Boutin, A.; Ungerer, P.; Tavitian, B.; Fuchs, A. H. *Mol. Simulation* **2004**, *30*, 593.

[40] Smit, B.; den Ouden, C. J. J. *J. Phys. Chem.* **1988**, *92*, 7169.

[41] Beerdsen, E.; Smit, B.; Calero, S. *J. Phys. Chem. B* **2002**, *106*, 10659.

[42] Liu, B.; Smit, B. *Phys. Chem. Chem. Phys.* **2006,** *8*, 1852.

[43] Koranyi,T. I.; Nagy, J. B. *J. Phys. Chem. B* **2005**, *109*, 15791.

[44] Bodart, P.; Nagy, J. B.; Debras, G.; Gabelica, Z.; Jacobs, P. A. *J. Phys. Chem.* **1986**, *90*, 5183.

[45] Takaishi, T.; Kato, M.; Itabashi, K. *Zeolites* **1995**, *15*, 21.

[46] Peterson, B. K. *J. Phys. Chem. B* **1999**, *103*, 3145.

[47] Herrero, C. P.; Utrera, L.; Ramirez, R. *Phys. Rev. B* **1992**, *46*, 787.

[48] Vega, A. J. *J. Phys. Chem.* **1996**, *100*, 833.

[49] Ding, D. T.; Li, B. H.; Sun, P. C.; Jin, Q. H.; Wang, J. Z. *Zeolites* **1995**, *15*, 569.

[50] International Zeolite Association, Structure Commission, http://www.iza-structure.org.

[51] Calero, S.; Dubbeldam, D.; Krishna, R.; Smit, B.; Vlugt, T. J. H.; Denayer, J. F. M.; Martens, J.A.; Maesen, T. L. M. *J. Am. Chem. Soc.* **2004**, *126*, 11377.

[52] Maesen, T. L. M.; Schenk, M.; Vlugt, T. J. H.; Smit, B. *J. Catal*. **2001**, *203*, 281.

[53] Dubbeldam, D.; Beerdsen, E.; Vlugt, T. J. H.; Smit, B. *J. Chem. Phys.* **2005**, *122*, 224712.

[54] Vlugt, T. J. H.; Schenk, M. *J. Phys. Chem. B* **2002**, *106*, 12757.

[55] Dubbeldam, D.; Calero, S.; Vlugt, T. J. H.; Krishna, R.; Maesen, T. L. M.; Beerdsen, E.; Smit, B. *Phys. Rev. Lett.* **2004**, *93*, 088302.

[56] Dubbeldam, D.; Calero, S.; Vlugt, T. J. H.; Krishna, R.; Maesen, T. L. M.; Smit, B. *J. Phys. Chem. B* **2004**, *108*, 12301.

[57] Calero, S.; Lobato, M. D.; García-Pérez, E.; Mejías, J. A.; Lago, S.; Vlugt, T. J. H.; Maesen, T. L. M.; Smit, B.; Dubbeldam, D. *J. Phys. Chem. B* **2006**, *110*, 5838.

[58] Ryckaert, J.P.; Bellemans, A. *Faraday Discuss. Chem. Soc*. **1978**, *66*, 95.

[59] Frenkel, D.; Smit, B. *Understanding Molecular Simulations: From Algorithms to Applications*, 2nd ed.; Academic Press: San Diego, CA, **2002**.

[60] García-Pérez, E.; Dubbeldam, D.; Liu, B.; Smit, B.; Calero, S. *Angew. Chem., Int. Ed.* **2007**, *46*, 276.

[61] Maesen, T. L. M.; Beerdsen, E.;Calero, S.; Dubbeldam, D.; Smit, B. *J. Catal*. **2006**, *237*, 278.

[62] Schelenker, J. L.; Pluth, J. J.; Smith, J. V. *Materials Research Bulletin* **1968**, *13*, 169.

[63] Meier, W. M.; Gramlich, V. Z. *Kristallogr.* **1978**, *147*, 329.

[64] Derouane, E. G.; Fripiat, J. J. *Proceedings of the 6th International Zeolite Conference*,Reno, **1984,** p.717.

[65] Debras, G.; Nagy, J. B.; Gabelica, Z.; Bodart, P.; Jacobs, P. A. *Chem. Lett.* **1983**, 199.

[66] Maurin, G.; Senet, P.; Devautour, S.; Gaveau, P.; Henn, F.; van Doren, V. E.; Giuntini, J. C. *J. Phys. Chem. B*, **2001**, *105*, 9157.

[67] Maurin, G.; Bell, R. G.; Devautour, S.; Henn, F.; Giuntini, J. C. *J. Phys. Chem. B*, **2004**, *108*, 3739.

[68] Meier, W. M. Z. *Kristallogr.*, **1961**, *115*, 439.

[69] Nivarthi, S. S.; Van Tassel, P. R.; Davis, H. T.; McCormick, A. V. *J. Chem. Phys.* **1995**, *103*, 3029.

[70] Smit, B.; Maesen, T. L. M. *Nature*, **1995**, *374*, 42.

[71] Vlugt, T. J. H.; Zhu, W.; Kapteijn, F.; Moulijn, J. A.; Smit, B.; Krishna, R. *J. Am. Chem. Soc.* **1998**, *120*, 5599.

[72] Vlugt, T. J. H.; Krishna, R.; Smit, B. *J. Phys. Chem. B*, **1999**, *103*, 1102.

[73] García-Pérez, E.; Dubbeldam, D.; Maesen, T. L. M.; Calero, S. *J. Phys. Chem. B*, **2006**, *110*, 23968.

In this work a combined molecular dynamics simulation and dynamically corrected transition state theory (dcTST) study was performed to investigate the effect of interpenetration (catenation) on hydrogen diffusion in metal-organic frameworks (MOFs) as well as their relationship. The results on 10 isoreticular MOFs (IRMOFs) with and without interpenetration show that catenation can reduce hydrogen diffusivity by a factor of 2 to 3 at room temperature. For the interpenetrated IRMOFs with multi-pores of different sizes, free volume can serve as a measure for hydrogen diffusivity: the bigger the free volume, the larger the hydrogen diffusivity. In addition, the present work shows that dcTST can directly reveal the influence of the MOF structure on hydrogen diffusivity, which is a powerful tool to provide a better understanding of the relationship between gas diffusivity and MOF structure.

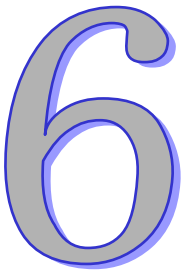

B. Liu, Q. Yang, C. Xue, C. Zhong, and B. Smit*

Molecular Simulation of Hydrogen Diffusion in Interpenetrated Metal-Organic Frameworks

6.1 Introduction

Metal-organic frameworks (MOFs) have been recognized as a new family of nanoporous materials that offer promising applications in gas storage, separation, and catalysis, etc. [1] Among the various MOFs synthesized, they can be divided into two groups: MOFs with non-interpenetrated frameworks [2] and those with interpenetrated ones [3]. Apart from substantial experimental studies on the gas adsorption and diffusion in non-interpenetrated MOFs [4], there are also many theoretical studies reported in the literature [5]. For example, Frost et al. investigated the influencing factors on the hydrogen uptake in IRMOFs using grand canonical Monte Carlo (GCMC) simulations [6] and Ramsahye et al. studied the breathing effect of the MIL-53 and -47 frameworks on CO_2 adsorption [7]; the hydrogen adsorption sites in Zn-MOFs were clarified by both quantum chemical [8] and classical simulation studies [9]. In addition, Skoulidas et al. investigated the self- and transport diffusion of several light gases in MOFs in detail using the molecular dynamics method [10]. Framework flexibility effects on gas adsorption and diffusion in Zn-MOF were investigated by several groups [11, 12]. There are much less investigations published on interpenetrated MOFs. Several available investigations have indicated that interpenetration (catenation) can enhance the adsorption capacity of MOFs [13], attributed to the additional adsorption sites and small pores formed by

* Liu, B.; Yang, Q.; Xue, C.; Zhong, C.; Smit, B. *Phys. Chem. Chem. Phys.* **2008**, *10*, 3244.

interpenetration that can strengthen the overall interaction between gas molecules and the pore walls [14]. Despite the potential applications of interpenetrated MOFs to gas storage and separation, little is known on gas diffusion characteristics in such MOFs. To the best of our knowledge, neither experimental nor theoretical investigations have been performed on this topic, thus this work carried out a combined molecular dynamics simulation and dynamically corrected transition state theory (dcTST) study to investigate the effect of catenation on gas diffusion. Considering that MOFs are a family of promising materials for hydrogen storage, hydrogen was selected as the probe molecule. Therefore, this work also provides useful information for developing new MOFs as efficient hydrogen storage materials.

6.2 Models and computational method

6.2.1 MOF structures

In this work, ten isoreticular metal-organic frameworks (IRMOFs) as synthesized by Eddaoudi et al. [15] were adopted as representatives of MOFs. The guest-free framework structures of the IRMOFs were constructed from their corresponding experimental single-crystal X-ray diffraction (XRD) data [15] using Materials Studio Visualizer [16]. As can be seen from Figure 6.1, IRMOFs-1, 8, 10, 12, 14, and 16 feature the same primitive cubic topology with the octahedral $Zn_4O(CO_2)$ clusters linked by different organic dicarboxylate linkers, while IRMOFs-9, 11, 13, and 15 are the interpenetration counterparts of IRMOFs-10, 12, 14, and 16, respectively. The structural properties for these IRMOF materials are given in Table 6.1, where the free volumes were calculated using a probe size of 0.0 Å to determine the total free volume not occupied by the framework atoms.

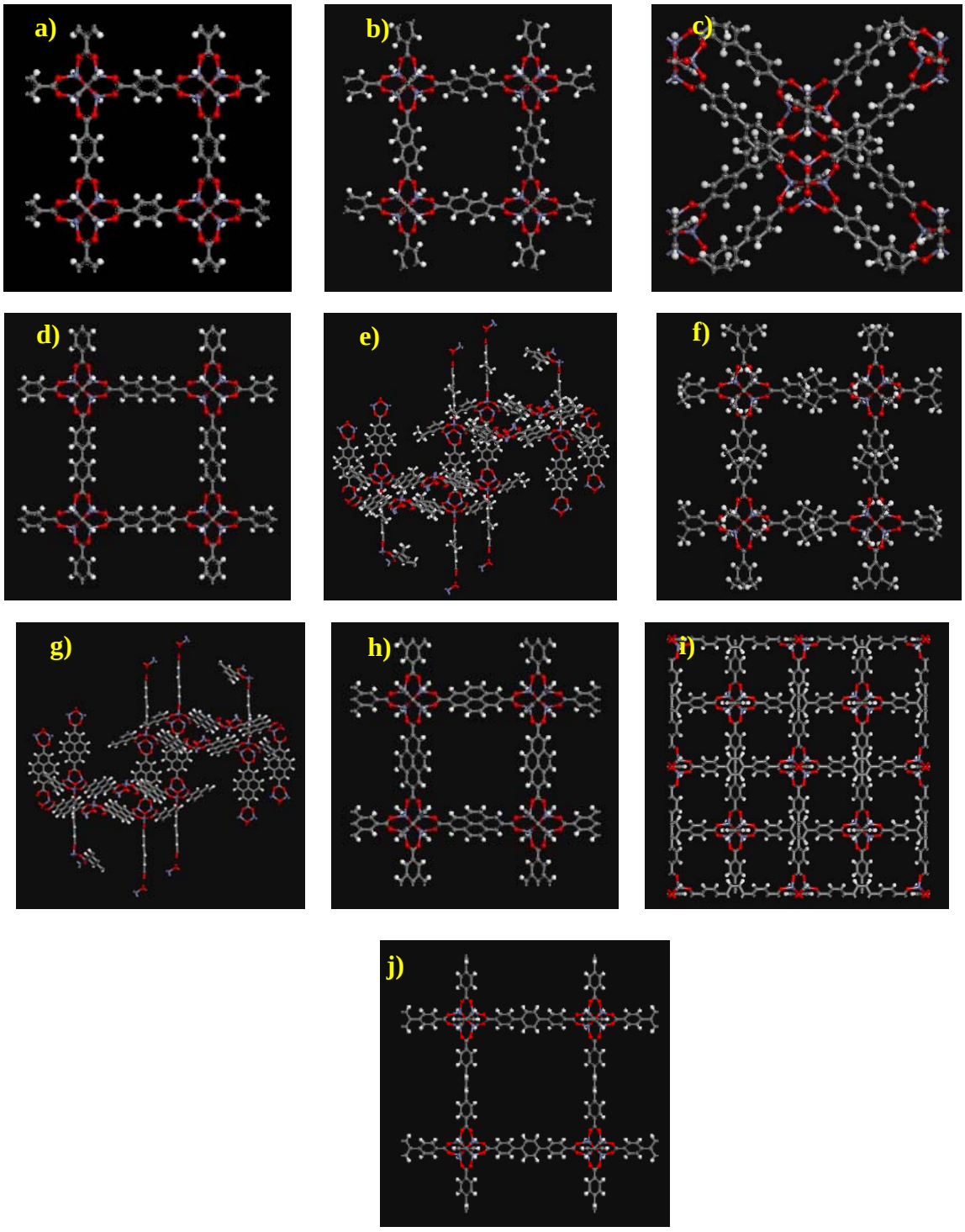

Figure 6.1: Unit cell crystal structures of the IRMOFs used in the simulation: a) IRMOF-1, b) IRMOF-8, c) IRMOF-9, d) IRMOF-10, e) IRMOF-11, f) IRMOF-12, g) IRMOF-13, h) IRMOF-14, i) IRMOF-15, j) IRMOF-16 (Zn, blue; O, red; C, gray, and H, white).

Material	Pore shape[a]	Unit cell (Å)	Cell angle (Degree)	d_{pore} [a] (Å)	ρ_{crys} [a] (g/cm^3)	V_{free} [b] (cm^3/g)	Porosity [b] (%)
IRMOF-1	cubic	a=b=c=25.832	α=β=γ=90	10.9/14.3	0.59	1.36	80.5
IRMOF-8	cubic	a=b=c=30.092	α=β=γ=90	12.5/17.1	0.45	1.87	84.0
IRMOF-10	cubic	a=b=c=34.281	α=β=γ=90	16.7/20.2	0.33	2.66	87.9
IRMOF-12	cubic	a= b=c=34.281	α=β=γ=90	13.9/20.0	0.38	2.24	85.1
IRMOF-14	cubic	a=b=c=34.381	α=β=γ=90	14.7/20.1	0.37	2.30	86.3
IRMOF-16	cubic	a=b=c=42.980 [c]	α=β=γ=90	23.3	0.21	4.46	91.5
IRMOF-9	cubic/catenation	a=17.147, b=23.322 c=25.255	α=β=γ=90	4.5/6.3/8.1/ 10.7	0.66	1.14	74.8
IRMOF-11	cubic/catenation	a=b=24.822, c=56.734	α=β=90, γ=120	3.5/3.8/4.7/ 6.1/7.3/11.1	0.76	0.92	69.8
IRMOF-13	cubic/catenation	a=b=24.822, c=56.734	α=β=90, γ=120	4.2/4.7/6.1/ 7.0/11.4	0.75	0.95	71.4
IRMOF-15	cubic/catenation	a=b=c=42.918 [c]	α=β=γ=90	–	0.41	2.01	82.8

Table 6.1: Structural properties for the IRMOFs studied in this work.

a Obtained from the XRD crystal data.[15]
b Calculated with the Materials Studio package.
c Unit cell used in the simulation.

6.2.2 Force fields and the parameters

Force field plays an important role in molecular simulations. In this work, the Coulombic interactions were not considered in our simulations as they were demonstrated to have little effect on the hydrogen adsorption properties at room temperature [17]. H_2 was modeled as a rigid diatomic molecule with bond length of 0.74 Å. Each atom H in H_2 molecule was represented as a Lennard-Jones (LJ) interaction site, for which the LJ potential parameters were taken from the force field developed in our previous work [18], and listed in Table 6.2. These potential parameters were optimized to reproduce the experimental PVT curve of bulk hydrogen [19], and could describe the experimental self-diffusion coefficients of bulk hydrogen well [18]. In addition, this force field has also been successfully used to simulate the adsorption of H_2 in MOFs by other researchers [20].

For the IRMOFs studied here, an atomistic representation was used to model all of these IRMOFs. The same potential model, that is, the site-site LJ potential was also used to calculate the interactions between adsorbate molecules and the atoms in the frameworks of adsorbents. The potential parameters listed in Table 6.2 were taken from the universal force field (UFF) of Rappe et al. [21], which has been successfully employed to depict the

adsorption [17, 22], diffusion [10,23], and separation [24] of several light gases and their mixtures in MOFs. In our simulations, all the LJ cross interaction parameters were determined using the Lorentz-Berthelot mixing rules.

LJ Parameters	H_2_H	MOF_O	MOF_C	MOF_H	MOF_Zn
σ (Å)	2.72	3.12	3.43	2.57	2.46
ε / k_B (K)	10.00	30.19	52.84	22.14	62.40

Table 6.2: LJ potential parameters for H_2 and the IRMOFs used in this work.

6.2.3 Molecular Dynamics simulation

In this work, equilibrium molecular dynamics (MD) simulations were carried out in the canonical (NVT) ensemble to investigate the effects of pore size and catenation on the diffusion behavior of H_2 in MOFs. The MD simulations were performed at room temperature, and the Nosé-Hoover chain (NHC) thermostat as formulated by Martyna et al. [25] was used to maintain the constant temperature condition. Similar to previous works [5, 6, 9-12], all the IRMOFs studied in this work were treated as rigid with atoms frozen at their crystallographic positions during simulations. Although the diffusion properties of guest molecules may depend significantly on the lattice dynamics of MOFs [12], the interactions between H_2 molecules and the frameworks of MOFs are weak and our purpose is to perform a comparative study on IRMOFs with and without catenation, thus, the treatment of rigid MOFs is reasonable. The simulation cell consists of 2×2×2 to 4×4×4 elementary cells of the IRMOF crystal lattice to ensure at least fifty H_2 molecules are accommodated in the cell, and the structural model for a unit cell of each IRMOF was constructed using the experimental XRD data as shown in Figure 6.1. The velocity Verlet algorithm was used to integrate Newton's equations of motion. The time step used in the MD simulations was taken as 1.0 fs. All the LJ interactions were calculated using the cut and shifted potential with a 17.0 Å cutoff radius, and periodic boundary conditions were applied in all three dimensions. Simulations were performed as follows: molecules were randomly inserted into the IRMOF lattices, and then relaxed using approximately 100 000 NVT Monte Carlo moves. Following the relaxation, velocities from the Maxwell-Boltzmann distribution at the required temperature were assigned to all the adsorbate molecules, and the total momentum of the system was set to zero. Next, the system was allowed to equilibrate with 100 000 MD steps before the final simulations were run for 2000 000 MD steps to sample the diffusion properties. At least 10 independent simulations were performed for each loading to estimate the statistical error. During each simulation, the trajectory of the system was saved every 100 steps to subsequently calculate the self-diffusion coefficient *D*s by mean-square displacements (MSD) method using a so-called order-N algorithm [26]. It was checked that MD simulations conducted in microcanonical (NVE) ensemble gave the equivalent results. To increase the computational efficiency, the potential

energies and forces between the adsorbate and adsorbent were initially tabulated on a series of three-dimensional grid points with grid spacing 0.15 Å. During the simulations, the potential energy and force at any position in the adsorbent were determined by interpolation [23].

6.2.4 Dynamically corrected Transition State Theory

Dynamically corrected Transition State Theory (dcTST) [27] regards diffusion processes in confinement as hopping events on a lattice, where the hopping from state A to another state B is limited by a free energy barrier between the two states. A and B are separated by a lattice distance λ. Together with the dynamical correction factor κ, free energy profiles $F(q)$ can be used to compute a hopping rate $k_{A\to B}$ between states A and B by:

$$k_{A\to B} = \kappa \times \sqrt{\frac{k_B T}{2\pi m}} \times \frac{\exp[-\beta F(q^*)]}{\int_{pore} \exp[-\beta F(q)]dq} \tag{6.1}$$

where k_B is Boltzmann's constant, T is the temperature of the system, m is the mass of the hopping particle, and q^* denotes the (assumed) location of the barrier. This hopping rate $k_{A\to B}$ in turn can be converted to a self-diffusion coefficient D_s via:

$$D_s = k_{A\to B} \times \lambda^2 = \kappa \times \sqrt{\frac{k_B T}{2\pi m}} \times \frac{\exp[-\beta F(q^*)]}{\int_{pore} \exp[-\beta F(q)]dq} \times \lambda^2 = \kappa \times D_s^{TST} \tag{6.2}$$

In the above equation, D_s^{TST} is the free energy contribution to the self-diffusion coefficient, the part of the diffusion that is governed by free energy barriers: influences of the confinement topology on the diffusion of the gas molecules. κ is regarded as a measure for the interaction between the fluid particles themselves [28].

To compute free energy profiles, we performed NVT ensemble Monte Carlo simulations using the histogram sampling (HS) method [27]. In the HS method, a histogram is made of the particle positions, mapped on the reaction coordinate q. Then this histogram can be converted into a free energy profile by using $\beta F(q) = -\ln < P(q) >$, where $P(q)$ denotes the probability to find a molecule at a given position q according to the histogram. Details of the calculations can be found elsewhere [29].

6.3 Results and discussion

6.3.1 Effect of catenation on hydrogen diffusivity in MOFs

To understand how the pore size and interpenetration (catenation) affect the hydrogen diffusion behaviors, the self-diffusivities (D_s) of hydrogen in the ten selected IRMOFs at room temperature were examined with MD simulation. The simulation results are shown in Figure 6.2, as a function of hydrogen loading.

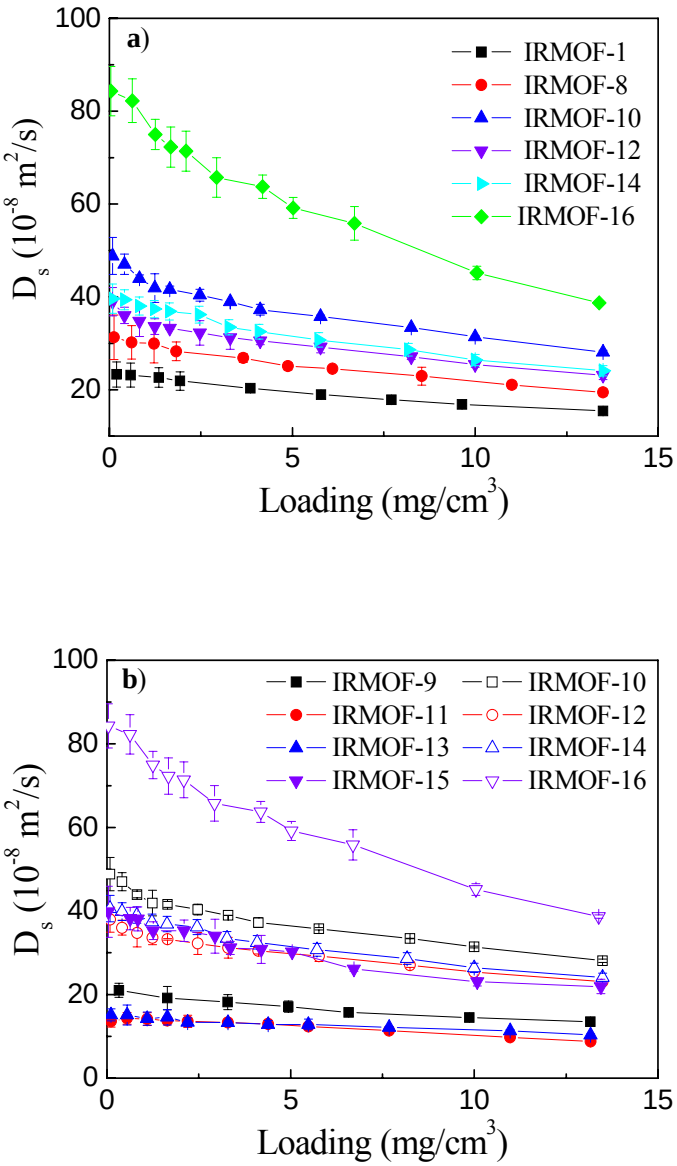

Figure 6.2: a) Comparison of the self-diffusivities of hydrogen in IRMOFs with the same primitive cubic topology at room temperature, b) Effect of catenation on the self-diffusivities of hydrogen in the IRMOFs at room temperature.

Figure 6.2a shows that for the six non-interpenetrated IRMOF materials with the same primitive cubic topology and loading, the self-diffusivities of hydrogen have the following order: IRMOF-16 > IRMOF-10 > IRMOF-14 (or IRMOF-12) > IRMOF-8 > IRMOF-1, which is consistent with the gradually decreasing sequence of pore size of the IRMOF materials. In Figure 6.2a, it seems the dependency of hydrogen diffusivity in IRMOF-16 is more evident than that in the other five IRMOFs, this can be explained as follows: (1) the porosity of IRMOF-16 (Table 6.1) is larger than the other five IRMOFs, thus, at the same loading

(mg/total volume of material) the hydrogen density in IRMOF-16 is smaller than that in the other materials, and (2), moreover, the pore size of
IRMOF-16 is much larger than that of the other five IRMOFs, leading to a much larger hydrogen diffusivity at the same loading.

Figure 6.2b shows the effect of catenation on the self-diffusivities of hydrogen in the IRMOFs at room temperature. The hydrogen self-diffusivities in the IRMOFs (IRMOF-10, IRMOF-12, IRMOF-14, and IRMOF-16) without catenation are two to three times of that in their catenated counterparts (IRMOF-9, IRMOF-11, IRMOF-13, and IRMOF-15, respectively). This implies that the motion of hydrogen molecules in MOFs is restricted largely by their catenation structures. In the interpenetrated IRMOFs, there are various pores with different sizes (4 in IRMOF-9 and 6 in IRMOF-11), and thus it is difficult, if not impossible, to correlate hydrogen diffusivity to pore size. However, an examination of the free volume of each material and the hydrogen diffusivity values shows that there is a good correlation between them: the larger the free volume, the bigger the hydrogen diffusivity. To illustrate this more intuitionally, the self-diffusivities of hydrogen at infinite dilution loading were plotted against the free volumes of the interpenetrated IRMOF materials as well as those without catenation. The results presented in Figure 6.3 show that a good correlation does exist between them. A similar relationship also holds for other hydrogen loadings. This suggests that for the interpenetrated IRMOFs with multi-pores of different sizes, material free volume can serve as a measure of hydrogen diffusivity.

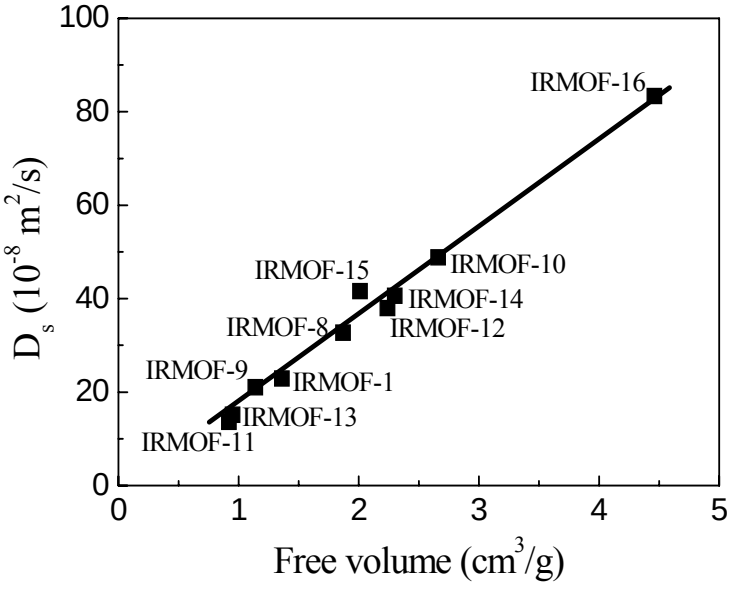

Figure 6.3: Self-diffusivities of hydrogen at infinite dilution loading vs free volume of the IRMOFs.

To understand the sitting of hydrogen molecules in the studied MOFs, center of mass (COM) probability distributions of hydrogen in IRMOF-10 and in its catenated counterpart, IRMOF-9, at the loading of 10 molecules per unit cell and room temperature were calculated,

and the results are shown in Figure 6.4. In IRMOF-10 hydrogen molecules distribute nearly evenly in the metal cluster and linker region, with slight accumulation near the cluster area; in IRMOF-9, the situation is a little different as the largest accumulation occurs in the catenated area formed by the metal clusters. This confirms that catenation can improve gas affinity at room temperature.

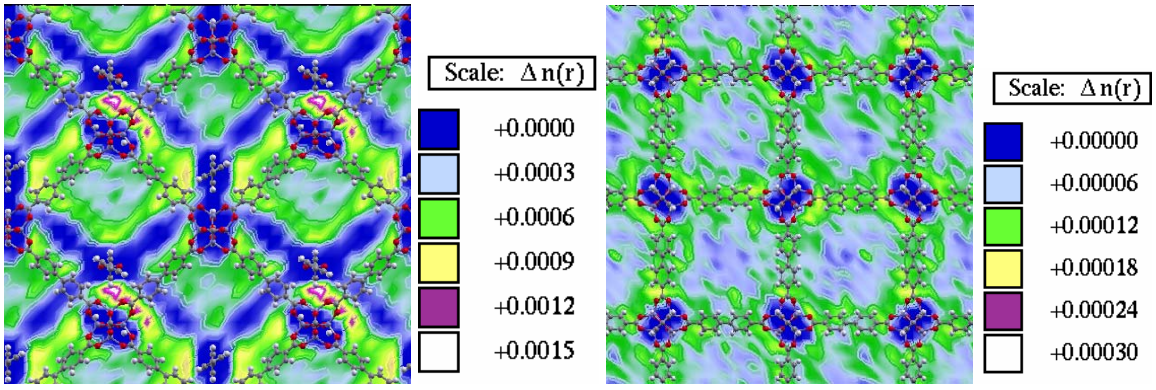

IRMOF-9 IRMOF-10

Figure 6.4: Contour plots of COM probability density in planes a) through the catenated area in IRMOF-9 and b) through the Zn_4O clusters in IRMOF-10 (Zn, blue; O, red; C, gray, and H, white).

6.3.2 The relationship between hydrogen diffusivity and MOF structure by dcTST

To further understand the relationship between hydrogen diffusivity and the MOF structure, a dynamically corrected transition state theory [27-29] study was performed for IRMOF-16 and its catenation counterpart, IRMOF-15, at room temperature and infinite dilution. The diffusion at infinite dilution can usually be fully accounted for by D_s^{TST} , i.e., the free energy contribution to the self-diffusion, as the dynamical correction factor κ is the contribution to the diffusion of interparticle collisions [28]. The free energy profiles in IRMOF-15 and -16 are shown in Figure 6.5. The reaction coordinate q is simply the position of a tagged molecule along the Cartesian connection from one pore to another. Because the structures of IRMOF-15 and -16 are highly symmetric, we only show the free energy profiles along the z-direction. The wells of the barriers correspond to the locations near the metal cluster and linker region inside the pores, i.e., the energetically favorable adsorption sites, and the maxima to the locations of the metal cluster and linker region. Clearly, the number of barriers per unit cell in IRMOF-15 is larger than those in IRMOF-16, attributed to the catenation structure of the former. From our MD simulations we know that hydrogen diffusivity in IRMOF-15 is about half of that in IRMOF-16 (39.8 [10^{-8} m^2/s] and 84.3[10^{-8} m^2/s] respectively) at infinite dilution, this can be explained by comparing the D_s^{TST} for the two materials from dcTST. According to Eq. (6.2),

the D_s^{TST} is given as $D_s^{TST} = \sqrt{\frac{k_B T}{2\pi m}} \times \frac{\exp[-\beta F(q^*)]}{\int_{pore} \exp[-\beta F(q)]dq} \times \lambda^2$. The values of $\sqrt{\frac{k_B T}{2\pi m}} \times \exp[-\beta F(q^*)]$ are nearly identical for IRMOF-15 and IRMOF-16 since the barrier heights are nearly same for the two materials. On the other hand, $[\int_{pore} \exp[-\beta F(q)]dq]_{\text{IRMOF-15}}$ $\approx 0.5\,[\int_{pore} \exp[-\beta F(q)]dq]_{\text{IRMOF-16}}$ and $\lambda_{\text{IRMOF-15}}$ (the lattice distance between two adjacent pore centers) = $0.5\,\lambda_{\text{IRMOF-16}}$. Therefore, the dcTST gives results that are consistent with the MD simulations. The structural effects can be revealed clearer by the dcTST: catenation in IRMOF-15 leads to a decrease of λ, i.e., at a given length the number of barriers is increased, resulting in a smaller hydrogen diffusivity in IRMOF-15 than that in IRMOF-16.

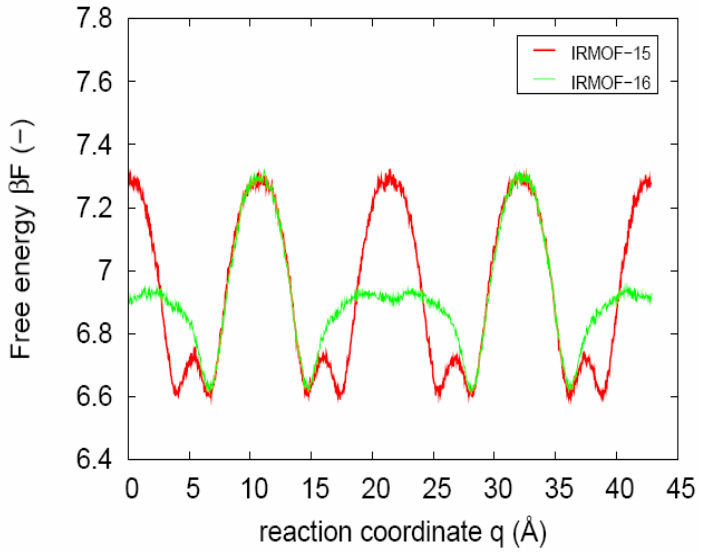

Figure 6.5: Free energy profiles F(q) of hydrogen in IRMOF-15 and IRMOF-16 at room temperature and infinite dilution. The reaction coordinate is chosen along the z direction. For IRMOF-15 the pore centers are located at 5.36, 16.09, 26.82, and 42.92 Å, while for IRMOF-16 the pore centers are located at 0, 21.49, and 42.98 Å, respectively.

6.4 Conclusions

We find that free volume plays the main role on determining hydrogen diffusivity in MOFs at room temperature, and for interpenetrated MOFs with multi-pores of different sizes, free

volume can serve as a measure for hydrogen diffusivity. The results on the ten IRMOFs show that catenation can reduce hydrogen diffusivity by a factor of 2 to 3 at room temperature, attributed mainly to the increase of the number of barriers at a given space. In addition, the present work shows that dcTST can characterize the number and value of diffusion barriers in MOFs to relate hydrogen diffusivity directly to the structure of a MOF material, giving a better understanding of guest molecule diffusivity in MOFs.

Bibliography

1 J. L. C. Rowsell and O. M. Yaghi, *Angew. Chem. Int. Ed*., 2005, **44**, 4670-4679; R. Q. Snurr, J. T. Hupp and S. T. Nguyen, *AIChE J.*, 2004, **50**, 1090-1095; U. Mueller, M. Schubert, F. Teich, H. Puetter, K. Schierle-Arndt, and J. Pastre, *J. Mater. Chem.*, 2006, **16**, 626–636.

2 Y. Kubota, M. Takata, R. Matsuda, R. Kitaura, S. Kitagawa, K. Kato, M. Sakata and T. C. Kobayashi, *Angew. Chem. Int. Ed.*, 2005, **44**, 920-923; S. S. Kayes and J. R. Long, *J. Am. Chem. Soc.***,** 2008, **130**, 806-807.

3 B. Kesanli, Y. Cui, M. R. Smith, E. W. Bittner, B. C. Bockrath and W. Lin, *Angew. Chem. Int. Ed.*, 2005, **44**, 72-75; B. Chen, S. Ma, E. J. Hurtado, E. B. Lobkovsky and H. C. Zhou, *Inorg. Chem.*, 2007, **46**, 8490-8492.

4 M. Latroche, S. Surblé, C. Serre, C. Mellot-Draznieks, P. L. Llewellyn, J. H. Lee, J. S. Chang, S. H. Jhung and G. Férey, *Angew. Chem. Int. Ed*., 2006, **45**, 8227-8231; A. G. Wong-Foy, A. J. Matzger and O. M. Yaghi, *J. Am. Chem. Soc.*, 2006, **128**, 3494-3495; S. S. Kaye, A. Dailly, O. M. Yaghi and J. R. Long, *J. Am. Chem. Soc.*, 2007, **129**, 14176-14177.

5 J. L. Belof, A. C. Stern, M. Eddaoudi and B. Space, *J. Am. Chem. Soc.*, 2007, **129**, 15202-15210; K. S. Walton, A. R. Millward, D. Dubbeldam, H. Frost, J. J. Low, O. M. Yaghi and R. Q. Snurr, *J. Am. Chem. Soc.*, 2008, **130**, 406-407; Q. Yang, C. Xue, C. Zhong and J. Chen, *AIChE J.*, 2007, **53**, 2832-2840.

6 H. Frost, T. Düren and R. Q. Snurr, *J. Phys. Chem. B*, 2006, **110**, 9565-9570.

7 N. A. Ramsahye, G. Maurin, S. Bourrelly, P. Llewellyn, T. Loiseau and G. Férey, *Phys. Chem. Chem. Phys.*, 2007, **9**, 1059–1063; N. A. Ramsahye, G. Maurin, S. Bourrelly, P. L. Llewellyn, T. Loiseau, C. Serrec and G. Férey, *Chem. Commun.*, 2007, 3261-3263.

8 E. Klontzas, A. Mavrandonakis, G. E Froudakis, Y. Carissan| and W. Klopper, *J. Phys. Chem. C*, 2007, **111**, 13635-13640; Q. Yang and C. Zhong, *J. Phys. Chem. B*, 2006, **110**, 655-658; T. B. Lee, D. Kim, D. H. Jung, S. B. Choi, J. H. Yoon, J. Kim, K. Choi and S. H. Choi, *Catal. Today*, 2007, **120**, 330-335;

9 S. S. Han, W. Q. Deng and W. A. Goddard III, *Angew. Chem. Int. Ed.*, 2007, **46**, 6289-6292; D. Dubbeldam, H. Frost, K. S. Walton and R. Q. Snurr, *Fluid Phase Equilibr.*, 2007, **261**, 152-161.

10 A. I. Skoulidas and D. S. Sholl, *J. Phys. Chem. B*, 2005, **109**, 15760-15768.

11 J. A. Greathouse and M. D. Allendorf, *J. Am. Chem. Soc.*, 2006, **128**, 10678-10679; D. Dubbeldam, K. S. Walton, D. E. Ellis and R.Q. Snurr, *Angew. Chem. Int. Ed.*, 2007, **46**, 4496-4499.

12 S. Amirjalayer, M. Tafipolsky and R. Schmid, *Angew. Chem. Int. Ed.* 2007, **46**, 463-466.

13 J. L. C. Rowsell and O. M. Yaghi, *J. Am. Chem. Soc.*, 2006, **128**, 1304-1315; D. H. Jung, D. Kim, T. B. Lee, S. B. Choi, J. H. Yoon, J. Kim, K. Choi and S. H. Choi, *J. Phys. Chem. B*, 2006, **110**, 22987-22990; B. Chen, S. Ma, F. Zapata, E. B. Lobkovsky and J. Yang, *Inorg. Chem.*, 2006, **45**, 5718-5720.

14 S. Ma, D. Sun, M. Ambrogio, J. A. Fillinger, S. Parkin and H. C. Zhou, *J. Am. Chem. Soc.*, 2007, **129**, 1858-1859.

15 M. Eddaoudi, J. Kim, N. Rosi, D. Vodak, J. Wachter, M. O'Keeffe and O. M. Yaghi, *Science*, 2002, **295**, 469-472.

16 Accelrys, Inc., Materials Studio, 3.0 V; Accelrys Inc: San Diego, CA, 2003.

17 G. Garberoglio, A. I. Skoulidas and J. K. Johnson, *J. Phys. Chem. B*, 2005, **109**, 13094-13103.

18 Q. Yang and C. Zhong, *J. Phys. Chem. B*, 2005, **109**, 11862-11864.

19 N. B. Vargaftik, *Tables of Thermophysical Properties of Liquids and Gases*, John Wiley & Sons: New York, 1975.

20 S. Surblé, F. Millange, C. Serre, T. Düren, M. Latroche, S. Bourrelly, P. L. Llewellyn and G. Férey, *J. Am. Chem. Soc.*, 2006, **128**, 14889-14896.

21 A. K. Rappé, C. J. Casewit, K. S. Colwell, W. A. Goddard III and W. M. Skiff, *J. Am. Chem. Soc.*, 1992, **114**, 10024-10035.

22 V. Krungleviciute, K. Lask, L. Heroux, A. D. Migone, J.-Y. Lee, J. Li and A. Skoulidas, *Langmuir*, 2007, **23**, 3106-3109.

23 A. I. Skoulidas, *J. Am. Chem. Soc.* 2004, **126**, 1356-1357.

24 S. Keskin and D. S. Sholl, *J. Phys. Chem. C*, 2007, **111**, 14055-14059; R. Babarao, Z. Hu, J. Jiang, S. Chempath and S. I. Sandler, *Langmuir*, 2007, **23**, 659-666.

25 G. Martyna, M. E. Tuckerman, D. J. Tobias and M. L. Klein, *Mol. Phys.*, 1996, **87**, 1117-1157.

26 D. Frenkel and B. Smit, *Understanding Molecular Simulation*: *From Algorithms to Applications*; Academic Press: San Diego, 2002.

27 E. Beerdsen, B. Smit and D. Dubbeldam, *Phys. Rev. Lett.*, 2004, **93**, 248301; E. Beerdsen, D. Dubbeldam and B. Smit, *Phys. Rev. Lett.*, 2005, **95**, 164505; E. Beerdsen, D. Dubbeldam and B. Smit, *Phys. Rev. Lett.*, 2006, **96**, 044501.

28 E. Beerdsen, D. Dubbeldam and B. Smit, *J. Phys. Chem. B*, 2006, **110**, 22754-22772.

29 D. Dubbeldam, E. Beerdsen, T. J. H. Vlugt and B. Smit, *J. Chem. Phys.*, 2005, **122**, 224712.

In this work a systematic molecular simulation study was performed to study the effect of interpenetration on gas mixture separation in metal-organic frameworks (MOFs). To do this, three pairs of isoreticular MOFs (IRMOFs) with and without interpenetration were adopted to compare their adsorption separation selectivity for CH_4/H_2 mixtures at room temperature. The results show that methane selectivity is greatly enhanced in the interpenetrated IRMOFs compared with their non-interpenetrated counterparts, due to the formation of additional small pores and adsorption sites by the interpenetration of frameworks. Furthermore, this work shows methane selectivity behavior is more complex in the interpenetrated IRMOFs and selectivity differs largely in the different areas of the pores, attributed to the existence of various small pores of different sizes. In addition, the present work shows that the ideal adsorbed solution theory is likely to be applicable to interpenetrated MOFs with complex structures.

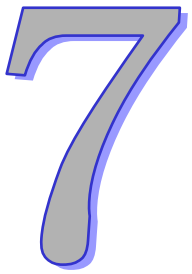

B. Liu, Q. Yang, C. Xue, C. Zhong, B. Chen, and B. Smit*

Enhanced Adsorption Selectivity of Hydrogen and Methane Mixtures in Metal-Organic Frameworks with Interpenetration

7.1 Introduction

Metal-organic frameworks (MOFs) are a family of hybrid porous materials that are formed by the coordination of metal ions with organic linkers. These materials feature opportunities for functionality and structure by a rational combination of different metal ions with different organic linkers. To date a large number of different MOFs have been synthesized with various promising applications in, for example, gas storage, separation, or catalysis, etc.[1-3] According to the structural characteristics, they can be categorized into two types: those with non-interpenetrated frameworks [4, 5] and those with interpenetrated ones [6, 7]. In the latter additional small pores and adsorption sites are formed by the interpenetration of frameworks, leading to MOFs with multi-pores of different sizes that may exhibit enhanced gas adsorption and separation properties [7-13].

* Liu, B.; Yang, Q.; Xue, C.; Zhong, C.; Chen, B.; Smit, B. *J. Phys. Chem. C* **2008**, *112*, 9854.

Currently, most theoretical [14-23] and experimental [24-26] investigations focus on non-interpenetrated MOFs and far less attention has been paid to these interpenetrated structures. Extensive studies have been carried out on the adsorption and diffusion of pure gases in MOFs [1-6, 8-10, 14-18, 24-29], but far less attention has been given to the separation of gas mixtures [7, 11-13, 19-23]. Among the available separation studies, Chen and coworkers performed experimental separations of light gas mixtures in several interpenetrated MOFs that exhibit high selectivity [7, 11, 12]. These experimental results encouraged us to carry out a systematic study on the effect of interpenetration (catenation) on gas mixture separations. In this work, we have selected three pairs of MOFs [30], three interpenetrated MOFs and their non-interpenetrated counterparts, which allows us to compare the effect of interpenetration while excluding the influences of the differences in chemical composition of these materials. We selected CH_4/H_2 system as the model mixture since this is an important practical system that is involved in the process of purification of synthetic gas obtained from steam re-forming of natural gas. Currently, 95% of hydrogen used in fuel cells is produced by this method, and components such as methane must be removed from the synthetic gas before hydrogen can be used effectively [31].

7.2 Models and computational method

7.2.1 MOF structures

In this work, six isoreticular metal-organic frameworks (IRMOFs), as synthesized by Eddaoudi et al. [30], were adopted as representatives of MOFs. The crystal structures of these IRMOFs were constructed from the XRD data [30] using Materials Studio Visualizer [32].

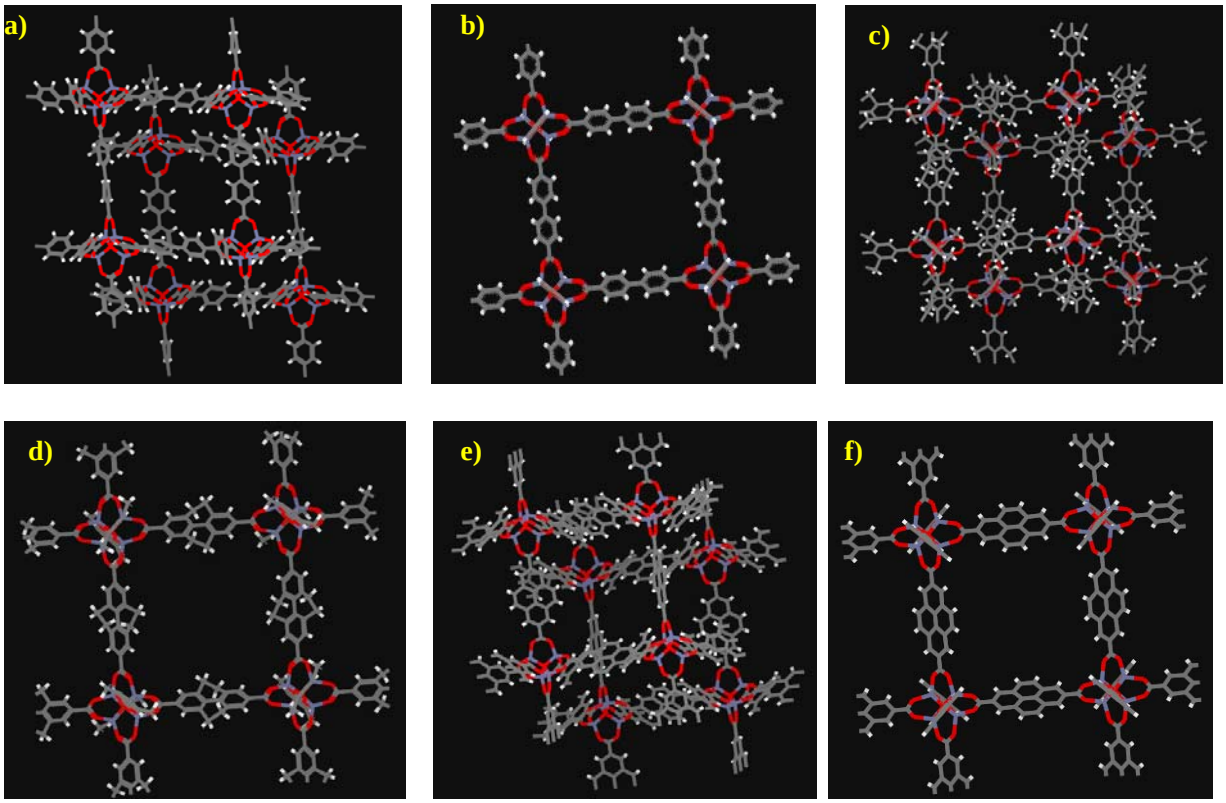

Figure 7.1: Crystal structures of the IRMOFs used in the simulation: a) IRMOF-9, b) IRMOF-10, c) IRMOF-11, d) IRMOF-12, e) IRMOF-13, f) IRMOF-14 (Zn, blue; O, red; C, gray, and H, white).

As shown in Figure 7.1, IRMOFs-10, 12, and 14 feature the same primitive cubic topology with the octahedral $Zn_4O(CO_2)$ clusters linked by different organic dicarboxylate linkers, while IRMOFs-9, 11, and 13 are the interpenetrated counterparts of IRMOFs-10, 12, and 14, respectively. The structural properties for these IRMOF materials are summarized in Table 7.1, where the free volumes were calculated using a probe size of 0.0 Å to determine the total free volume not occupied by the framework atoms. It should be noted that this method of calculating free volume, as done by others [14, 27], is based solely on the system geometry.

Material	Pore shape[a]	Unit cell (Å)	Cell angle (Degree)	d_{pore} [a] (Å)	ρ_{crys} [a] (g/cm^3)	V_{free} [b] (cm^3/g)	Porosity [b] (%)
IRMOF-10	cubic	a=b=c=34.281	α=β=γ=90	16.7/20.2	0.33	2.66	87.9
IRMOF-12	cubic	a= b=c=34.281	α=β=γ=90	13.9/20.0	0.38	2.24	85.1
IRMOF-14	cubic	a=b=c=34.381	α=β=γ=90	14.7/20.1	0.37	2.30	86.3
IRMOF-9	cubic/catenation	a=17.147, b=23.322 c=25.255	α=β=γ=90	4.5/6.3/8.1/ 10.7	0.66	1.14	74.8
IRMOF-11	cubic/catenation	a=b=24.822, c=56.734	α=β=90, γ=120	3.5/3.8/4.7/ 6.1/7.3/11.1	0.76	0.92	69.8
IRMOF-13	cubic/catenation	a=b=24.822, c=56.734	α=β=90, γ=120	4.2/4.7/6.1/ 7.0/11.4	0.75	0.95	71.4

Table 7.1: Structural properties for the IRMOFs studied in this work.

a Obtained from the XRD crystal data.[30]
b Calculated with the Materials Studio package.

7.2.2 Force fields

In the present work, a single Lennard-Jones (LJ) interaction site model was used to describe a methane molecule, and the potential parameters were taken from the TraPPE force field [33]. H_2 was modeled as a rigid diatomic molecule with bond length of 0.74 Å, and each atom H was represented as a LJ interaction site with the potential parameters taken from our previous work [34]. Electrostatic interactions were not included, as previous simulations have shown that the effects of these interactions on the adsorption of hydrogen in MOFs are very small at room temperature [35]. The above potential models have been successfully used to model the adsorptions of methane and hydrogen in MOFs [23, 34, 36]. For the IRMOFs studied here, an atomistic representation was used. For calculating the interactions between the adsorbate molecules and the atoms in the framework of the MOF materials, we adopted the universal force field (UFF) of Rappe et al. [37], which has been successfully employed to depict the adsorption [35, 38], diffusion [39, 40], and separation [20, 41] of several light gases and their mixtures in MOFs. The potential parameters used are listed in Table 7.2. In our simulations, all the LJ cross interaction parameters were determined by the Lorentz-Berthelot mixing rules.

LJ Parameters	CH_4	H_2_H	MOF_O	MOF_C	MOF_H	MOF_Zn
σ (Å)	3.73	2.72	3.12	3.43	2.57	2.46
ε / k_B (K)	148.0	10.00	30.19	52.84	22.14	62.40

Table 7.2: LJ potential parameters for CH4, H_2, and the IRMOFs used in this work.

To further confirm the reliability of the force fields adopted in this work, the adsorption isotherms of pure CH_4 and H_2 in IRMOF-1 (MOF-5) were simulated and compared with experimental data, as shown in Figure 7.2. The results show that the simulations enable excellent reproduction of the experimental adsorption isotherm of CH_4 [17] up to ca. 3 MPa. While for H_2, excellent agreement between simulation and experiment [25] is also obtained up to 2 MPa; similar conclusion has also been obtained by Frost and Snurr [27]. Therefore, the force fields adopted in this work are reliable to investigate the adsorption of CH_4/H_2 mixtures in IRMOFs with pressure up to 2 MPa.

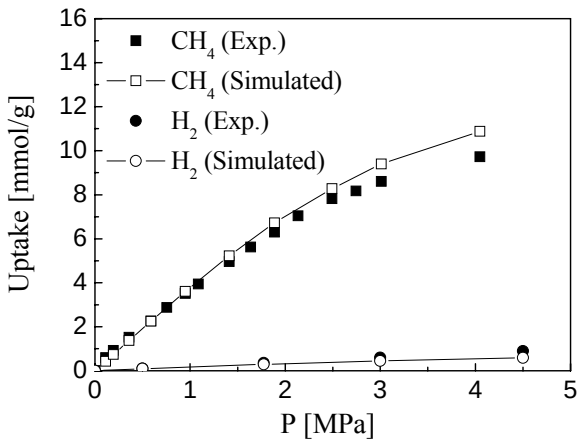

Figure 7.2: Comparison of simulated and experimental [17, 25] adsorption isotherms of CH_4 and H_2 in IRMOF-1 (MOF-5) at 298 K.

7.2.3 Simulation method

GCMC simulations were employed to calculate the adsorption of pure components and their mixtures in all IRMOFs. Similar to previous work [20-23], all the IRMOFs were treated as rigid frameworks, with atoms frozen at their crystallographic positions during simulations. A cutoff radius of 12.8 Å was applied to the LJ interactions. To convert the experimental

pressures to chemical potentials, which are required in the GCMC simulations, we used the Peng-Robinson equation of state. For each state point, GCMC simulation consisted of 1.5×10^7 steps, to guarantee equilibration, followed by 1.5×10^7 steps to sample the desired thermodynamic properties. To estimate the statistical uncertainty, the simulations were divided into 10 blocks and the standard deviation of the block average was calculated. The statistical uncertainties on the final results, including the ensemble averages of the number of adsorbate molecules in the simulation cell and the total potential energy, were estimated to be within ± 2%. A detailed description of the simulation methods can be found in Ref. 42.

7.3 Results and discussion

In separation processes a good indication of the ability for separation is the selectivity of a porous material for different components in mixtures. The selectivity for component *A* relative to component *B* is defined by $S=(x_A/x_B)(y_B/y_A)$, where x_A and x_B are the mole fractions of components *A* and *B* in the adsorbed phase, and y_A and y_B are the mole fractions of components *A* and *B* in the bulk phase, respectively. In this work, we first compared the adsorption selectivity of the six MOFs to reveal the effect of interpenetration, then, studied the effect of mixture composition on selectivity, and finally carried out ideal adsorbed solution theory (IAST) calculations to check whether IAST is applicable to MOFs with interpenetration.

7.3.1 Adsorption selectivity

As a first step, we performed molecular simulations to calculate the adsorption selectivity of methane from the binary mixtures of CH_4/H_2 in the three interpenetrated IRMOFs as well as their non-interpenetrated counterparts. The results for five different gas compositions at 298 K are shown in Figure 7.3 as a function of the bulk pressure up to 2.0 MPa.

Figure 7.3 shows the effect of interpenetration (catenation) on gas mixture separation is most pronounced at room temperature. The adsorption selectivities for CH_4 in the IRMOFs (IRMOF-9, IRMOF-11, and IRMOF-13) with interpenetration are much higher than those in their corresponding non-interpenetrated counterparts (IRMOF-10, IRMOF-12, and IRMOF-14, respectively), indicating that catenation can improve the adsorption selectivity for CH_4/H_2 system significantly. Separation of equimolar mixture of CH_4/H_2 has been performed in other porous materials, for example, at room temperature and moderate pressure, the selectivity of CH_4 is 5.0 in MOF-5 [21], 13.3 in Cu-BTC [21], 8.0 in SAPO-34 membrance [43], 2.0 in microporous SSF membrane [44], and 13.0 in carbon nanotubes [45]. Figure 7.3 demonstrates that IRMOF-9, IRMOF-11, and IRMOF-13 show much larger selectivity than the above

mentioned materials, illustrating the generation of interpenetrated structures is a promising strategy to produce MOF materials for separation applications.

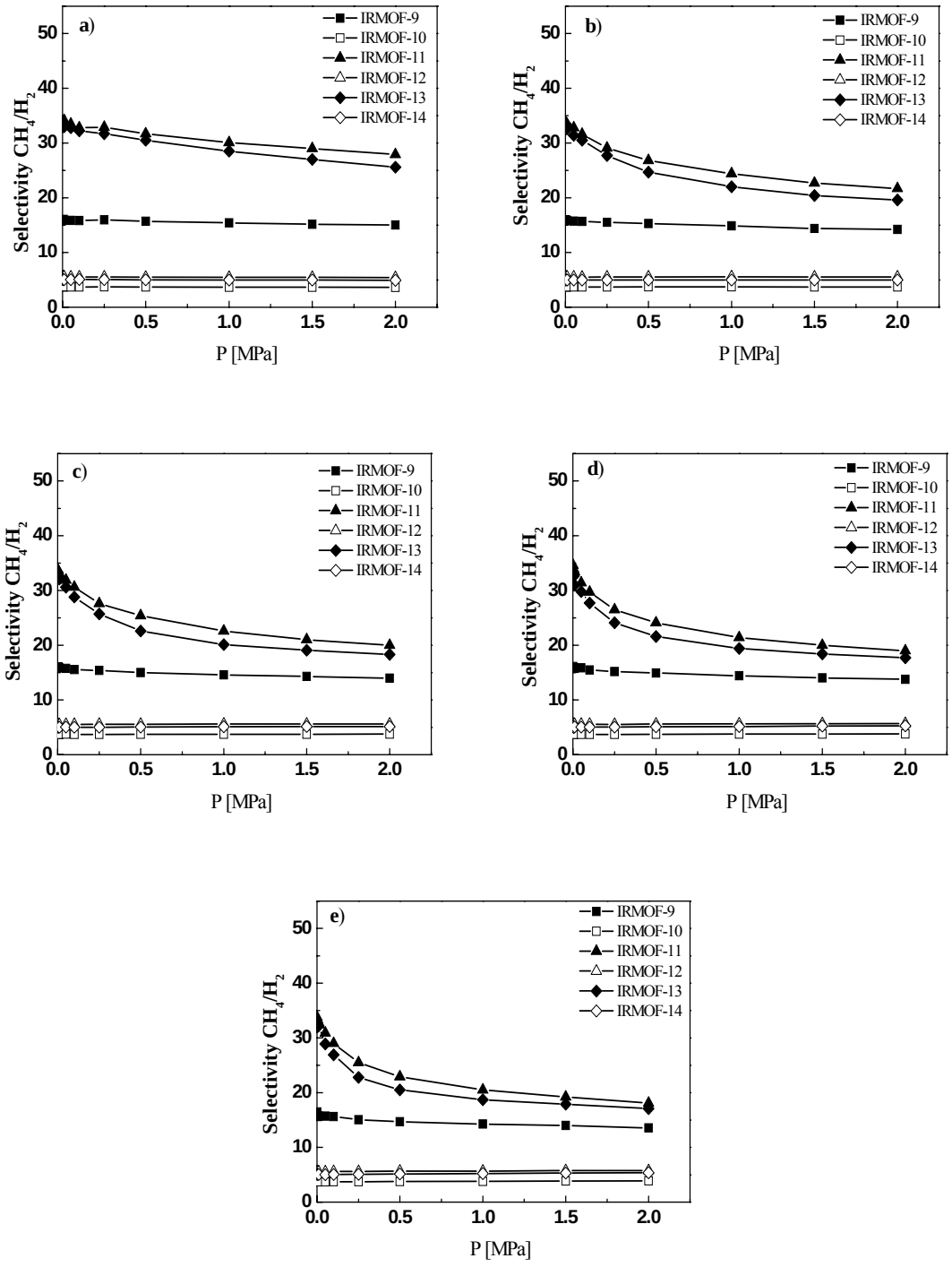

Figure 7.3: Selectivity for CH_4 from binary mixtures of CH_4/H_2 with various gas compositions at 298 K: a) 5% CH_4 and 95% H_2, b) 30% CH_4 and 70% H_2, c) 50% CH_4 and 50% H_2, d) 70% CH_4 and 30% H_2, and e) 95 % CH_4 and 5% H_2.

In addition, from Figure 7.3 we can see that the pressure dependence of the adsorption selectivity is much different in the non-interpenetrated IRMOFs and their interpenetrated counterparts. For IRMOF-10, IRMOF-12, and IRMOF-14, the selectivities of methane are

nearly pressure-independent for all the gas compositions within the pressure range studied. The reasons are that their crystal structures are very simple with large cubic pores, and up to 2.0 MPa there is still much space in the pores of the materials, thus, the packing effect that favors the adsorption of hydrogen will only play a role at much higher pressures. As to IRMOF-9, IRMOF-11, and IRMOF-13, the adsorption selectivity curves contain two steps: a quick decrease at low pressures, followed by a slow decrease with further increasing pressure, and with increasing the gas compositions of CH_4 this trend becomes more pronounced. This can be attributed to the facts that in the interpenetrated IRMOFs there are different types of pores (4 in IRMOF-9, 6 in IRMOF-11, and 5 in IRMOF-13) with much smaller sizes. This is leading to stronger confinement effects and the packing effects become evident at low pressures; the existence of small pores together with the heterogeneity in pore size results in a decrease of methane selectivity with increasing pressure. Similar behavior has also been observed in our previous work for the separation of CH_4/H_2 mixture in Cu-BTC, which has two kinds of small size pores [21].

To understand the effect of interpenetration, we further analyzed the loading-dependency of the adsorbate/IRMOF framework interactions for equimolar mixture of CH_4/H_2. Figure 7.4 shows the isosteric heats of adsorption as a function of pressure. The differences of isosteric heats of adsorption between CH_4 and H_2 in the IRMOFs with interpenetration are much higher than those in their non-interpenetrated counterparts; this explains the much larger selectivity observed in the former in the pressure range studied. Also, the pressure-dependency behavior of the difference of isosteric heats of adsorption is similar to that of selectivity (Figure 7.3). For the non-interpenetrated IRMOFs, the adsorbate-adsorbent interactions slightly decrease in a similar extent with increasing pressure (loading) for both CH_4 and H_2 in the pressure range studied, resulting in the differences of isosteric heats of adsorption between CH_4 and H_2 nearly unchanged. Again this can be attributed to the facts that the crystal structures of these non-interpenetrated IRMOFs are very simple with large cubic pores, and up to 2.0 MPa there is still much space in the pores of the material. For the interpenetrated IRMOFs, the behaviors are caused by the existence of various small pores of different sizes; the small pores and the heterogeneous nature in pore size result in a decrease of the differences of isosteric heats of adsorption with increasing loading (pressure).

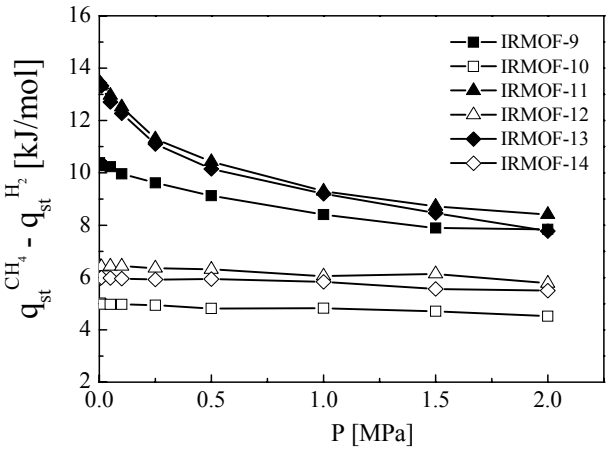

Figure 7.4: The differences of isosteric heats of adsorption between CH_4 and H_2 in the six IRMOFs as a function of pressure (only the parts contributed by the adsorbate/IRMOF framework interactions are given).

As the structures of interpenetrated IRMOFs are somewhat more complicated, it is instructive to study the sitting of hydrogen and methane molecules in these IRMOFs in detail and to clarify the different separation selectivity regions in them. The center of mass (COM) probability distributions of methane and hydrogen for equimolar mixture of CH_4/H_2 in the three interpenetrated IRMOFs at different pressures were examined. Figure 7.5 shows, as an example, these distributions in IRMOF-9.

CH_4

a) P = 0.1 MPa **b) P = 1 MPa** **c) P = 2 MPa**

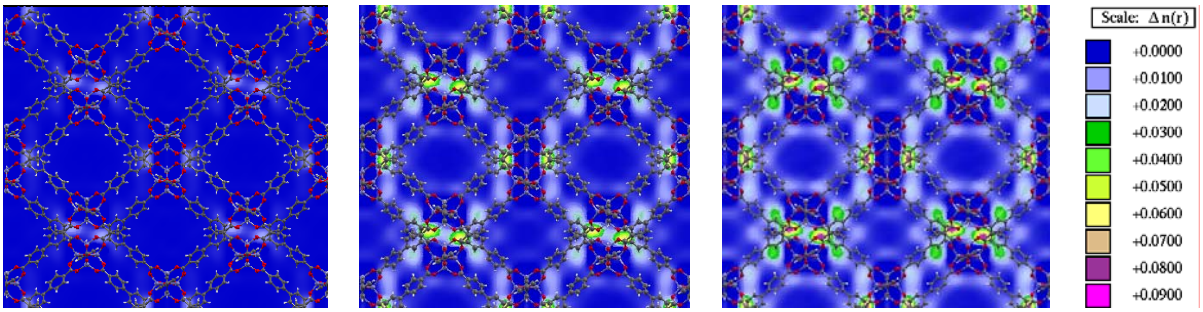

H_2

d) P = 0.1 MPa **e) P = 1 MPa** **f) P = 2 MPa**

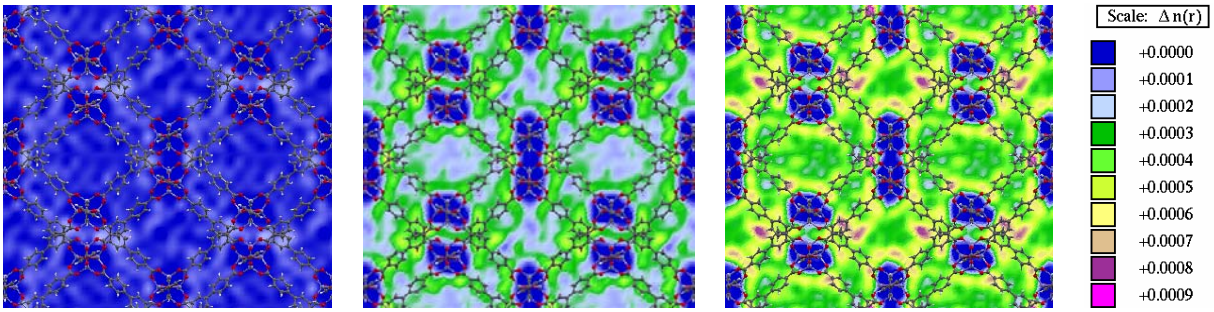

Figure 7.5: Contour plots of the COM probability densities of CH_4 ((a)-(c)) and H_2 ((d)-(f)) in planes through the catenated area in IRMOF-9 at different pressures (Zn, blue; O, red; C, gray, and H, white).

As can be seen from Figures 7.5(a)-(c) (here we only show the COM probability densities of methane for clarity), strongest adsorption for methane occurs in the small pores formed by the interpenetration of the frameworks, the ones formed by two metal clusters and phenyl linkers, particularly in the corner area, where strongest overlap of the interactions from metal clusters and phenyl linkers occurs; with increasing pressure (loading), the areas formed by one metal cluster and a phenyl linker in another chain also adsorb methane strongly (Figures 7.5(b) and (c)). This confirms that catenation can improve gas affinity. The COM probability densities of hydrogen are shown in Figures 7.5(d)-(f). Methane was omitted for clarity. Similar to methane, at low pressure, hydrogen is preferably to be adsorbed in the small pores formed by two metal clusters and phenyl linkers; however, with increasing pressure, hydrogen molecules seem to distribute more uniformly in the material (Figures 7.5(e) and (f)), due to the presence of more methane molecules that occupied most the favorable adsorption sites. It seems largest selectivity should occur in the small pores formed by interpenetration;

however, it is difficult to get a clear picture from the COM figures shown in Figure 7.5. Therefore, we computed the local selectivity in the materials.

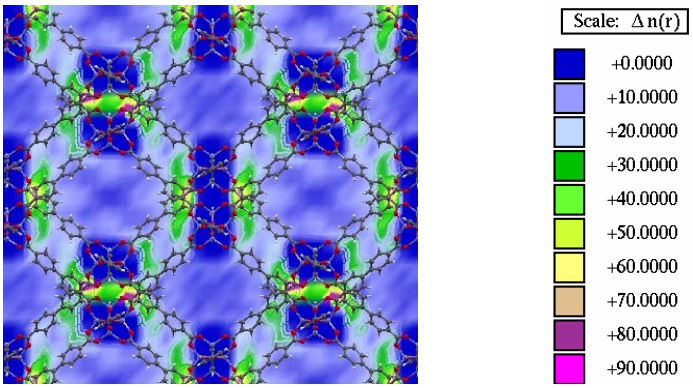

Figure 7.6: Contour plot of adsorption selectivities of CH_4 for equimolar mixture of CH_4/H_2 at 2 MPa and 298 K in planes through the catenated area in IRMOF-9 (Zn, blue; O, red; C, gray, and H, white).

The selectivity distribution of methane for equimolar mixture of CH_4/H_2 in IRMOF-9 at 298 K and 2 MPa is shown in Figure 7.6. The selectivity distribution is heterogeneous in the material, with highest selectivity occurs in the small pores formed by two metal clusters and phenyl linkers. In this region the selectivity ranges from 30 to 90, much higher than the average value of 14. The small pores formed by the linker-linker region also show high selectivity (around 20), with lowest selectivity in the center of the large pores (around 4). Figure 7.6 gives a clear picture of the selectivity distribution in the material, and it is expected that with increasing pressure, the contribution of the small pores formed by linker-linker region will become more important. Selectivity distribution plot for 1 MPa is very similar to the one for 2 MPa. As to 0.1 MPa, since the number of molecules in the system is too small to reliably estimate the local selectivity, the selectivity distribution figure was not calculated.

7.3.2 Effect of composition on selectivity

For practical applications, it is useful to know how the adsorption selectivity varies with the gas mixture composition. Figure 7.7 gives the selectivities of methane for CH_4/H_2 mixtures at five compositions, as a function of the total pressure. Figure 7.7 shows that the selectivity does not strongly depend on gas mixture composition for the three non-interpenetrated IRMOFs within the pressure range studied. For the interpenetrated frameworks, however, the mixture composition does affect the selectivity. This can be attributed to the differences in crystal structures of these two types of materials. The three non-interpenetrated IRMOFs have very

simple crystal structures and the pores are rather large compared to the adsorbates studied. Within the pressure range considered, there is still much free volume in the pores of these materials for all gas mixture compositions. While for the interpenetrated IRMOFs the situation is different as they have various smaller pores of different sizes, resulting in more complicated structures. Therefore, the selectivity is more sensitive to both pressure and composition. As can be seen from Figure 7.7, the selectivities of methane at various compositions are identical at very low pressure; while with increasing pressure, methane selectivity decreases with increasing bulk molar fraction of methane. The reasons for these phenomena are that in infinite dilution region, selectivity of a mixture depends mainly on the interactions of the adsorbent with the adsorbate. At higher pressures, however, the molecules have to compete for space and confinement effects become evident; in this case, pore size, topology, as well as heterogeneity in structure play more important roles, and their effects on selectivity depend on the composition of the mixtures in the pores. Although the mixture composition affects the selectivity in the three interpenetrated IRMOFs, within the entire composition range they show much larger methane selectivity than their non-interpenetrated counterparts. Therefore, this work demonstrates that the creation of interpenetrated frameworks is a promising strategy to develop new MOFs with enhanced adsorption separation selectivity.

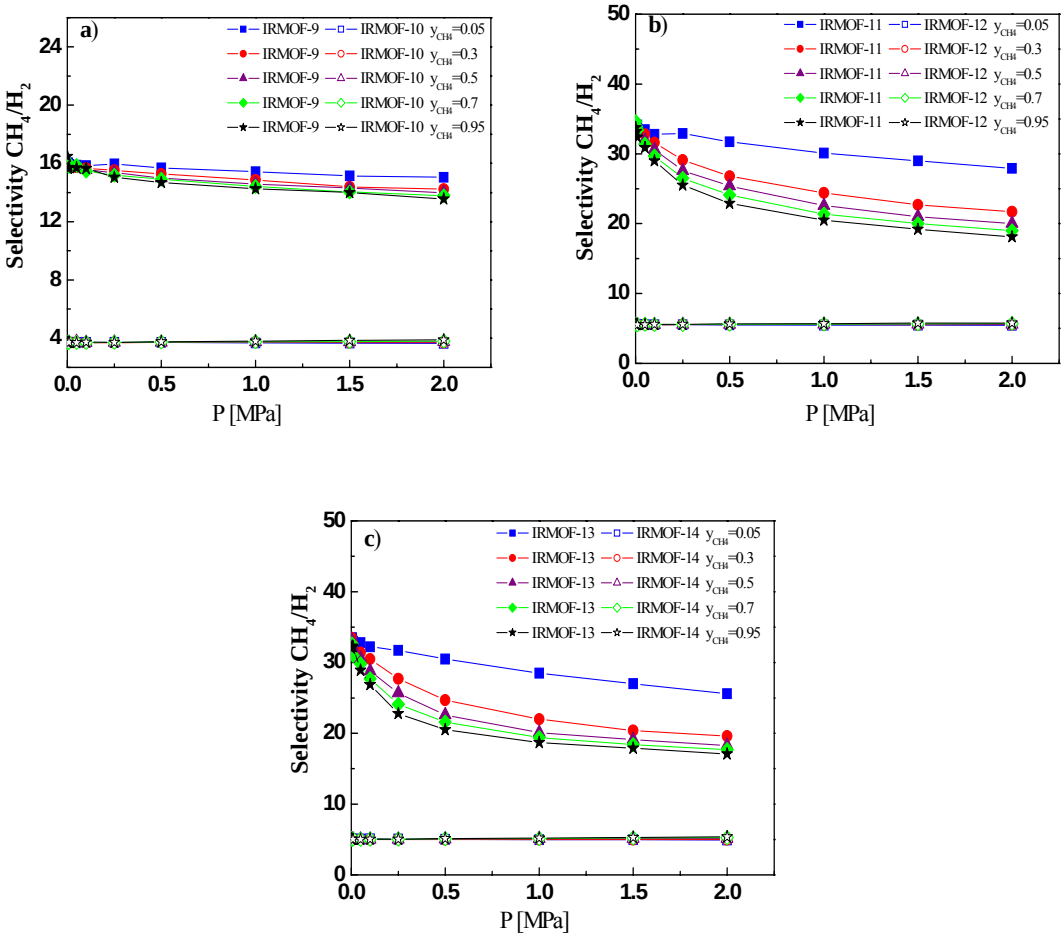

Figure 7.7: CH_4 selectivities from binary mixtures of CH_4/H_2 as a function of gas composition and pressure at 298 K in: a) IRMOF-9 and IRMOF-10, b) IRMOF-11 and IRMOF-12, and c) IRMOF-13 and IRMOF-14.

7.3.3 IAST prediction

It has been commonly recognized that ideal adsorbed solution theory (IAST) [46] can give good predictions of gas mixture adsorption in many zeolites [47, 48], and in our previous work we have demonstrated it is applicable for depicting the CH_4/H_2 adsorption in non-interpenetrated IRMOF-1 and Cu-BTC [21]. IAST calculations were performed to check whether this is also the case for interpenetrated MOFs. The calculated adsorption selectivities of methane at different compositions with GCMC and IAST in IRMOF-9 and IRMOF-11 are shown in Figure 7.8. In all the cases, good agreement between GCMC simulation and IAST calculation was obtained, indicating that IAST is applicable to predict the adsorption behavior of CH_4/H_2 mixture in the interpenetrated IRMOFs studied.

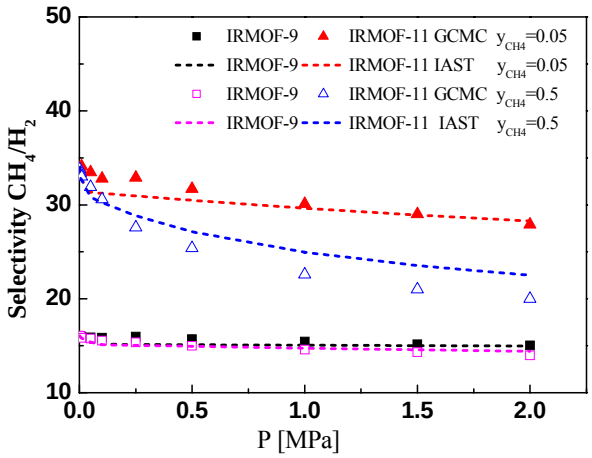

Figure 7.8: Comparison of IAST and GCMC for CH_4 selectivity from binary mixtures of CH_4/H_2 as a function of gas composition and pressure in IRMOF-9 and IRMOF-11 at 298 K.

7.4 Conclusions

This work shows that, due to the additional small pores and adsorption sites formed by the interpenetration of frameworks, the adsorption selectivity of CH_4/H_2 mixtures is greatly enhanced in the three interpenetrated IRMOFs compared with their non-interpenetrated counterparts. In the interpenetrated MOFs, because of the existence of various small pores of different sizes, methane selectivity shows more complex behavior, and the selectivity differs largely in the different areas of the pores. In addition, this work shows IAST is likely to be applicable to interpenetrated MOFs with complex structures. Based on the results obtained, it may be concluded that the creation of interpenetrated frameworks is a promising strategy to develop MOFs with high separation performance.

At the moment, there are no experimental data to check our results; it would be interesting to see whether experiments can confirm our observations in the future. Also, it would be an interesting topic to study the performance of membranes based on these MOFs, both experimentally and theoretically.

Bibliography

[1] Rowsell, J. L. C.; Yaghi, O. M. *Angew. Chem. Int. Ed*. **2005**, *44*, 4670.

[2] Férey, G. *Chem. Soc. Rev.* **2008**, *37*, 191.

[3] Mueller, U.; Schubert, M.; Teich, F.; Puetter, H.; Schierle-Arndt, K.; Pastré, J. *J. Mater. Chem.* **2006**, *16*, 626.

[4] Kubota, Y.; Takata, M.; Matsuda, R.; Kitaura, R.; Kitagawa, S.; Kato, K.; Sakata, M.;

Kobayashi, T. C. *Angew. Chem. Int. Ed.* **2005**, *44*, 920.

[5] Kayes, S. S.; Long, J. R. *J. Am. Chem. Soc.* **2008**, *130*, 806.

[6] Kesanli, B.; Cui, Y.; Smith, M. R.; Bittner, E. W.; Bockrath, B. C.; Lin, W. *Angew. Chem. Int. Ed.* **2005**, *44*, 72.

[7] Chen, B.; Ma, S.; Hurtado, E. J.; Lobkovsky, E. B.; Zhou, H. C. *Inorg. Chem.* **2007**, *46*, 8490.

[8] Ma, S.; Sun, D.; Ambrogio, M.; Fillinger, J. A.; Parkin, S.; Zhou, H. C. *J. Am. Chem. Soc.* **2007**, *129*, 1858.

[9] Rowsell, J. L. C.; Yaghi, O. M. *J. Am. Chem. Soc.* **2006**, *128,* 1304.

[10] Chen, B.; Ma, S.; Zapata, F.; Lobkovsky, E. B.; Yang, J. *Inorg. Chem.* **2006**, *45*, 5718.

[11] Chen, B.; Liang, C.; Yang, J.; Contreras, D. S.; Clancy, Y. L.; Lobkovsky, E. B.; Yaghi, O. M.; Dai, S. *Angew. Chem. Int. Ed.* **2006**, *45*, 1390.

[12] Bastin, L.; Bárcia, P. S.; Hurtado, E. J.; Silva, J. A. C.; Rodrigues, A. E.; Chen, B. *J. Phys. Chem. C* **2008,** *112,* 1575.

[13] Bárcia, P. S.; Zapata, F.; Silva, J. A. C.; Rodrigues, A. E.; Chen, B. *J. Phys. Chem. B* **2007**, *111*, 6101.

[14] Fost, H.; Düren, T.; Snurr, R. Q. *J. Phys. Chem. B* 2006, *110*, 9565.

[15] Walton, K. S.; Millward, A. R.; Dubbeldam, D.; Frost, H.; Low, J. J.; Yaghi, O. M.; Snurr, R. Q. *J. Am. Chem. Soc.* **2008**, *130*, 406.

[16] Ramsahye, N. A.; Maurin, G.; Bourrelly, S.; Llewellyn, P. L.; Serre, C.; Loiseau, T.; Devic, T.; Ferey, G. *J. Phys. Chem. C* **2008**, *112*, 514.

[17] Düren, T.; Sarkisov, L.; Yaghi, O. M.; Snurr, R. Q. *Langmuir* **2004,** *20,* 2683.

[18] Liu, J.; Culp, J. T.; Natesakhawat, S.; Bockrath, B. C.; Zande, B.; Sankar, S. G.; Garberoglio, G.; Johnson, J. K. *J. Phys. Chem. C* **2007,** *111,* 9305.

[19] Yang, Q.; Xue, C.; Zhong ,C.; Chen, J. *AIChE J.* **2007**, *53*, 2832.

[20] Keskin, S.; Sholl, D. S. *J. Phys. Chem. C* **2007**, *111*, 14055.

[21] Yang, Q.; Zhong ,C. *J. Phys. Chem. B* **2006**, *110*, 17776.

[22] Yang, Q.; Zhong, C. *ChemPhysChem* **2006**, *7*, 1417.

[23] Düren, T.; Snurr, R. Q. *J. Phys. Chem. B* **2004**, *108*, 15703.

[24] Latroche, M.; Surblé, S.; Serre, C.; Mellot-Draznieks, C.; Llewellyn, P. L.; Lee, J. H.; Chang, J. S.; Jhung, S. H.; Férey, G. *Angew. Chem. Int. Ed*. **2006**, *45*, 8227.

[25] Li, Y.; Yang, R. T. *J. Am. Chem. Soc.* **2006**, *128*, 8136.

[26] Kaye, S. S.; Dailly, A.; Yaghi, O. M.; Long, J. R. *J. Am. Chem. Soc.* **2007**, *129*, 14176.

[27] Frost, H.; Snurr, R. Q. *J. Phys. Chem. C* **2007**, *111*, 18794.

[28] Dubbeldam, D.; Frost, H.; Walton, K. S.; Snurr, R. Q. *Fluid Phase Equilibr.* **2007**, *261*, 152.

[29] Yang, Q.; Zhong ,C. *J. Phys. Chem. C* **2008**, *112*, 1562.

[30] Eddaoudi, M.; Kim, J.; Rosi, N.; Vodak, D.; Wachter, J.; O'Keeffe, M.; Yaghi, O. M. *Science* **2002**, *295*, 469.

[31] Mitchell, M. C.; Gallo, M.; Nenoff, T. M. *J. Chem. Phys.* **2004**, *121*, 1910.

[32] Accelrys, Inc., Materials Studio, 3.0 V; Accelrys Inc: San Diego, CA, **2003**.

[33] Martin, M. G.; Siepmann, J. I. *J. Phys. Chem. B* **1998**, *102*, 2569.

[34] Yang, Q.; Zhong, C. *J. Phys. Chem. B* **2005**, *109*, 11862.

[35] Garberoglio G.; Skoulidas, A. I.; Johnson, J. K. *J. Phys. Chem. B* **2005**, *111,* 13094.

[36] Surblé, S.; Millange, F.; Serre, C.; Düren, T.; Latroche, M.; Bourrelly, S.; Llewellyn, P. L.; Férey, G. *J. Am. Chem. Soc.* **2006**, *128*, 14889.

[37] Rappé, A. K.; Casewit, C. J.; Colwell, K. S.; Goddard III, W. A.; Skiff, W. M. *J. Am. Chem. Soc.* **1992**, *114*, 10024.

[38] Krungleviciute,V.; Lask, K.; Heroux, L.; Migone, A. D.; Lee, J.-Y.; Li, J.; Skoulidas, A. *Langmuir* **2007**, *23*, 3106.

[39] Skoulidas, A. I.; Sholl, D. S. *J. Phys. Chem. B* **2005**, *109*, 15760.

[40] Skoulidas, A. I. *J. Am. Chem. Soc.* **2004**, *126*, 1356.

[41] Babarao, R.; Hu, Z.; Jiang, J.; Chempath, S.; Sandler, S. I. *Langmuir* **2007,** *23,* 659.

[42] Frenkel, D.; Smit, B. *Understanding Molecular Simulations: From Algorithms to Applications*, 2nd ed.; Academic Press: San Diego, CA, 2002.

[43] Poshysta, J. C. ; Tuan, V. A. ; Pape, E. A. ; Noble, R. D. ; Falconer, J. L. *AIChE J.* **2000**, *46*, 779.

[44] Vieira-Linhares, A. M.; Seaton, N. A. *Chem. Eng. Sci.* **2003**, *58*, 4129.

[45] Chen, H. B.; Sholl, D. S. *J. Membrane. Sci.* **2006**, *269*, 152.

[46] Myers, A. L.; Prausnitz, J. M. *AIChE J.* **1965**, *11*, 121.

[47] Goj, A; Sholl, D. S.; Akten, E. D.; Kohen, D. *J. Phys. Chem.* **2002**, *106*, 8367.

[48] Challa, S. R.; Sholl, D. S.; Johnson, J. K. *J. Chem. Phys*. **2002**, *116*, 814.

Summary

This thesis describes a simulation study of adsorption and diffusion phenomena of gases in porous materials, i.e. zeolites and metal-organic frameworks (MOFs).

Zeolites are microporous materials that are found in a wide range of applications, such as efficient heterogeneous catalysts and adsorbents in the petrochemical industry. In these petrochemical applications the adsorption of hydrocarbons in zeolite pores plays an important role. Therefore, it is of great importance to explore the adsorption behavior of hydrocarbons in different zeolites from both scientific and practical points of view.

MOFs are a relatively new family of hybrid porous materials that are formed by the coordination of metal ions with organic linkers. These materials feature opportunities for functionality and structure by a rational combination of different metal ions with different organic linkers. These materials have various promising applications in, for example, gas storage, separation, or catalysis, etc. According to the structural characteristics, they can be categorized into two types: those with non-interpenetrated frameworks and those with interpenetrated ones. In the latter additional small pores and adsorption sites are formed by the interpenetration of frameworks, leading to MOFs with multi-pores of different sizes that may exhibit different gas adsorption, diffusion, and separation properties. In this work we investigate the effect of interpenetration on the adsorption and diffusion behaviors of gases/gas mixtures in interpenetrated MOFs.

Evaluation of a Force Field for Describing the Adsorption Behavior of Alkanes in Various Pure Silica Zeolites

Because force fields play an important role in molecular simulations, in chapter 2 we test the applicability of a united-atom force field developed by Dubbeldam *et al.* to various pure silica zeolites. Our results show that the united-atom force field of Dubbeldam *et al.* developed for MFI-type zeolites is applicable to other pure silica zeolites, such as FER-, MWW-, MTW-, CFI-, and LTA-type zeolites. It may be concluded that this united-atom force field is a general force field applicable to most pure silica zeolites.

Development of a New Force Field for Alkenes in Zeolites

In chapter 3 a new united-atom force field is developed which accurately describes the adsorption properties of linear alkenes in zeolites. With this force field, we perform a comparative study on the adsorption behavior of ethene and propene in four pure-silica small pore eight-membered ring zeolites, CHA, DDR, ITE, and IHW, since they have been recognized as promising candidates for the separation of alkene from olefin/paraffin mixtures in the petrochemical industry. The differences in adsorption capacities and of the shapes of the adsorption isotherms for the four zeolites are elucidated and related to their structures with the microscopic information obtained.

Adsorption of Alkanes in Na-MOR Zeolites

In chapter 4 the adsorption behavior of linear alkanes in Na-MOR zeolites are studied in detail. We first validate a force field developed for Na-FAU zeolites by Calero *et al.* to Na-MOR zeolites; based on the validated force field we further study the relationship between sodium cations and the adsorption behavior of butane in MOR-type zeolites, and finally, the adsorption behavior of larger alkanes such as C_5-C_7 is investigated to understand the influences of the location and density of cations on the adsorption.

Understanding Aluminium Location and Non-framework Ions Effects on Alkane Adsorption in Aluminosilicates

The structure of zeolites is composed of silicon and aluminium oxide tetrahedra and charge-balancing ions. The presence of cations or protons influences the adsorption properties of the zeolites. As the positions and stability of cations or protons in the zeolites are strongly related to their Al distributions, it is therefore important to identify the aluminium site locations. In chapter 5, firstly, we identify the most likely positions of aluminium in TON, FER, and MOR zeolites. Then with the determined structures, the effects of non-framework ions on the adsorption behaviors of alkanes in these zeolites are studied systematically and the relations of the macroscopic adsorption behaviors of alkanes to their microscopic structures are elucidated. Our results show that by matching the simulation data with the available experimental values the most likely position of aluminium in zeolites could be identified. The

aluminium distributions in zeolites strongly affect the positions and stability of cations or protons, which in turn influence the adsorption behavior of alkanes.

Hydrogen Diffusion in Interpenetrated Metal-Organic Frameworks

In chapter 6 a combined molecular dynamics simulation and dynamically corrected transition state theory (dcTST) study is performed to investigate the effect of interpenetration (catenation) on hydrogen diffusion in MOFs. The results on 10 isoreticular MOFs (IRMOFs) with and without interpenetration show that catenation can reduce the hydrogen diffusivity by a factor of 2 to 3 at room temperature. For the interpenetrated IRMOFs with multi-pores of different sizes, free volume can serve as a measure for hydrogen diffusivity: the bigger the free volume, the larger the hydrogen diffusivity. In addition, the present work shows that dcTST can directly reveal the influence of the MOF structure on hydrogen diffusivity, which is a powerful tool to provide a better understanding of the relationship between gas diffusivity and MOF structure.

Separation of Methane and Hydrogen Mixtures in Interpenetrated Metal-Organic Frameworks

In chapter 7 we perform a systematic molecular simulation study to investigate the effect of interpenetration on gas mixture separation in MOFs. Our results show that the adsorption selectivity of CH_4/H_2 mixtures is greatly enhanced in the interpenetrated IRMOFs compared with their non-interpenetrated counterparts. This enhancement is due to the formation of additional small pores and adsorption sites by the interpenetration of frameworks. Furthermore, this work shows that the pressure dependency behavior of adsorption selectivity, the composition dependency behavior of adsorption selectivity, and the occupying situation of H_2 and CH_4 molecules in the non-interpenetrated IRMOFs and their interpenetrated counterparts are much different. In addition, the present work shows that the ideal adsorbed solution theory (IAST) gives a good prediction of CH_4/H_2 mixture adsorption in interpenetrated MOFs with complex structures, on the basis of the pure component data in these structures. Based on the results obtained in this work, it can be concluded that the creation of interpenetrated frameworks is a promising strategy to develop MOFs with high separation performance.

Samenvatting (Summary in Dutch)

Dit proefschrift beschrijft een simulatiestudie van adsorptie en diffusie verschijnselen van gassen in poreuze materialen, namelijk zeolieten en organometallische structuren (MOFs).

Zeolieten zijn microporeuze materialen die gebruikt worden in een groot aantal toepassingen, zoals efficiënte heterogene katalysatoren en adsorbenten in de petrochemische industrie. In deze petrochemische toepassingen speelt de adsorptie van koolstoffen in zeolietporiën een belangrijke rol. Daarom is het, omwille van zowel louter wetenschappelijke als praktische redenen, bijzonder belangrijk om de adsorptie van koolstoffen in verschillende zeolieten te bestuderen.

Organometallische structuren (MOFs) vormen een vrij nieuwe familie van hybride poreuze materialen die gevormd worden door de coördinatie van metaalionen met organische binders. Deze materialen worden gekenmerkt door de mogelijkheid om hun functionaliteit en structuur te optimalizeren door een rationele combinatie van verschillende metaalionen met verschillende organische binders. Deze materialen hebben verschillende veel belovende toepassingen in bijvoorbeeld gasopslag, scheidingen of katalyse. Afhankelijk van de structurele kenmerken, kunnen deze materialen onderverdeeld worden in twee types: met en zonder in elkaar verweven structuren. Door de interpenetratie van structuren ontstaan nieuwe kleinere poriën en adsorptie sites. Dit leidt tot MOFs met vele poriën met uiteenlopende groottes die verschillende gasadsorptie, diffusie en scheidings eigenschappen hebben. In dit werk bestuderen we het effect van interpenetratie op adsorptie en diffusie gedrag van gassen en gasmengsels in verweven MOFs.

Evaluatie van een krachtveld voor de beschrijving van het adsorptiegedrag van alkanen in verschillende silicium zeolieten

Aangezien krachtvelden een belangrijke rol spelen in moleculaire simulaties, testen we in hoofdstuk 2 de toepasbaarheid van een united-atom krachtveld ontwikkeld door Dubbeldam et al. op verschillende zuiver silicium zeolieten. Onze resultaten tonen aan dat het united-atom krachtveld van Dubbeldam et al., ontworpen voor zeolieten van het type MFI, toepasbaar is op

andere types zuiver silicium zeolieten, zoals FER, MWW, MTW, CFI, ans LTA. Dit resultaat toont aan dat dit united-atom krachtveld toepasbaar is op de meeste silicium zeolieten.

Ontwikkeling van een nieuw krachtveld voor alkenen in zeolieten

In hoofdstuk 3 wordt een nieuw united-atom krachtveld ontwikkeld dat de adsorptie eigenschappen van lineaire alkenen in zeolieten precies beschrijft. Met behulp van dit krachtveld maken we een vergelijkende studie van het adsorptiegedrag van etheen en propeen in vier silicium zeolieten met kleine poriën en achtdelige ring (CHA, DDR, ITE en IHW). Deze zeolieten zijn veelbelovende kandidaten voor de scheiding van alkenen uit mengsels van olefinen en paraffinen in de petrochemische industrie. De verschillen in de adsorptie capaciteit en in de vormen van de adsorptie isothermen tussen de vier zeolieten worden opgehelderd en in verband gebracht met hun structuren aan de hand van de verworven microscopische informatie.

Adsorptie van alkanen in Na-MOR Zeolieten

In hoofdstuk 4 wordt de adsorptie van lineaire alkanen in Na-MOR zeolieten in detail bestudeerd. We bekijken eerst de toepasbaarheid van het krachtveld ontwikkeld voor Na-FAU zeolieten door Calero et al. op Na-MOR zeolieten. Met behulp van dit krachtveld bestuderen we het verband tussen Na kationen and het adsorptie gedrag van butaan in zeolieten van het type MOR. Het adsorptie gedrag van langere alkanen zoals C_5-C_7 wordt onderzocht om de invloed van de locatie en van de dichtheid van de kationen op de adsorptie te begrijpen.

Invloed van de positie van aluminium en het effect op de adsorptie van alkanen in aluminiumsilicaten

De zeolietstructuur bestaat uit silicium en aluminiumoxide tetraëders en ionen met verchillende lading. Het voorkomen van kationen of protonen beïnvloedt het adsorptiegedrag van de zeolieten. Aangezien de positie en de stabiliteit van de kationen of protonen in zeolieten sterk gerelateerd is aan de distributie van Al is het belangrijk om de aluminium sites te identificeren. In hoofdstuk 5 bepalen we eerst de meest waarschijnlijke posities van aluminium in TON, FER en MOR zeolieten. Vervolgens bepalen we met deze structuren de effecten van de ionen die niet tot de zeolietstructuur behoren op het adsorptiegedrag van alkanen. Dit geeft ons inzicht in het verband tussen het macroscopisch adsorptiegedrag van

alkanen en de microstructuur van de zeolieten. Onze resultaten tonen aan dat het mogelijk is om de meest waarschijnlijke posities van aluminium in zeolieten te identificeren door de gesimuleerde resultaten te vergelijken met de experimentele. De verdeling van aluminium in zeolieten beïnvloedt sterk de plaats en de stabiliteit van kationen of protonen, wat dan het adsorptiegedrag van alkanen beïnvloedt.

Diffusie van waterstof in in elkaar verweven organometallische structuren

In hoofdstuk 6 wordt een moleculaire dynamica studie gecombineerd met dynamisch gecorrigeerde transitietoestandstheorie (dcTST) met als doel het effect van interpenetratie (catenatie) op waterstof diffusie in MOF zeolieten te bestuderen. De resultaten van 10 verschillende MOFs met dezelfde structuur (IRMOFs) maar al dan niet interpenetratie tonen aan dat catenatie de waterstof diffusiviteit met een factor 2 tot 3 kan verkleinen bij kamertemperatuur. In de in elkaar verweven IRMOFs met verschillende poriën van verschillende afmetingen kan het vrije volume dienen als een maat voor de waterstofdiffusiviteit. Hoe groter het vrije volume, des te groter is de waterstofdiffusiviteit. Daarbij toont deze studie aan dat dcTST onmiddellijk de invloed van de MOF structuur op de waterstofdiffusiviteit kan weergeven. Dit is een krachtig instrument om het verband tussen gas diffusiviteit en MOF structuur te verduidelijken.

Scheiding van methaan en waterstof mengsels in in elkaar verweven organometallische structuren

In hoofdstuk 7 voeren we een systematische moleculaire dynamica studie uit om het effect van interpenetratie op de scheiding van gas mengsels in MOFs te bestuderen. Onze resultaten tonen aan dat de adsorptieselectiviteit van CH_4/H_2 mengsels sterk vergroot wordt in de in elkaar verweven IRMOFs in vergelijking met de niet verweven zeolieten. Deze vergroting wordt veroorzaakt door de vorming van nieuwe kleine poriën en adsorptie sites door de interpenetratie van de structuren. Bovendien toont dit werk aan dat het druk- en samenstellingafhankelijke adsorptieselectief gedrag en de bezetting door H_2 en CH_4 moleculen verschillen in de in elkaar verweven IRMOFs en in de niet verweven zeolieten. Dit werk toont ook aan dat de ideaal geadsorbeerde oplossing theorie (IAST) de adsorptie van het CH_4/H_2 mengsel in in elkaar verweven MOFs met complexe structuren goed voorspelt op basis van de data van de zuivere componenten in deze structuren. Op basis van de resultaten die in dit werk

zijn verkregen kan men concluderen dat het maken van in elkaar verweven structuren een veel belovende strategie is om MOFs te ontwikkelen waarmee men een zeer goede scheiding kan behalen.

Acknowledgements

This thesis would not have been done without the help and support of a great number of people.

First of all, I would like to thank my supervisor, Berend Smit, for giving me the opportunity to start a PhD in his group. His help, stimulating suggestions, and encouragement helped me in all the time of research and writing of this thesis.

I am thankful beyond words to Sofia Calero, for everything she taught me, for giving me energy and motivation for my research, and for her constant help. Without her this thesis would not have become what it is now.

I also want to thank Prof. Chongli Zhong for giving me a chance to work in his group. It was a pleasure to work for and with you. Thank you very much for your hospitality and support.

I owe a lot of gratitude to Edith Beerdsen and David Dubbeldam who have taught me all I needed to know about zeolites and COTA. Edith, thank you for the Dutch lessons and all the help you have given to me.

Words are not enough to thank the people that, with their friendship, help, and support made the years I spent in Amsterdam a happy and special time for me. I am extremely grateful to Anil for his invaluable friendship, his help and support. I also would like to thank Hong, Yuli, and Laura for their precious help and constant support, *xie xie* and *gracias*. A sincere thank to Gooitzen Zwanenburg for his help with computer related problems and for being always nice. I also wish to thank the people in our MolSim group: Jarek Juraszek, Bastiaan Huisman, Elske Leenders, Francesco Colonna, and Jocelyne Vreede. Other people who don't get thanked often enough are Renate Hippert, Truc Ngo, Maureen Sabandar, and Petra Hagen: thanks for all your help.

Many thanks also to "The Spanish": Juan Manuel Castillo, Elena García-Pérez, and Almudena García Sanchez. Thank you all for making my days in Seville and Lyon enjoyable and thanks for all your help.

I had a good time in Prof. Zhong's group, and I would like to thank Qingyuan Yang and Chunyu Xue for the fruitful collaborations and instructive discussions.

I am indebted to Frederick de Meyer for his careful translation of the Dutch *samenvatting*, and Jarek for his help with the thesis printing.

Lastly, I would like to express my special thanks to my parents, my sister Jingjing, and my boy friend for their love and support. This thesis is simply impossible without them. *xie xie*!

Published Work

Understanding the effects of electrostatic interactions on gas separation in metal-organic frameworks
Qingyuan Yang, Qing Xu, **Bei Liu**, Chongli Zhong, and Berend Smit
Submitted

Gas diffusion mechanism in catenated metal-organic frameworks
Chunyu Xue, Ziezhou, **Bei Liu**, Qingyuan Yang, Chongli Zhong
Submitted

Enhanced adsorption selectivity of hydrogen/methane mixtures in metal-organic frameworks with interpenetration: A molecular simulation study
Bei Liu, Qingyuan Yang, Chunyu Xue, Chongli Zhong, Biaohua chen, and Berend Smit
Journal of Physical Chemistry C 112 (26) **2008**, 9854-9860

Molecular simulation of hydrogen diffusion in interpenetrated metal-organic frameworks
Bei Liu, Qingyuan Yang, Chunyu Xue, Chongli Zhong, and Berend Smit
Physical Chemistry Chemical Physics 10 (22) **2008**, 3244-3249 (**Featured on the issue cover**)

A new united atom force field for adsorption of alkenes in zeolites
Bei Liu, Berend Smit, Fernando Rey, Susana Valencia, and Sofia Calero
Journal of Physical Chemistry C 112 (7) **2008**, 2492-2498

Understanding aluminum location and non-framework ions effects on alkane adsorption in aluminosilicates: a molecular simulation study
Bei Liu, Elena García-Pérez, David Dubbeldam, Berend Smit, and Sofia Calero
Journal of Physical Chemistry C 111 (28) **2007**, 10419-10426

A computational method to characterize framework aluminum in aluminosilicates
Elena García-Pérez, David Dubbeldam, **Bei Liu,** Berend Smit, and Sofia Calero
Angewandte Chemie International Edition 46 (1-2) **2007**, 276-278

Molecular simulation of adsorption of alkanes in sodium MOR-type zeolites using a new force field
Bei Liu and Berend Smit
Physical Chemistry Chemical Physics 8 (15) **2006**, 1852-1857

Evaluation of a new force field for describing the adsorption behavior of alkanes in various pure silica zeolites
Bei Liu, Berend Smit, and Sofia Calero
Journal of Physical Chemistry B 110 (41) **2006**, 20166-20171

A hybrid cylindrical model for characterization of MCM-41 by the Density Functional Theory
Bei Liu, Wenchuan Wang, and Xianren Zhang
Physical Chemistry Chemical Physics 6 (15) **2004**, 3985-3990

Front cover of Physical Chemistry Chemical Physics